Title
DEVELOPMENT OF THE HIGH-TEMPERATURE, SOLID-STATE, ELECTROMOTIVE FORCE TECHNIQUE TO STUDY THE THERMODYNAMICS OF LEWIS-ACID-BASE TRANSITION METAL ALLOYS

Author
Bullard, Gary Lloyd

Publication Date
1978-05-01

LBL-7691

DEVELOPMENT OF THE HIGH-TEMPERATURE, SOLID-STATE, ELECTROMOTIVE FORCE TECHNIQUE TO STUDY THE THERMODYNAMICS OF LEWIS-ACID-BASE TRANSITION METAL ALLOYS

Gary Lloyd Bullard
(Ph. D. thesis)

May 1978

Prepared for the U. S. Department of Energy
under Contract W-7405-ENG-48

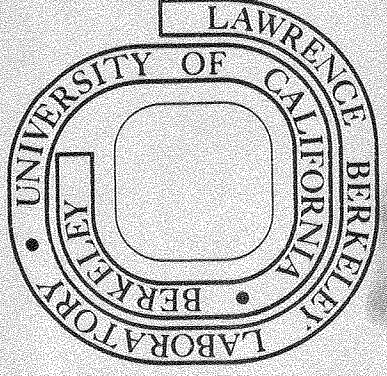

LEGAL NOTICE

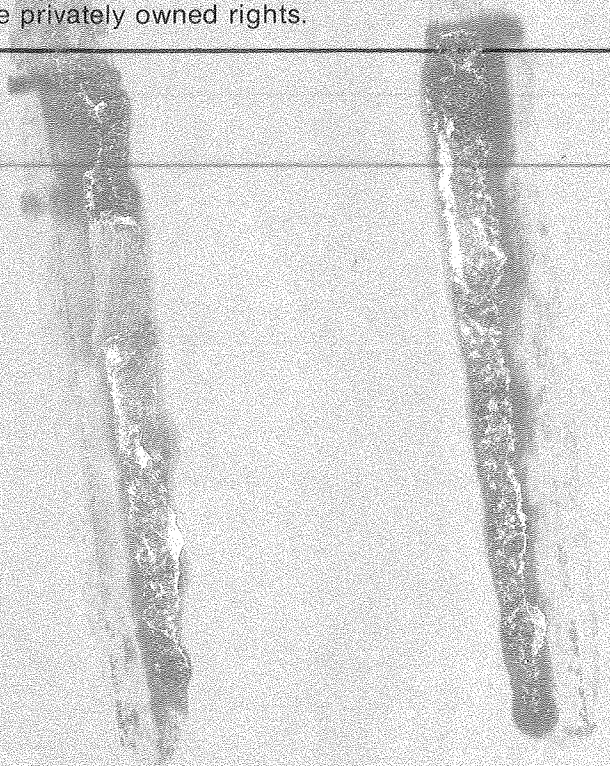

Development of the High-Temperature, Solid-State, Electromotive Force Technique to Study the Thermodynamics of Lewis-Acid-Base Transition Metal Alloys

By

Gary Lloyd Bullard

Materials and Molecular Research Division, Lawrence Berkeley Laboratory
and Department of Chemistry, University of California,
Berkeley, California 94720

ABSTRACT

The basic principles of the Engel-Brewer theory of metals are summarized and illustrated. Definitions of words used to describe its fundamentals are clarified. The theory predicts the extreme stability of the Lewis-acid-base alloys. The thermodynamics of such alloys may be obtained through the use of oxide-electrolyte, electrochemical cells. Experimental techniques associated with the use of these cells are explained in detail. Much attention is given to the preparation and processing of the materials required.

A selective review of the cell literature demonstrates frequent difficulty in obtaining accurate thermodynamic data. In an attempt to correct this situation, as well as to correct problems discovered in this work, the physical processes which create the cell emf are clearly identified. The fundamental understanding afforded by the resulting cell model implies the procedures used to both discover and eliminate errors. Those due to concentration overpotentials, reactive impurities in the gas phase, and interfacial reactions are carefully analyzed. The procedures used to test for and attain equilibrium in an alloy-oxide, powder compact are supported through identification of the transport processes that mediate equilibration.

Leo Brewer

DEVELOPMENT OF THE HIGH-TEMPERATURE, SOLID-STATE, ELECTROMOTIVE FORCE TECHNIQUE TO STUDY THE THERMODYNAMICS OF LEWIS-ACID-BASE TRANSITION METAL ALLOYS

Contents

ACKNOWLEDGMENTS

I am grateful for the assistance of the Materials and Molecular Research Division support staff. I appreciate the use of the powder metallurgy laboratory of Dr. Milton Pickus and his occasional advice. I was fortunate to be able to discuss the experimental problems involved in operating solid-state cells with Professor Wayne Worrell throughout his sabbactical leave in Berkeley. I would like to thank Professor Leo Brewer, my research director, for his patience, for his philosophy of allowing his students to work independently, and for the example of his methods of scientific reasoning.

This work was supported by the United States Department of Energy.

I. INTRODUCTION

The long range purpose of this work is to further the chemical bonding approach to alloy phase stability. Since it is still impossible to deal quantitatively, and more often even qualitatively, with the problem of alloy stability by a deductive approach from first principles, it is necessary to employ other methods of attack which are more amenable to the use of simple chemical reasoning to make predictions. Such methods rely on the inductive use of experimental data to multiply the predictive power of the otherwise unintegrated data. The policy of the present research program is to seek the aid of generally accepted models of chemical bonding. By consulting established models, one is able to identify in the broad sense the presence or absence of a cause of stability. Once a causal factor which determines stability has been defined, data may be obtained on a system in which this factor is predominant or can be separated from the others. This allows stability due to a particular cause to be experimentally calibrated; hence, the approach to a quantitative level is made.

The chemical approach is applied to metals and alloys because its extensive use with all kinds of materials makes it more applicable to physical reasoning than the band the theory or molecular orbital approach. This in turn makes it more amenable to experimental calibration or an on-the-spot sort of qualitative prediction. A chemical viewpoint of metals is expressed by the Engel-Brewer theory (1) which is a combination of basic chemical principles and experimental correlations. Its purpose is

to serve as a basis for ordering and predicting the thermodynamic properties of alloy and pure metal phases. The ultimate result of such knowledge is the understanding and prediction of metal phase diagrams and the first step in characterizing the reactivity of a metal or alloy in any chemical environment. Thus the theory has extensive application to the use of high temperature materials. For instance, the prediction of certain unusually stable intermetallic compounds by the Engel-Brewer theory warns of the possibility of reaction between common ceramics such as alumina, zirconia, or thoria, as well as the other third and fourth group or rare earth oxides, and the noble metals. Such combinations of refractory oxide and noble metal are often encountered in the ceramics industry and were formerly thought to be stable at high temperatures, but they will react readily under reducing conditions (2). Many supported catalysts are composed of this combination of materials. Dispersed noble metals have been shown to undergo strong interaction with their TiO_2 supports, causing severe loss of H_2 and CO adsorption capability (3). Applications are also found in the nuclear industry where a knowledge of phase relationships and thermodynamic properties of elements from every part of the periodic table will be required to deal effectively with several material compatibility problems. These include interaction of oxide fuel rods with their alloy claddings and fission products and the containment and cycling of liquid sodium through heat exchangers (4).

This work aims to increase the small supply of thermodynamic data available for a specific class of binary alloys, viz., the Lewis-acid-base alloys (5). Such data will facilitate the development of bonding models

aimed at characterizing the thermodynamic stability of alloys. The system presently under study is Ta-Ir. The data are obtained by means of a solid-state, high-temperature, electrochemical cell of the type introduced by Carl Wagner twenty years ago (6).

Despite the age of the emf technique, its use for the production of thermodynamic data is still not generally well in hand. Often one finds cases such as iron chromite ($FeCr_2O_4$) in which several workers have performed experiments and obtained results none of which agree with thermal data let alone with one another (7). The present experimental work was also hampered by a seemingly inordinate number of problems, many of which are not characterized as well as they might be for such an old technique; hence, they required time-consuming, difficult procedures to track them to their source. There is a need to theoretically analyze solid state cells in the context of the problems which arise when they are operated for the sake of thermodynamic measurement. Such a study is presented here; one finds that criteria for the elimination of error may be proposed and justified from a fundamental level. This allows clear statements of good experimental practice, thus facilitating the continuation of this particular experimental project as well as other projects using the emf technique.

II. THEORETICAL CONTEXT OF THE EXPERIMENTAL PROGRAM

The essentials of the Engel-Brewer theory of metals are presented and briefly explained here to provide a basic understanding of its contents. The exposition is sufficient to develop an integrated viewpoint of metallic stability and to appreciate the motivation for the experiment.

A. General Principles of Stability and Structure

The principles listed below ultimately imply modification and extension of their early foundations, the ideas of L. Pauling and W. Hume-Rothery. The recognition of d electron bonding in metals and the application of the valence bond model to them are Pauling's significant contributions to the development of the Engel-Brewer theory (8). He propounded the necessity of d electron bonding in Fe, Co, Ni, and Cu to account for interatomic distance and mechanical properties and suggested that the valence electron configuration of Cu was about $d^8\ sp^2$ in 1938. This was in general agreement with the later postulates of N. Engel (9). Pauling's valence bond treatment of the bonding energetics in alkali and alkaline earth metals formed the basis of L. Brewer's application of this method to most metals (10). Furthermore, to recall some simple chemistry, the valence bond model has taught chemists that in the nonmetals the number of bonds per atom is limited by the number of unpaired electrons per atom in the valence state, for example, four bonds for Si(sp^3), three for

P (s^2p^3), two for S(s^2p^4), and one for Cl(s^2p^5). The number of sp valence electrons determines, and is thus correlated with, the crystal structure of the nonmetals. W. Hume-Rothery (11) was the first to extend this concept to metals. He pointed out that many intermetallic compounds which had the same valence electron-to-atom ratio had the same crystal structure, even though they differed in composition and constituents. Engel applied this correlation between crystal structure and valence electron concentration more broadly to both elements and alloys.

The fundamentals of the Engel-Brewer theory may be summarized from the works of Engel (9, 12-15) and Brewer (1, 5, 10, 16-22):

[1]. The valence-bond model is applicable to metals. Bonding can be viewed as being accomplished through vacant orbitals in the bonding valence state so that stability is determined by the number of unpaired electrons available for bonding and efficiency of overlap of their charge clouds.

[2]. There is a correlation between the number of sp electrons in the bonding valence state, i.e., the number of sp electrons per atom, and the crystal structure. If n is the total number of valence electrons, then a $d^{n-1}s$ electronic configuration is associated with body-centered cubic (bcc), $d^{n-2}sp$ with hexagonal close-packed (hcp), $d^{n-3}sp^2$ with cubic close-packed (ccp).

[3]. The d electrons in a metal are only partially delocalized while the sp electrons are much more delocalized. This difference leads to separation of the roles of sp vs d electrons in determining structure. Ultimately, only the concentration of long-ranging sp electrons determines structure. The d electrons are much more localized and have poor overlap predominately with d orbitals of nearest neighbors. Overlap increases from 3d to 4d to 5d, however. Note that some d bonding will be lost if the number of d electrons exceeds five because this necessitates the pairing of electrons in the bonding valence state.

To clarify the application of the valence-bond model to a metal, consider the case of Mg which is schematically represented in Figure 1 (18). The ground state of gaseous Mg is s^2. If the internuclear distances, r, of a mole of such atoms are reduced, the interactomic potential follows the very shallow curve. Only a weak van der Waals interaction is possible in this case since the Pauli exclusion principle does not allow overlap of the 3s orbital. This prevents the s electrons from interacting strongly with the nuclei of adjoining Mg atoms. This hypothetical solid would be held together by the same van der Waals interaction which holds the Mg_2 gaseous molecule together. Its potential curve is known (23) and has a dissociation energy of only 1.15 kcal/mole. On the other hand, if the promotion energy of 63 kcal/mole is used to excite the gaseous atoms from s^2 to sp and the excited Mg atoms are allowed to approach one another, the very deep potential curve results. This curve

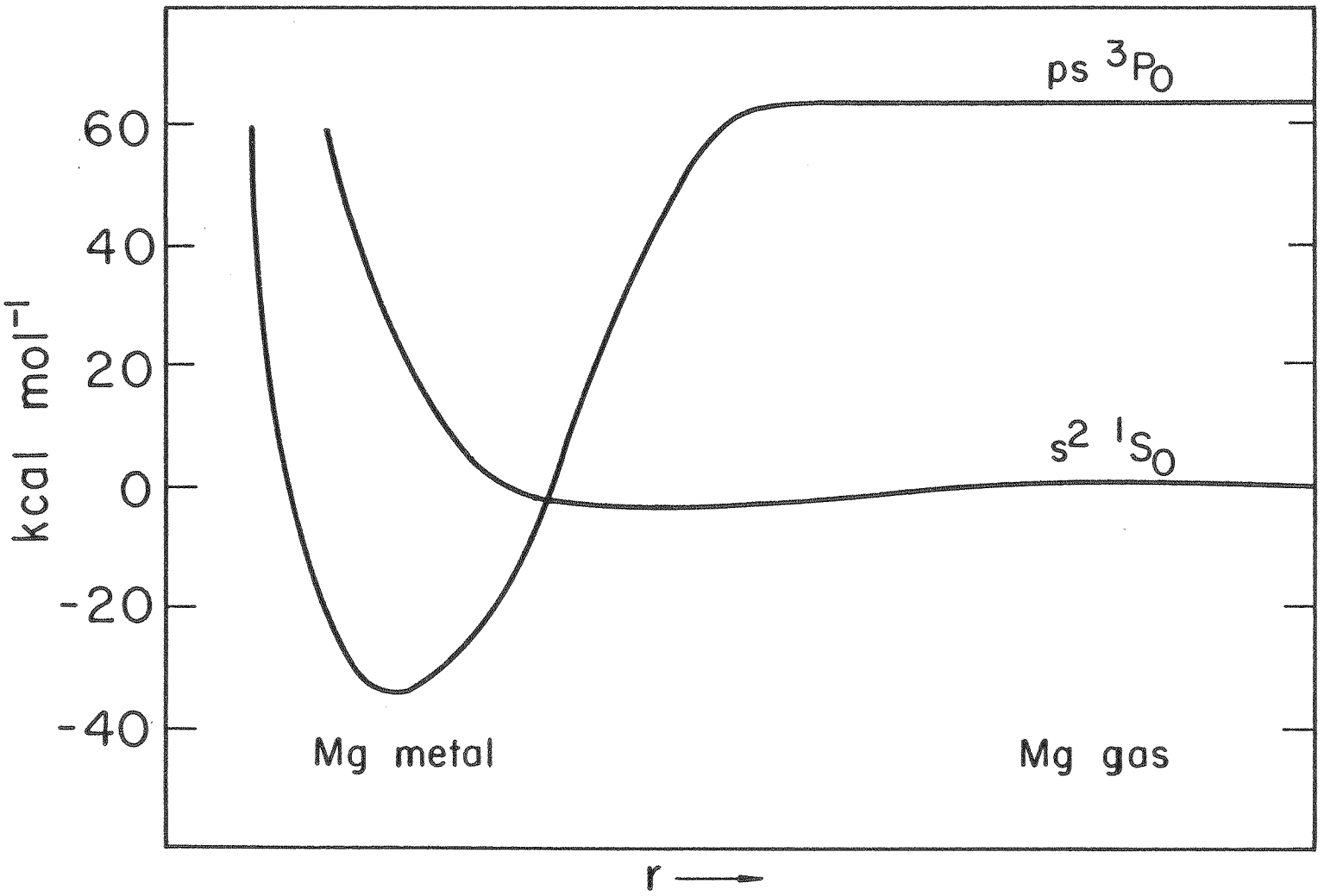

XBL7210-4209

Figure 1. Potential energies of s^2 and sp configurations of Mg as a function of internuclear distance.

schematically represents the potential energy of a mole of Mg atoms in the sp configuration. Interaction is much stronger because there are two electrons per atom available for bonding. As the internuclear distance is decreased, the energy of the sp configuration drops below that of s^2; and the cohesion in Mg metal is due to two bonding electrons per atom. The enthalpy of atomization from solid to gaseous ground state of Mg metal is thus the enthalpy released when atoms in the bonding valence state condense, the bonding enthalpy of gaseous sp Mg (17), minus the promotion energy to the sp state of Mg gas, or 35 kcal/mole.

The valence-bond model is then a thermodynamic cycle used to break up the real, physical process of bonding into simpler steps. The actual bonding process for Mg involves a cross-over region from the s^2 to the sp curve where bonding and change in electronic configuration occur simultaneously. Dealing with this complex process in order to determine the heat of atomization is avoided by considering the simpler steps. They imply that bonding may only take place if the bonding enthalpy is sufficient to pay off the promotion energy. A curious result of this rule is that under certain conditions gaseous Mg atoms can be denied sufficient neighbors with which to interact to achieve a bonding (sp) configuration (24). In this unique situation sufficient bonding enthalpy cannot be generated to pay off promotion. Condensation is restricted; and the surprisingly high pressure of 10^{-6} torr of Mg atoms, compared to the equilibrium value of 10^{-21} torr, can be maintained at 300 K.

The one-to-one correspondence between major metallic crystal structure and electronic configuration (the Engel correlation) was inductively developed by Engel (9, 13, 14) from consideration of elemental structural data, heats of atomization, and phase diagrams. Brewer (10) confirmed it by using heats of atomization and spectroscopic data of gaseous atoms in conjunction with the valence-bond model. To generally indicate how this was done one may consider Figure 2 (17) which presents the relative energies of the $d^{n-1}s$ and d^{n-2} sp electronic configuration of the gaseous atoms of the second transition series. The energy of each gaseous electronic configuration appears as a band because, in general, there are several spectroscopic states for each configuration corresponding to different combinations of the spin and orbital momenta of the electrons. The range of energies of spectroscopic states of highest spin multiplicity (spin momenta combined with minimum pairing) corresponding to each configuration is shown. Since the d electrons are in an inner shell, they are not shielded from the nuclear charge as well as the sp electrons which are in an outer shell; therefore, the d orbitals become stabilized with respect to the s and p orbitals as the nuclear charge increases from Sr to Mo. The d^{n-2} sp configuration then becomes much higher in energy than the d^{n-2} s. Assuming as a first approximation that the bonding enthalpy is fixed merely by the total number of bonding electrons and invoking the valence-bond model, one notes that for Sr, Y, and Zr both electronic configurations can be expected to be important for the solid. This means that sufficient bonding enthalpy is available to pay off the promotion energy for a bonding valence state of either $d^{n-1}s$ or d^{n-2} sp and that the heats of atomization of a solid formed from either

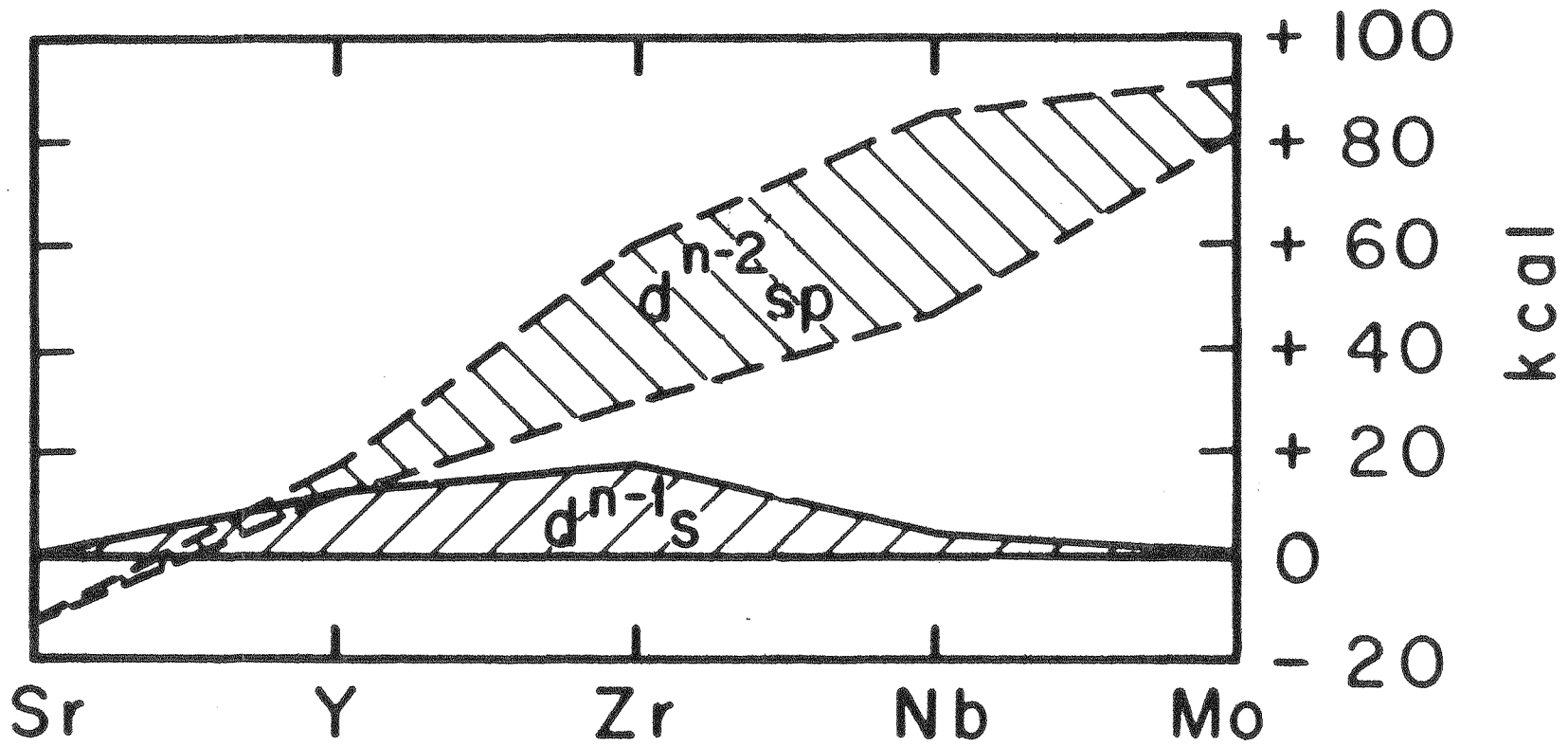

MUB-8895

Figure 2. Relative energies of $d^{n-1}s$ and d^{n-2} sp electronic configurations of gaseous atoms of the second transition series, Kcal/gm-atom.

will be close. For Nb and Mo the heat of atomization of a solid with electronic configuration d^{n-2} sp would be expected to be much less than one based on a $d^{n-1}s$ configuration because much of the bonding enthalpy would be used to pay off the promotion energy in the case of the former. By the Engel correlation, both bcc and hcp are expected for Sr, Y, and Zr while only bcc is expected for Nb and Mo. Examination of Table I (17) which displays the crystal structures of the elements confirms these expectations. For Sr, Y, and Zr the heats of atomization are close for different crystal structures so the phase with the highest entropy, viz., bcc due to its lower co-ordination number, occurs at higher temperatures. For Nb and Mo only the bcc structure is stable. It should be mentioned that small amounts of H may be necessary to stabilize hcp Sr (25), but the enthalpies of the bcc and hcp phases must be very close. Also, ccp Sr is one of the very few clear-cut contradictions to the Engel correlation, all of which occur in only weakly bonded systems (1).

The last principle enumerated describes the difference between sp and d electrons as being primarily due to that part of real space which each predominantly occupies. The fact that the d electrons are much more localized than the sp electrons in a metal is not due to their orbital angular momentum quantum numbers in the bonding valence state but to their principle quantum numbers. The sp electrons are always in the outer shell, while the d's are in the next or inner shell, so that their charge clouds just protrude from the filled s and p orbitals of the same shell. Upon condensation of atoms in the bonding valence state, the degree of mixing between sp and d electrons must be limited due to their poor overlap. Thus when one speaks of d electrons in the context of the

Table 1. Crystal structure of the elements.[a]

Li I	Be II	B * *											C IV >=[f]	N =[b]	O =[b]	F —[c]	
Na I	Mg II	Al III											Si IV	P [e]	S <[d]	Cl ·—·	
K I	Ca I III	Sc I II	Ti I II	V I	Cr I	Mn I III β χ	Fe I III I	Co III II	Ni III	Cu III	Zn II	Ga All	Ge IV	As ↖	Se <	Br —	
Rb I	Sr I II III	Y I II	Zr I II	Nb I	Mo I	Tc II	Ru II	Rh III	Pd III	Ag III	Cd II	In (III)[g]	Sn A5 IV	Sb ↖	Te <	I —	
Cs I	Ba I	La I III II	Hf I II	Ta I	W I	Re II	Os II	Ir III	Pt III	Au III	Hg A10	Tl I II	Pb III	Bi ↖	Po	At	
Fr	Ra	Ac															

Ce I III II	Pr I II	Nd I II	Pm	Sm I (II)[g]	Eu I	Gd I II	Tb I II	Dy I II	Ho I II	Er I II	Tm I II	Yb I III	Lu I II
Th I III	Pa *	U I σ A20	Np I **	Pu I * III ***	Am ? II	Cm ? II	Bk	Cf	Es	Fm	Md		Lw

[a]I: Body centered cubic, A2. II: Hexagonal close packed, A3. III: Cubic close packed, A1. IV: Diamond, A4. Asterisk denotes complex structure. [b]Diatomic molecules with double or triple bonds. [c]Diatomic molecule with a single electron pair bond. [d]Atoms which form two single bonds per atom to form rings or infinite chains. [e]Three single bonds per atom, corresponding to a puckered planar structure. [f]The graphite structure where one resonance form consists of two single and one double bond per atom. [g]Parentheses indicate slight distortions. The structures are listed in order of temperature stability except for metastable diamond.

Engel-Brewer theory, one is not signifying the one electron wave function "d-ness" of such states but merely those which arise from interactions of electrons in the inner shell. Meaning can also be ascribed to an internally paired d electron in a solid by considering its expected position in real space. A bonding d electron would have a higher probability density between nuclei so that more than one nucleus could act upon it while a nonbonding, internally paired d electron would be localized about a single atom. The degree of overlap attainable by a bonding d orbital with its neighboring d orbitals is determined by how much it protrudes above the filled s and p orbitals. As nuclear charge increases and shells are added from 3d to 4d to 5d, the filled s and p orbitals of the same inner shell contract more than the d orbitals due to their poorer shielding from the nucleus. Thus more d overlap can be achieved before the repulsive wall of the filled orbitals is met as one proceeds from the first to the third transition series.

After an abstract statement and clarification of basic principles, a few illustrations of the applicability of these ideas should serve to indicate their usefulness.

The variation in crystal structure of the metals across the periodic table can be explained (16, 17). The second transition series has been partly discussed, and it shall be considered again here. Starting at the far left with Rb, its ground state is s and so is its electronic configuration in the solid giving a bcc structure (see Table 1). Sr may assume a ds in the solid yielding bcc or sp if the electron concentration is increased a bit with H, Sr being hcp under these conditions. The similarity of promotion energies of the dsp and d^2s configurations allow

Y to assume hcp or bcc respectively. Likewise for Zr, d^3s is associated with bcc and d^2 sp with hcp. With increasing nuclear charge, the d orbitals increase greatly in stability and a $d^{n-2}sp$ has much too high a promotion energy to be paid off. Thus Nb and Mo are restricted to d^4s and d^5s, respectively, and both are bcc. Upon arriving at Tc, there is the option of pairing up two d electrons to retain the bcc structure, but this would cause a loss in bonding energy. It is more favorable to keep the d's in a situation of maximum bonding by promoting to d^5sp. Now there is a change in crystal structure from bcc at Mo to hcp at Tc. Ru stays hcp by adding a d and assuming a d^6 sp. Rh turns ccp because it finds it more favorable to promote to d^6sp^2 than to destroy more d bonding. Pd and Ag have d^7sp^2 and d^8sp^2 respectively and are ccp while Cd fills its d orbitals ending up with $d^{10}sp$ and is hcp. Brewer has verified these configurations as mentioned above except for Rh, Pd, and Ag because spectroscopic data for $d^{n-3}sp^2$ promotion energies are lacking for these elements. He has defended the Engel correlation for the noble metals (5), however, on the basis of interatomic distances, heats of vaporization, and the plausible numbers of bonding electrons which need be involved. The Engel correlation and the chemical bonding approach thus offer order to an interpretation of a sequence of crystal structures.

The utility of considering the bonding valence state to be the electronic configuration in the metal is also illustrated by elucidation of the confusing trend in heats of atomization vs. melting points of the lanthanides (20). Figure 3 displays the heats of atomization of the lanthanides compared to their respective melting points. The trend of interatomic distances through the lanthanides can be used to establish that all

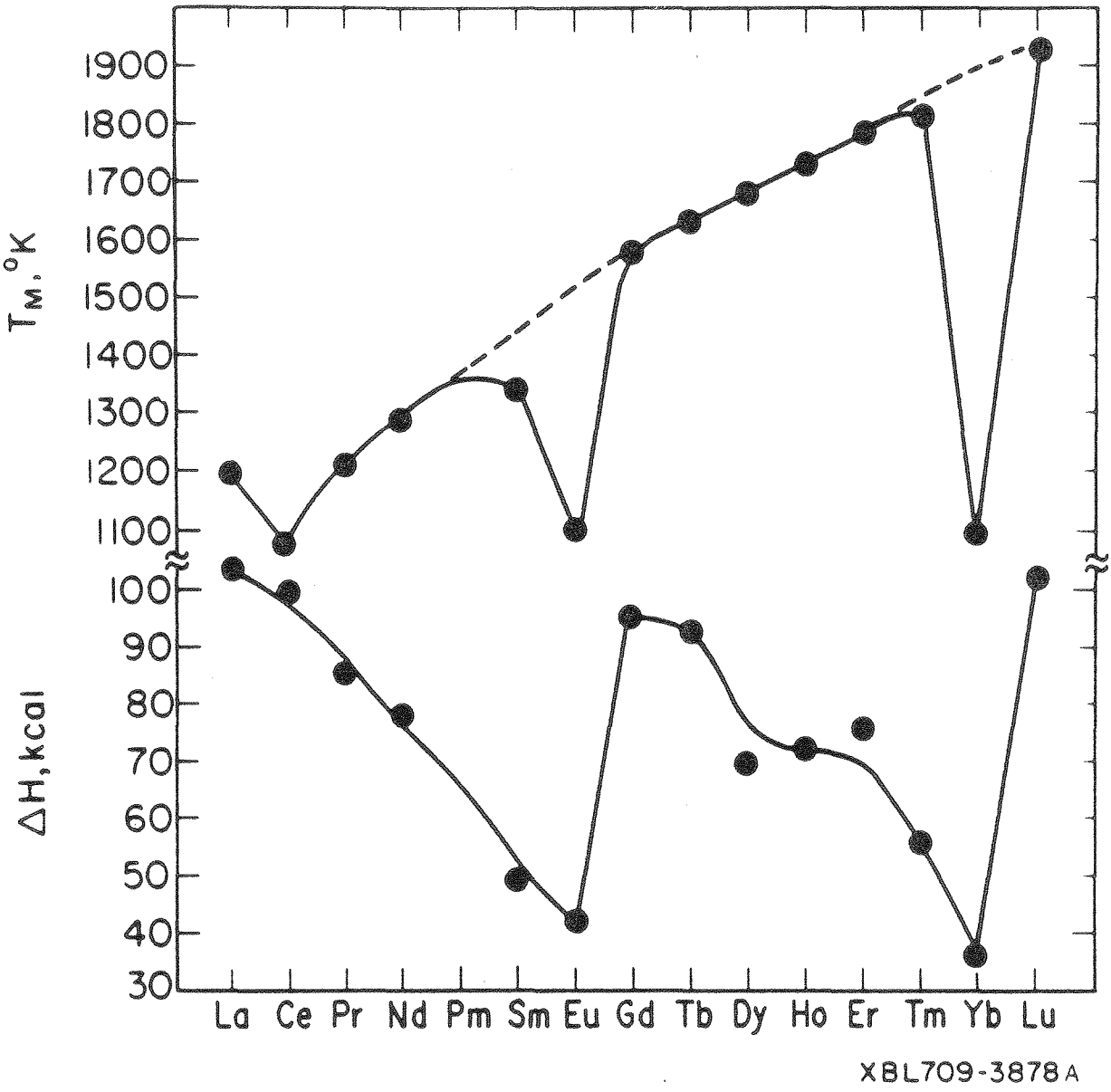

Figure 3. Melting points and heats of atomization of the lanthanide metals.

the lanthanides use three electrons in bonding except Eu and Yb which show sudden increases in lattice parameter (26). They have two bonding electrons. The small heats of fusion of metals implies that bonding is usually similar in the solid and liquid phases. One then expects to see an increase in melting point with an increase in cohesive energy or the strength of bonding. On this basis the divalent bonding character of Eu and Yb explains their low melting points and heats of atomization. From La and Sm and from Gd to Tm the increase of melting point with nuclear charge along with the decrease in lattice parameter imply tighter binding which is contradicted by a shrinking heat of atomization. To resolve this contradiction one must recognize that the enthalpy liberated upon condensation of atoms in the bonding valence state, the bonding enthalpy, is the appropriate energetic measure of chemical interaction, and, it is the quantity, not the heat of atomization, which is rigorously associable with other measures of interaction such as interatomic distance and melting point. The degree to which the heat of atomization is unsuitable for such associations is given by the promotion energy or energy difference between the gaseous ground state and the excited state which represents the bonding valence state. Brewer (20) has used the Engel correlation to identify the correct electronic configuration in the solid. By adding together the promotion energy to this electronic configuration in the gas and the heat of atomization, he calculated the bonding enthalpy for the bcc phase of each lanthanide because this is the phase which is in equilibrium with the liquid. His results are shown in Figure 4. The expected trend of bonding enthalpy and melting point is now observed. Comparison with Figure 3

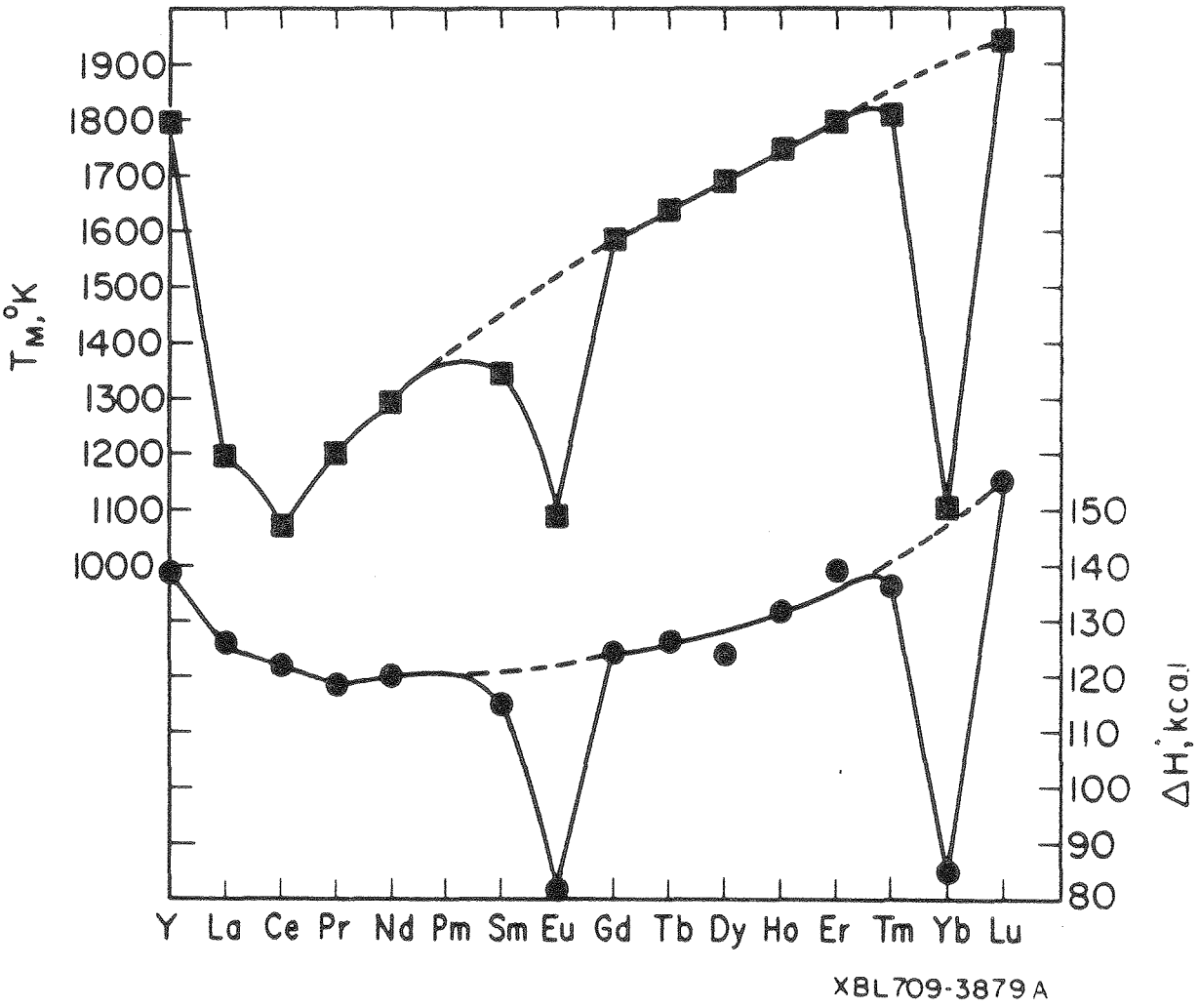

Figure 4. Melting points and bonding enthalpies of the lanthanide metals.

shows that there is an increase in promotion energy to the trivalent bonding valence state with nuclear charge in each of the two sequences separated by Eu. The trivalent bonding enthalpy increases rather slowly with nuclear charge so that the trend in heats of atomization is caused by the rapid variation of promotion energy.

The last example to be presented focuses on the difference in spatial distribution of sp and d electrons in a solid. The relatively poor overlap of the inner d orbitals compared to the outer s and p orbitals enables one to predict the effect of pressure on the phase equilibria between crystal structures of the same transition metal (22). In general, if pressure is applied to the lattice, the closed shells must compress to allow the nuclei to move closer together. Recalling that the d orbitals barely protrude above the closed shells, this markedly increases their exposure (relative to no applied pressure); and, a substantial increase in their degree of overlap occurs. The s and p orbitals, however, undergo much less change in degree of overlap because the fraction of sp electron density outside the closed shells experiences only a very small relative change under pressure. Then, bonding through d orbitals is favored under pressure; hence, the phase with the most unpaired d electrons will be stabilized in this situation. To deal with a specific application of these ideas, consider the bcc-hcp equilibrium in Zr. The bcc is d^3s and the hcp is d^2 sp so that under pressure, the bcc would be favored because

it has the greater number of bonding d electrons. The transition temperature from hcp to bcc is thus expected to decrease with increasing pressure. Consideration of both ccp-bcc equilibria of Fe, which is on the opposite side of the periodic table, leads one to predict that here the bcc will be destabilized relative to ccp under pressure. The bcc is d^7s and the ccp is $d^5 sp^2$. Due to the necessity to internally pair d electrons in the bcc, this phase has the least number of bonding d electrons, hence the above prediction. Furthermore, low temperature bcc Fe may be expected to convert to hcp under pressure. The reason for this change is again simply explained. As pressure increases the efficiency of d bonding increases and eventually, promotion of a d electron to a p orbital becomes favorable. The electronic configuration changes from $d^7 s$ to $d^6 sp$ so that the number of bonding d electrons increases by one. The Engel correlation then demands a change in crystal structure due to the increase in sp electrons. Again, the phase with the most bonding d electrons is favored. Klement and Jayaraman (27) and recently Pistorius (28) have reviewed the high pressure phase diagrams of the elements. The predictions made here, as well as all analogous ones, are all supported by well-established data.

The validity of the predictions made above rests on the difference in spacial distributions of sp vs. d electrons. At the beginning of each transition series, these spacial distributions do not differ nearly so much as they do in the fourth and higher groups because the nuclear charge has not increased sufficiently to drastically contract the inner shell d orbitals relative to the outer shell s and p orbitals. The extended d orbitals at the beginning of the second transition series and the relative contraction with increasing nuclear charge just noted is reflected in the

energy difference between the $d^{n-1}s$ and the $d^{n-2}sp$ configurations of the gaseous atoms shown in Figure 2. One must therefore not expect the elements at the beginning of the periods to behave under pressure according to the above arguments. Several disagreements, for example La and Ba, can be found in the reviews noted above. In fact, due to the much smaller difference in spacial distribution of sp vs. d electrons of metals in this part of the periodic table, they tend to fall outside the Engel-Brewer theory's physical conception of a transition metal. Violations of the Engel correlation here, such as the occurrence of ccp Sr, are therefore not surprising.

This concludes the presentation and illustration of the essential theoretical framework of the Engel-Brewer theory of metals. All specific aspects of the theory as it relates to pure metals may be deduced from the three principles discussed because they are statements of concepts. Some such specific aspects were selected for discussion because they emphasize the theory's integrative power over a given property of many or all metallic elements.

B. Principles of Alloy Phase Stability

The last section dealt with general principles of structure and stability which were illustrated for pure metals only. The task of this section is to briefly indicate how extensions of these same principles are used to understand and predict alloy phase stability and structure. When one examines the effects of a chemical difference in components of an alloy, three factors arise, all of which must be simultaneously considered in dealing with the stability of a given alloy. They have been

extensively reviewed by Brewer in his monograph on the prediction of high temperature phase diagrams (10):

[1]. Differing size of component atoms leads to either better packing and increased stability or lattice strain and decreased stability, depending on the degree of equivalence of lattice sites.

[2]. If pure components have substantially different internal pressures and no specific interactions result between them upon combination, their enthalpy of mixing will be positive and similar to that of a regular solution.

[3]. Electronic factors which result in specific interactions between components and changes in their bonding valence state relative to the pure elements can produce very negative enthalpies of mixing.

Each of these three points will be explained and illustrated in turn so that a coherent viewpoint of alloy stability may be formed. The third point includes the generalized-Lewis-acid-base interaction, the subject of study in the experimental program.

Consider the results of alloying two elements with atoms of different size. If maximum efficiency of overlap of orbitals cannot be achieved due to constraints imposed by the long range order of the crystal lattice, strains in the lattice will result. The bond energy which is lost due to inefficient overlap is usually called strain energy, and it is unfavorable to thermodynamic stability. The simplest illustration of a result of lattice strain is the classic formulation of Hume-Rothery

(29). He examined the effect of size on the extent of primary solubility i.e., the solubility limit of pure metal A in pure metal B without the precipitation of a second phase. The size of an atom was defined by its elemental diameter calculated from x-ray data. With this admittedly somewhat arbitrary but uniform basis for comparison of atomic sizes, Hume-Rothery found that whenever the diameter of two metal atoms differed by more than about 15%, primary solutions were restricted to not more than 5 a/o solute. A more recent review of all known binary systems shows a 90% agreement with this principle (30). In these cases strain energy increases with increasing solute concentration, and the phase is destabilized. Hume-Rothery also noted that his size factor argument gave a definite result only in the negative sense: It could predict restricted primary solubility if the size factor were unfavorable (the diameters differed by more than 15%), but extensive solubility was not necessarily implied if the size factor were favorable. For this to occur other factors must be considered and satisfied. One of these will be examined shortly.

Relative atomic size, rather than being a detriment is stability, can also enhance it. The favorable thermodynamic effect of size difference is achieved by allowing the usual elemental coordination numbers of 8 or 12 to be exceeded upon alloy formation. If proper size criteria are met, a new crystal structure can be formed with non-equivalent lattice sites commonly having 14 or 16 atoms in nearest neighbor coordination. Such closer packing with greater than usual coordination numbers allows more effective overlap of bonding orbitals, hence the favorable effect on

stability. A class of intermetallic compounds which take particular advantage of this effect are the Laves phases (31). The factors which determine their occurrence have been briefly discussed by Brewer (10) and throughly reviewed by Nevitt (32). They point out that the unique feature of the Laves phases with $MgNi_2$ and $MgCu_2$ type structures is the presence of a coordination polyhedron of 16 with (if the composition is denoted generally by AB_2) an A atom at the center surrounded by 12 B atoms and 4 A atoms.

The second major determinant of alloy stability arises from the difference in internal pressure,* or "strength of binding," between the pure metals. J. Hildebrand's theory of regular solutions (33, 34) is used to predict alloying behavior resulting from such a difference. As Hildebrand formulated his theory, primarily in the content of nonmetallic solutions, it involved three points: First, the system to which the theory is to be applied must have no specific interactions, such as solvation or association between components. Second, relative internal pressures are characterized with the quantity $(\Delta E_{vap}/V)^{1/2}$, called the solubility parameter, in which ΔE_{vap} is the energy of vaporization per mole and V is the molar volume. Third, in order to calculate an enthalpy of mixing, regular solution theory must assume, because it employs pair-wise addition of interparticle interaction energies, some value for the like-unlike interaction energy between particles of different components. This Hildebrand took to be the geometric mean of the like-like interaction energies, an assumption which was very successful in dealing with his van der Waals systems.

*thermodynamic definition is $(\partial E/\partial V)_T$

The extension of regular solution theory to metallic systems requires interpretation of the three points discussed in the last paragraph in the context of metals. First, to predict thermodynamic properties of alloys from those of the pure components, the electronic configurations of the components must be the same or very nearly so in the alloy as they are in the pure elements. Second, the appropriate representation of relative internal pressure is a solubility parameter based on the energy of vaporization of the solid to the gaseous bonding valence state rather than to the gaseous ground state. Hildebrand's theoretical derivation of the regular solution energy of mixing equation (in either reference quoted above) clearly shows that the occurrence of solubility parameters therein arises from the pairwise addition of interparticle potentials. In a metal, the interatomic potentials are associated with the bonding valence state; hence, so is the solubility parameter. Third, Hildebrand notes that not even for the van der Waals interaction is there a theoretical justification for placing the like-unlike pair interaction energy equal to the geometric mean of the two like-like interaction energies. For an alloy, which involves much more complex interactions, it is certainly unclear what to use for this quantity. It must therefore be calibrated using existing solubility data.

Brewer has applied both the original and adapted form of the regular solution equations to binary alloys. The enthalpies of mixing are positive because like-unlike interaction energies are less than the arithmetic mean and the enthalpies become more and more positive as the differences in solubulity parameter increase. Thus solubilities decrease as this

difference increases. Brewer has found that the original form of regular solution theory is sufficient to predict general solubility and phase behavior in binary alloys between transition metals in the first six rows of the periodic table (10). (Little change in electronic configuration occurs when these elements are mixed, so the regular solution treatment is applicable.) Usually solid solubilities of greater degree were predicted than were found experimentally. This occurred, for example more markedly, in the systems Zr-V and Cr-Ta where substantial size differences exist. Clearly lattice strain is responsible for the reduction of solubilities below expectations based on differences in internal pressure alone. Therefore both factors, size and internal pressure, must simultaneously be considered in dealing with solid phase behavior in this group of metals. This insight also offers one reason why Hume-Rothery's size factor argument only operates in the negative sense: Even if atomic diameters are nearly the same, solubility parameters must also be sufficiently alike to allow extended solubility.

Application of regular solution theory adapted particularly for use with metals as outlined above will appear in Brewer's monograph on the thermodynamics of molybdenum compounds and alloys (35). By comparisons with existing data, he found that a useful estimate of like-unlike interatomic interaction energies is the average of the arithmetic mean and the geometric mean. This assumption, along with the use of solubility parameters based on the bonding valence state, allows the testing of the reliability of experimental data well as the prediction of solubilities where experimental data are presently quite sparse, for example, in the Mo-alkali metal, -lanthanide, and -actinide systems.

The third source of alloy stability is the electronic factor which involves a specific electronic interaction between the components of an alloy. This interaction is novel because it could not have been so simply identified, or perhaps not identified at all, except by a chemical approach to metallic bonding, and because it imparts extreme stability to the alloys in which it occurs. Consider the number of d electrons in transition metals from opposite sides of the periodic table compared with the maximum possible number of bonding d electrons. On the left side, full d bonding capability is not utilized because each transition metal has less than five d electrons which leaves completely vacant d orbitals. On the right side, d bonding is also restricted below maximum because each transition metal has more than five d electrons which results in internal pairing and the destruction of bonding capability. An alloy of a d electron rich metal with a d electron poor metal allows the internally paired d electrons of the former to make use of the vacant orbitals of the latter. Non-bonding electrons become bonding electrons through a generalized Lewis-acid-base reaction in the same manner as in the complex $F_3B{:}NH_3$. Examples would be the reaction between Zr (d^3 s) and Pt (d^7 sp^2) or between Ta (d^4 s) and Ir (d^6 sp^2). The extreme stability resulting from such combinations has been demonstrated by Brewer and Wengert (36) who used a series of reactions between noble metals and ZrC to form intermetallic compounds and Meschter and Worrell (37,38) who used the emf technique to obtain thermodynamic quantities in the Ti-Pt, Zr-Pt, and Hf-Pt systems. The electrochemical data yielded Gibbs energies of formation at 1300K for the intermetallic compounds $TiPt_3$, $ZrPt_3$, and $HfPt_3$ of -71.3, -91.7, and -97.4 kcal/mole respectively.

Clearly, unmodified regular solution theory is not applicable to such strongly interacting systems due to the extreme changes of electron configuration upon alloying. Different methods must be developed and used to provide quantitative predictions of stability. They are presently lacking, but it is possible to utilize some aspects of the Lewis-acid-base interaction to render qualitative predictions involving periodic trends in stability. Recollection of the increasing strength of d bonding upon passing from the first to the third transition series implies that replacement of an element in a given Lewis-acid-base compound with one directly below it in the periodic table will cause an increase in stability while replacement with one directly above it will cause a decrease in stability. This method of comparison keeps all factors constant except component identity. This vertically based trend is reflected by Meschter's data cited above. The stability of the Pt intermetallic increases as its fourth group component is changed from 3d to 4d to 5d. Likewise each Pd compound will be less stable than its Pt correspondent. Referring to Table 2, which lists the electronic configurations of elements in the second transition series, two specific examples of periodic trends of a horizontal directionality may be identified. Again, only component identity is considered to vary in each comparison. What trend in stability will arise if an acid, such as Zr, is alloyed with each base in turn in the series Ru through Ag? Two opposing factors must be considered to answer this question. First, as the atomic number of the base increases the number of non-bonding, internally paired d electrons increases. Stability is enhanced by this factor due to the increase in electrons available for transfer. Secondly, however, precisely because nuclear charge is increasing, electrons become

Table 2. Electronic configurations of transition metals of the second transition series.*

Rb	Sr	Y	Zr	Nb	Mo	Tc	Ru	Rh	Pd	Ag
s	ds	d^2s	d^3s	d^4s	d^5s	d^5sp	d^6sp	d^6sp^2	d^7sp^2	d^8sp^2

*For Sr, Y, and Zr, only the high-temperature bcc structure is listed.

increasingly difficult to transfer. The result is an increase in stability to a maximum, then a drop. Analogously, if a given base, such as Pd, is alloyed in turn with each metal in a series of acids in order of decreasing atomic number, such as Nb through Rb, then stability is again expected to increase to a maximum, and then to drop. A greater number of empty d orbitals, moving to the left, increases capacity for accepting donated electrons; but the degree of electron transfer is at the same time lessened by the shrinking nuclear charge. Figure 5, taken from Brewer and Wengert, illustrates the first of these horizontally based predictions. The excess partial molal Gibbs energy of Zr at infinite dilution at 1800K is plotted against solvent identity. Each maximum is clear as well as the increased interaction of Zr with 5d transition metals relative to 4d ones. These trends are useful because if data for some alloys are known, limits to the stabilities of related others may be set.

Lastly, a brief word is necessary about the determinant of major metallic crystal structure in alloys. It is the sp electron concentration per atom, the same as in pure metals. In the case of alloys, each structure correlates with a range of sp electron concentration per atom (10). The bcc structure occurs with 1 to 1.5 sp electrons per atom, hcp with 1.7 to 2.1, and ccp with 2.5 to 3.

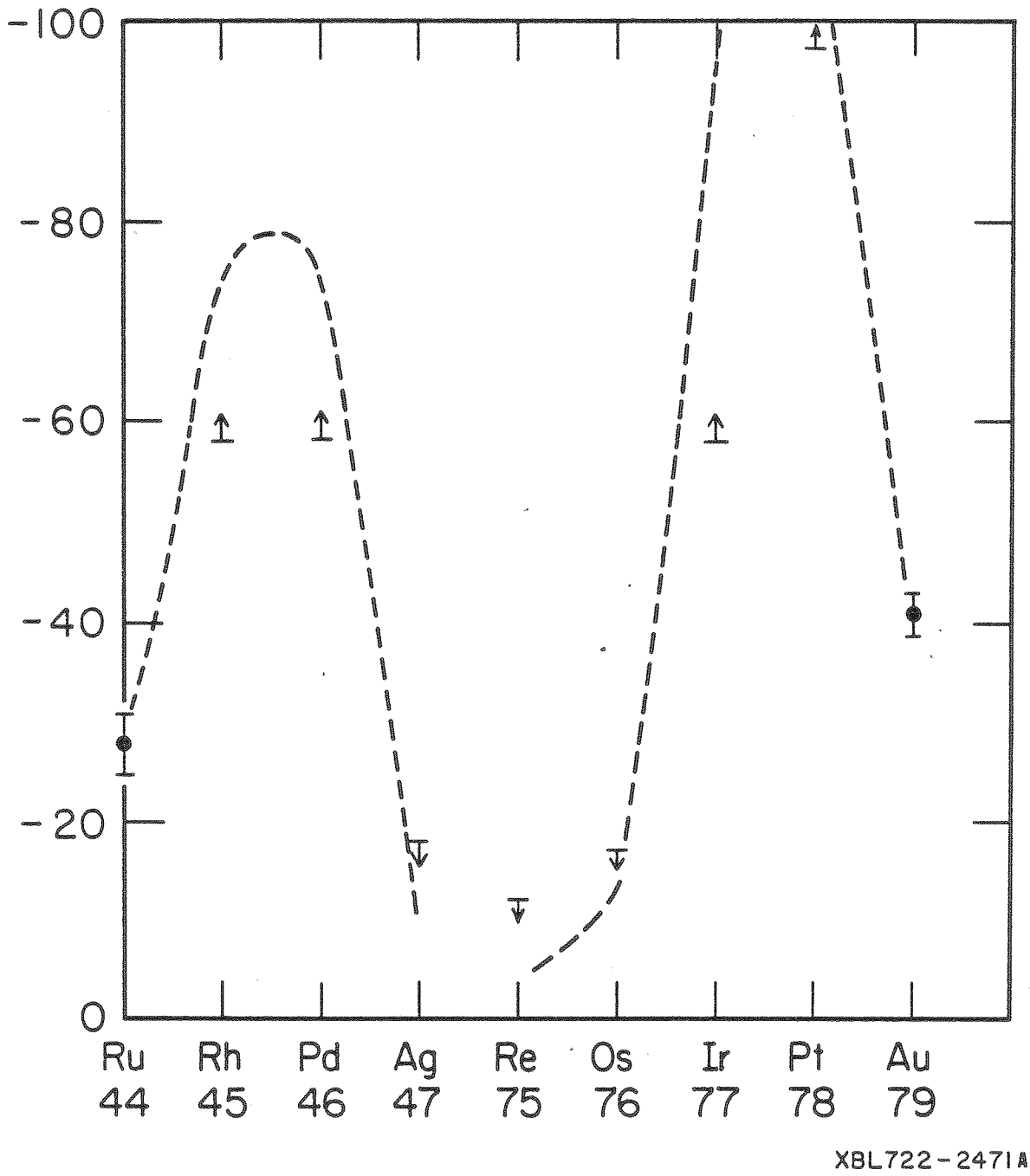

Figure 5. Excess partial molal Gibbs energy of zirconium in kcal/gm-atom at low concentrations in Ru, Rh, Pd, Ag, Re, Os, Ir, Pt, and Au at 1800K.

C. Motivation for the Experimental Project

There are special, difficult problems associated with the prediction of stability and structure of Lewis-acid-base alloys; until they are surmounted, quantitative results are not possible. This section defines such problems, and indicates general directions toward their solution.

Picture physically the bonding situation in the alloy. The transfer of d electrons to establish the new bond requires some separation of charge. The degree of transfer is promoted by the magnitude of the covalent bonding energy and some sort of back bonding which is necessary to reduce charge separation. A simple, probable form of back bonding would be a partial shift of sp electron density from the acid toward the base. The problems now arise from this physical situation. Because d electrons are not shared equally and the bond is polarized as well, d bonding energy is not obtainable directly from Brewer's determinations of d bonding energies per electron in pure metals (17). Likewise, the effect of polarization of sp bonds on their bonding energy must be explained. Also any coulombic contribution must be taken into account. The inability to quantitatively characterize any of these effects makes stability prediction enormously difficult. Further complications result when the distribution of electrons between d and p orbitals is considered. Whether an electron will occupy a d or a p orbital is determined by the bonding energy, which reflects the difference in bonding energy per electron of a p vs a d electron, and the promotion energy associated with a given alloy electronic configuration. The criteria of interest form an analogy with pure metals. The distribution between d and p must then be ambiguous because it depends

on factors with which there are already problems. This in turn imparts a wide range of uncertainty to quantitative prediction of composition range for a given structure since each structure is associated with its own particular range of sp electron concentration. Since a substantial fraction of the various possible alloys of all metals are Lewis-acid-base alloys, these road blocks to prediction represent a barrier to a general theory of alloy stability.

As a means to overcome this barrier, the experimental project focuses on obtaining thermodynamic data of certain Lewis-acid-base binary systems. Results will be used to calibrate the various contributions to stability noted, in keeping with the philosophy mentioned in the introduction. Apportionment of stability among the various factors will be aided by a general understanding of the behavior of the distribution of electrons between p and d orbitals as a function of composition. Consider the titration of an acid with a base. At the beginning as base is added, the empty d orbitals of the acid act as sinks for the non-bonding d electrons of the base. This causes a sharp increase of stability as the titration proceeds, but only up to a certain small range of composition. Then the d orbitals are more saturated in bonding capacity, and further addition of electrons to them would greatly increase the amount of internal pairing. Instead, however, some d electrons of the base transfer to the p orbitals of the acid to partially counteract this effect. The result is a decrease in the rate of increase in stability mentioned above because preparing non-bonding electrons for bonding now requires a promotion energy while none was required before. How the available orbitals are utilized is thus reflected

by trends in thermodynamic data associated with broad ranges of composition. Nothing less than data covering the entire composition range of the binary alloys of interest will do.

III. THE EXPERIMENT

A. Introduction to the Literature of High-Temperature, Solid-State Cells

The solid-state, electrochemical technique has found a very broad range of uses. Application to thermodynamics includes the determination of Gibbs energies of formation of binary and ternary oxides, of silver chalcogenides, and of metal fluorides. It can further be used to determine activities of components in alloys and the activity of oxygen in liquid and solid metals. Applications in solid-state kinetics also exist, for example, the measurement of oxygen diffusion in metals at high temperatures, the measurement of reaction kinetics of product layer formation, and even the combination with a Knudsen cell to investigate vaporization kinetics. All these extensive and varied uses, particularly in the cases of alloy and oxide thermodynamics, have prompted the publication of several reviews. H. Rickert (39) has reviewed all of the above applications on a brief, elementary level. More extensive reviews of intermediate difficulty have been compiled by H. Schmalzried (40), R. A. Rapp and D. A. Shores (41), and W. L. Worrell (42). F. A. Kröger's review (43) deals also with the theories associated with solid-state electrochemistry and is written on a higher level of sophistication than the other reviews mentioned. The majority of the thermodynamic work has employed solid oxide electrolytes, and T. H. Estell and S. N. Flengas have devoted an entire review (44) to the transport and electrical properties of these materials. Worrell (45) has discussed some of the difficult experimental problems associated with the use of oxide electrolytes

to obtain reliable thermodynamic data. Lastly, a prominent and expanding practical application of solid electrolyte cells is their use as electrochemical sensors for solute elements in metallurgical melts (46-48). Such devices allow quick, in situ measurement of solute activities.

The most extensively used solid oxide electrolytes are calcia-stabilized-zirconia ($ZrO_2 \cdot CaO$) and yttria-doped-thoria ($ThO_2 \cdot Y_2O_3$). Some variation in additive to the ZrO_2 and ThO_2 occurs. The complete material properties of ZrO_2 and some of its binary systems have been reviewed by R. C. Garvie (49); the same has been done for ThO_2, Y_2O_3, and their binary system by R. C. Anderson (50). Electrolytes based on ZrO_2 or ThO_2 are used in this work. The most important difference between the two is that ThO_2-based electrolytes are not reduced to sub-stoichiometric oxygen content as easily as ZrO_2-based electrolytes are. The ThO_2-based systems are thus able to maintain essentially complete ionic conductivity at lower oxygen activities than the ZrO_2-based systems (51). This condition is necessary to obtain an emf which can be used to calculate thermodynamic data.

B. Choice of the Ta-Ir Binary System

The decision to investigate the thermodynamics of the Ta-Ir system instead of other possible choices is based primarily on two criteria. First, since thermodynamic data are required across the complete composition range of the system, the emf technique must be applicable throughout this range. The experimental configuration (vide infra) involves the determination of the equilibrium oxygen activity arising from a Lewis-acid-base alloy in contact with the oxide of its acidic metal.

Use of third and fourth group metals was avoided because such combinations at acid rich alloy compositions would result in such low oxygen activities that even ThO_2-based electrolytes would develop too much electronic conductivity to be useful (51). A fifth group metal was selected for an acid to avoid this problem. The minimum oxygen activity encountered in the alloy composition range would be that of the fifth group metal and its oxide, and it is well-established that ThO_2-based electrolytes are usable with such systems (42, 52). Upon meeting this first criterion, the second requires that the final choice of system ought to maximize the stability arizing from the Lewis-acid-base effect to aid future bonding model building. According to previous arguments in II-B, 5d metals were selected. This implies Ta from the fifth group and the 5d metal with which it is expected to have the strongest interaction, viz., Ir.

N. J. Grant and co-workers (53) have done a fine job on the determination of the Ta-Ir phase diagram, shown in Figure 6. They found four intermediate phases listed in Table 3 according to their Pearson nomenclature and structure type (54). Grant's lattice parameters are included. Further information exists on the structure of α_1 (55) and close-packed ordered AB_3 compounds which includes α-$TaIr_3$ (56).

There are no known thermodynamic data associated with the Ta-Ir system in the literature.

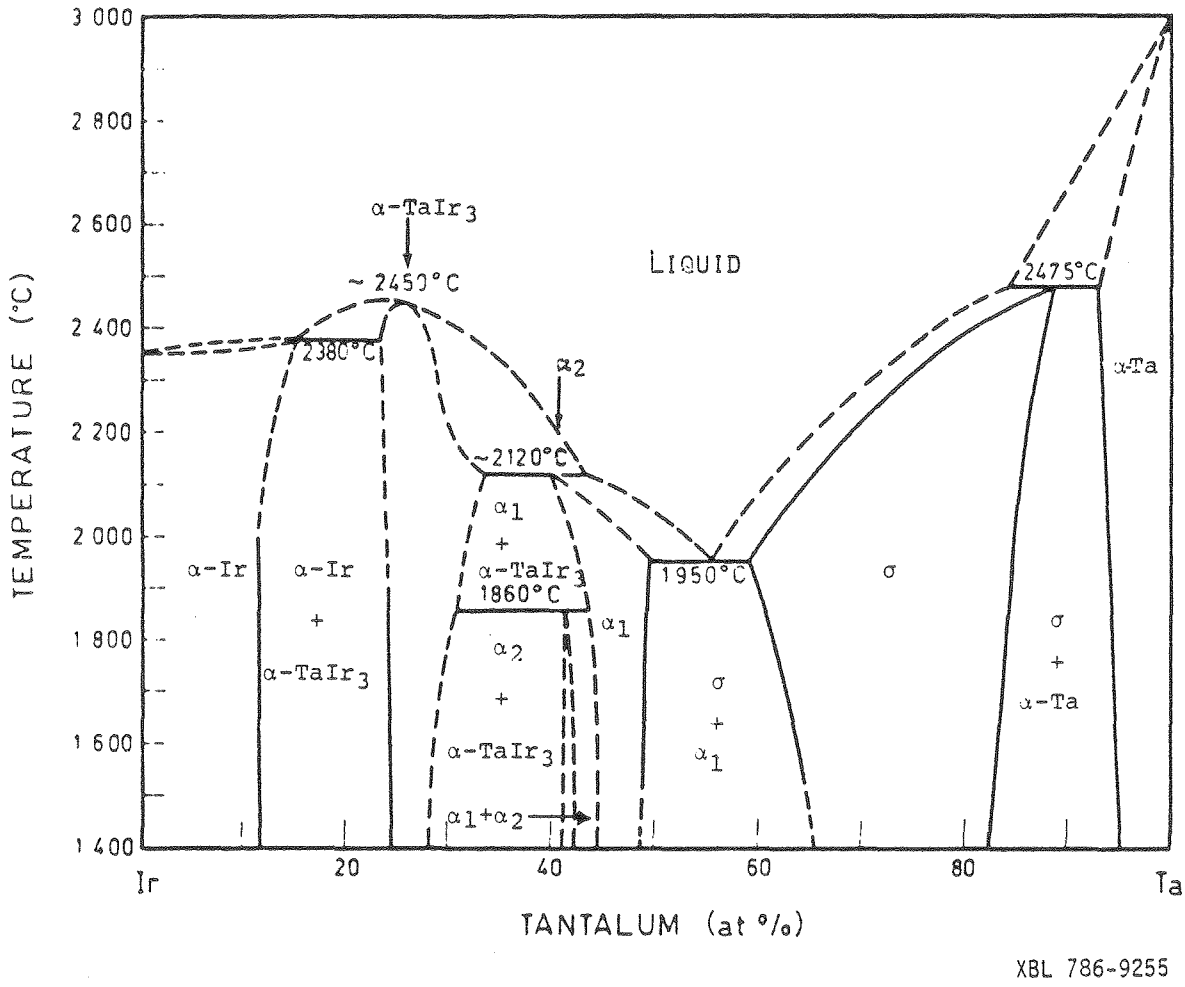

Figure 6. The Ta-Ir phase diagram (53).

Table 3. Description of intermediate phases in the Ta-Ir phase diagram and of α-Ir (53).

Phase and Structure	Ir a/o	Lattice Parameters A			Precision	
		a_o		c_o	±0.004	
σ	20.0	9.968		5.197		
tP30	25.0	9.928		5.159		
(FeCr)	30.0	9.888		5.121		
α_1		a_o	b_o	c_o	a_o,b_o	c_o
oP12 (α_1-TaRh)	57.0	2.830	4.803	13.661	±0.002	±0.006
α_2		a_o	c_o	c/a	a_o,c_o	
tetragonal	59.0	3.988	3.859	0.967	±0.002	
α-$TaIr_3$						
cP4	70	3.907			a_o	
($AuCu_3$)	75	3.886			±0.002	
α-Ir						
cF4	90	3.857			±0.002	
(Cu)	100	3.839				

C. Conceptual Description of Experimental Approach

Several different electrochemical cells were investigated during the course of this work to define errors and to find a good combination of an oxide electrolyte and electrodes which could practically produce the data of interest. Cell I is representative of this search:

$$NbO_2,\ Nb_2O_{4.8}|ZrO_2\text{-}CaO|Ta(Ir),\ Ta_2O_5. \qquad \text{I}$$

It is composed of three tablets. The oxide-ion-conducting, solid electrolyte is $ZrO_2 \cdot CaO$ (57). The two phase mixture of niobium oxides represented on the left is a reference electrode which provides a known oxygen activity (58). The alloy-oxide electrode is an equilibrated mixture of a one - or two-phase Ta-Ir alloy, Ta(Ir), and Ta_2O_5.

Data reduction requires the virtual chemical reaction which would occur if the external circuit of Cell I were closed. The half-cell reactions are

$$\text{anode:} \quad 6.25\ NbO_2 + 2.5O^{2-} = 3.125Nb_2O_{4.8} + 5e^-$$
$$\text{cathode:} \quad 5e^- + 0.5\ Ta_2O_5 = 2.5O^{2-} + Ta(Ir)$$

which lead to a cell reaction of

$$6.25\ NbO_2 + 0.5\ Ta_2O_5 = 3.125\ Nb_2O_{4.8} + Ta(Ir). \qquad (1)$$

Reaction (1) is the actual cell reaction only if the Ta-Ir alloy is composed of a single phase. For those alloy compositions that yield two metal phases, restrictive conditions cause a more complicated cathode

reaction. At a given temperature, the phase rule uniquely fixes the composition of each alloy phase (59). In order to maintain compositional invariance, a certain amount of the Ta-poor alloy phase is mixed with the Ta resulting from the reduced Ta_2O_5 to form an alloy with a composition identical to the Ta-rich alloy phase. Thus only relative amounts of phases change, not their compositions. The actual cell reaction involving a two-phase alloy is then

$$6.25\ NbO_2 + (Z-1)\ TaIr_x + 0.5\ Ta_2O_5 = 3.125\ Nb_2O_{4.8} + ZTaIr_y \qquad (2)$$

where $TaIr_x$ is the composition of the Ta-poor phase and $TaIr_y$ is that of the Ta-rich phase, and Z is given by

$$(Z-1)x = Zy \qquad (3)$$

to balance the Ir. If one wishes to represent solely the Gibbs energy change associated with reaction (2), it can be reduced to reaction (1) in appearance by considering the alloys to be solutions of two components, rather than two compounds, and noting that each component has the same chemical potential in both phases.

Assuming the elctrolyte to be an ionic conductor, the Gibbs energy change of the virtual cell reaction, ΔG, is -nFE where n is 5 equivalents passed in this case, F is the Faraday (23,061 cal/volt•equivalent), and E is the measured open circuit voltage. The relative partial molal Gibbs energy of Ta, $\Delta\overline{G}_{Ta}$, is related to E and the standard Gibbs energies of formation of Ta_2O_5, NbO_2, and $Nb_2O_{4.8}$ by Eq. (4),

$$\Delta\bar{G}_{Ta} = RT\ell na_{Ta} = 3.125\ (2\Delta G^{\circ}_{f}[NbO_2] - \Delta G^{\circ}_{f}[Nb_2O_{4.8}]) + 0.5\ \Delta G^{\circ}_{f}[Ta_2O_5] - 5FE. \quad (4)$$

This expression for $\Delta\bar{G}_{Ta}$ holds for reactions (1) and (2), i.e., for single and two-phase alloy cells as implied at the end of the last paragraph. To obtain the relative partial molal entropy and enthalpy of Ta, $\Delta\bar{S}_{Ta}$ and $\Delta\bar{H}_{Ta}$, for a single phase alloy cell, Eq. (5)

$$\Delta\bar{S}_{Ta} = -\ (\partial\Delta\bar{G}_{Ta}/\partial T)_{X_{Ta}} \quad (5)$$

and Eq. (6)

$$\Delta\bar{H}_{Ta} = \Delta\bar{G}_{Ta} + T\Delta\bar{S}_{Ta} \quad (6)$$

may be used; but they are inapplicable to a two-phase alloy cell because both $\Delta\bar{H}_{Ta}$ and $\Delta\bar{S}_{Ta}$ have different values in each of the two alloy phases. In fact, no knowledge of partial molal quantities other than $\Delta\bar{G}_{Ta}$, may be obtained from measurements on a two-phase alloy cell. The temperature derivative of the cell emf would yield the entropy change for reaction (2). The temperature derivative of the right side of Eq. (4) which is used to calculate $\Delta\bar{G}_{Ta}$ for both types of cells leads to the integral entropy change for the reaction

$$ZTaIr_y = (Z-1)TaIr_x + Ta. \quad (7)$$

The entropy changes of reactions (2) and (7) result from the above temperature derivatives only if the alloy compositions do not vary within the temperature range of measurement. Giauque has shown that the interpretation of emf temperature dependence of the two-phase alloy cells is more complicated if alloy composition does vary within the temperature range

of measurement (60). Still, though, only integral quantities may be obtained. Values for $\Delta\bar{S}_{Ta}$ at phase boundaries may be determined by extrapolation of single-phase alloy cell data obtained within the phase of interest.

Application of the Gibbs-Duhem equation to the Ta activity determined from Eq. (4) yields the Ir activity and $\Delta\bar{G}_{Ir}$ as functions of composition (61, 62). Then $\Delta\bar{S}_{Ir}$ and $\Delta\bar{H}_{Ir}$ may be obtained from equations analogous to (5) and (6). As noted earlier in II-C, the behavior of these quantities as functions of composition is of special concern. Application of the definition of relative partial molal quantities allows calculation of the integral quantities for an alloy of particular composition. For example, the standard Gibbs energy of formation of $TaIr_3$, $\Delta G^\circ_f[TaIr_3]$, is given by

$$\Delta G^\circ_f[TaIr_3] = \Delta\bar{G}_{Ta} + 3\,\Delta\bar{G}_{Ir} \quad . \tag{8}$$

Thermodynamic data on oxides is necessary for the application of Eq. (4). Gibbs energy data on the niobium oxides couple has been reviewed by Worrell (58). The JANAF Thermochemical Tables (63) presently give the most reliable value for $\Delta G^\circ_f[Ta_2O_5]$.

D. Apparatus

A device was constructed to position and contain the three tablets composing the solid-state cell; its design is essentially that of Meschter (37, 64). The cell apparatus is shown in Figure 7B (top part) and Figure 7A (bottom part). Each figure is annotated numerically with the same index system. First, refer to Figure 7A. The three tablets, the electrolyte[13] with an electrode[14] on both sides, are sandwiched between two 20 mil thick Pt discs[10] which act as electrical contacts and then between two alumina discs[12]. This arrangement is held in compression between the flat, circular alumina plate[15] and the alumina compression tube[6]. The 20 mil diameter, Pt leads used to measure the cell emf are carried to the tablets by a double-bore, alumina insulator[7]. The leads are covered with alumina beads[11] upon exiting the insulator and then are spot-welded to the Pt discs[10]. A Pt-Pt+10% Rh thermocouple, also 20 mil diamter wire and carried by a double-bore, alumina insulator[5], is positioned with its bead 1/4" from the electrolyte[13] to measure cell temperature. Returning to the compressive mechanism of the tablets, the circular plate[15] is supported on two Ta nuts[16] screwed onto the threaded ends of the alumina tension rods[3]. Referring to Figure 7B, the rods lead up to the water-cooled cell cap[22] (which is made of stainless steel but should have been made of brass, a much better thermal conductor). Household springs[28], with a coiled section 3/8" × 1/2" long and "degalvanized" in HCl, hang from the cell cap by mounted eyes. The rods are hooked onto the springs via stainless steel nuts with eyes[29]. Clearly, if the compression tube[6] is moved downward with respect to the

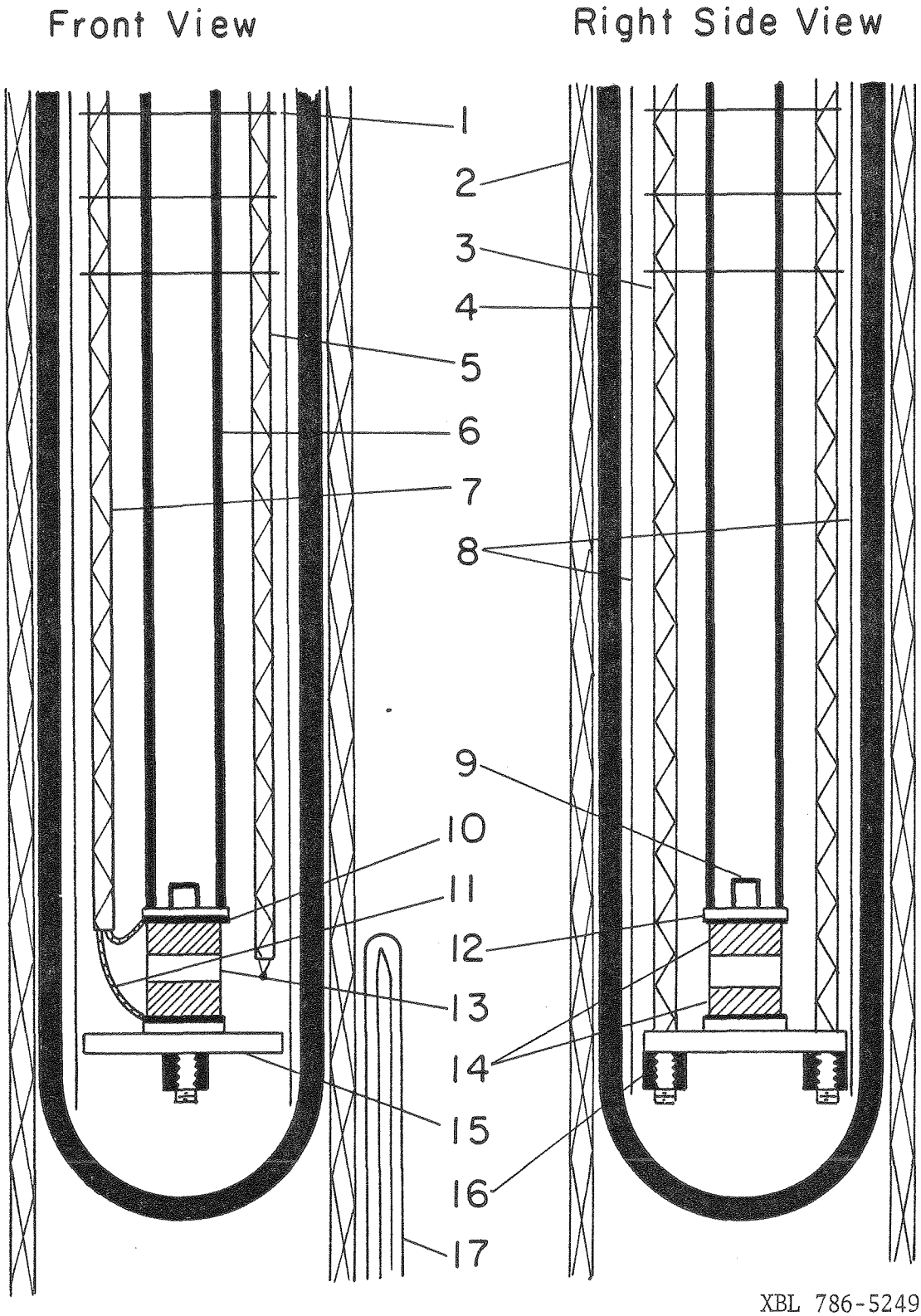

Figure 7A. Cell apparatus, bottom end.

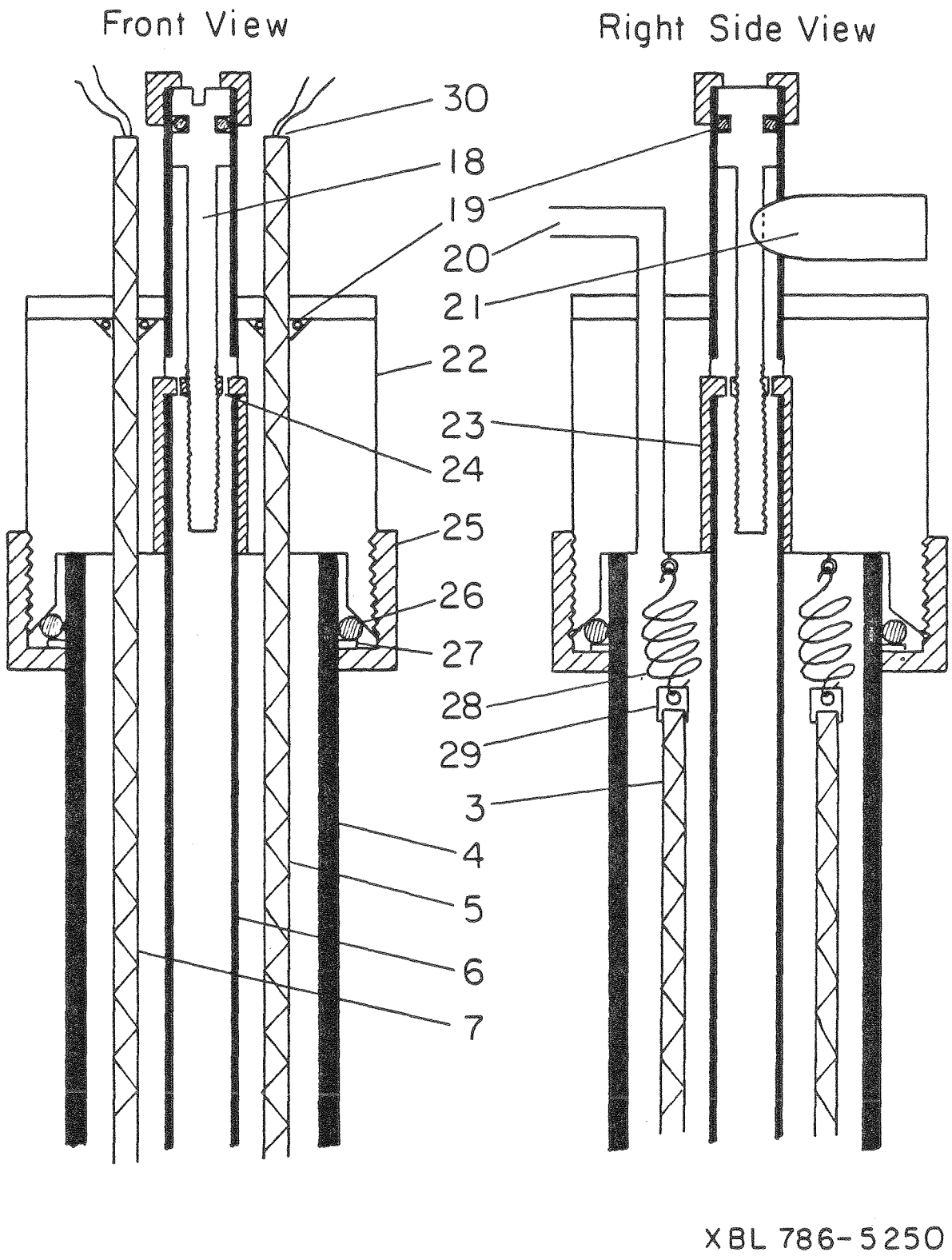

Figure 7B. Cell apparatus, top end.

Index for Figure 7A and 7B.

[1] Tantalum heat shields
[2] Inconel 601 furnace tube
[3] Alumina tension rods
[4] Closed-one-end, alumina containment tube
[5] Alumina insulator containing thermocouple
[6] Alumina compression tube
[7] Alumina insulator containing emf leads
[8] Tantalum foil internal getter
[9] Slots for inert gas passage
[10] Platinum discs
[11] Alumina beads covering emf leads
[12] Alumina discs
[13] Electrolyte
[14] Electrodes
[15] Circular alumina plate
[16] Tantalum nuts
[17] Controlling thermocouple
[18] Compression control bolt
[19] Greased O-rings
[20] Inert gas inlet
[21] Intert gas outlet
[22] Cell cap
[23] Brass sleeve
[24] Holes for inert gas passage
[25] Brass nut
[26] Ungreased Viton O-ring
[27] Brass ring
[28] Springs
[29] Eye-nuts
[30] Epoxy seals

cell cap[22], the springs stretch and the tablets are compressed. The function of the compression control bolt[18] is to supply such motion. A brass sleeve[23] which fits on the end of the compression tube and snugly into the cell cap provides a threaded hole in the top end for the compression control bolt. Rotation of this bolt by means of a screw-driver slot in its head moves the compression tube up or down, thus varying the magnitude of compression on the tablets.

The cell is run in a flowing, highly purified, inert gas atmosphere; so it is encased in a closed-one-end, alumina tube[4] sealed to the cell cap with a Viton O-ring[26]. The large brass nut[25] slides against the flat, brass ring[27] which evenly presses the O-ring against the beveled part of the cell cap and containment tube. The use of T-Apiezon or Dow-Corning grease on this seal, which was 55° C during cell operation, interfered with the cell emf. A good seal was obtained without grease by polishing the alumina tube surface with fine diamond wheels and finally 6μ diamond paste. The O-rings sealing the alumina insulators and the compression control bolt[19] are greased with L-Apiezon and maintained at 18° C by the water-cooling. The insulator bores from which the wires exit to the outside[30] are sealed with expoxy, which was baked overnight at 90° C after drying to degas it.

The inert gas flows through the inlet[20], down the space between the compression tube[6] and containment tube[4], through slots[9] at the bottom of the compression tube, up in the tube and through holes in the brass sleeve[24], and through the outlet[21], which is also used to pull a vacuum. Tantalum heat shields[1] are placed above the tablets to minimize temperature decline above them, to act as baffles to help

heat the inert gas, and to getter oxygen. Tantalum foil[8] was also used as an internal getter for oxygen, below the shields, in most of the high-temperature region. Except for the rods and insulators which were 99%, all alumina parts mentioned in this description are 99.8% Coors alumina.

Either helium or argon is used for the flowing, inert gas atmosphere. Table 4 displays purity specifications to which the gas suppliers comply. Analyses ran on particular cylinders are also shown. The inert gas purification scheme is as follows: First, the gas is passed through a 1.3" ID × 25" long reactor at room temperature filled with fully activated Linde 5A molecular sieve. Dehydration occurs down to a minimum water content of 0.02 ppm if equilibrium is reached in the reactor. Second, the gas passes through an alumina tube (1" ID) filled with chips of an 87-1/2% Zr-12-1/2% Ti alloy (Oregon Metallurgical Company). This getter is maintained at 800°C by a 12" tube furnace. Third, the gas passes through another identical gettering furnace maintained at 500°C. This furnace is meant to getter hydrogen, for which the alloy has very little capacity at 800°C (65). The inert gas is routed to the cell cap in thoroughly degreased, stainless steel tubing which has been degassed at 160°C. Bellows seal valves are used in the gas line, and the connections to the cell cap are made with flexible, stainless steel tubing and Viton O-ring fittings.

The cell apparatus is heated by a Marshall resistance furnace, 26" long with a 2.5" diameter bore containing Super-Kanthal windings. Shunt resistors are placed across external connections positioned along the windings to extract heat and flatten the temperature distribution.

Table 4. Inert gas specifications and individual cylinder analyses.

Specifications (ppm by volume):

		H_2O	N_2	O_2	H_2	CO_2	CH_4*
Argon, Pacific Oxygen Co.	max.	1.5	5	3	1	.5	.5
	typ.	.25	5	2	1	.5	.5
Extra pure helium, Union Carbide Corp, Linde Div.	max.	5.3	5	2			none
	typ.	1.0	4	1			
Matheson purity argon, Matheson	max.	.63	5	1	1	.5	.5

Cylinder Analyses (ppm by volume):†

	H_2O	N_2	O_2	H_2	CO	CO_2	CH_4*
Argon, Pacific Oxygen Co. #1273507	.6	<4.0	1.2	<.1	<.5	<.1	<.1
Extra pure helium, Union Carbide, Linde #51131				<.5	<.5	1.1	<.1
Matheson purity argon, Matheson, #33207T				<.1	<.5	<.1	<.1

*hydrocarbons as CH_4.

†H_2O, O_2, N_2 analyses by Pacific Oxygen, Oakland, CA; the others by Matheson, Newark, CA.

An Inconel 601 pipe (2.375"OD, .154" wall thickness) was placed in the furnace bore (Figure 7A, 2) to even temperature variations caused by the large, exposed windings and to aid the creation of a constant temperature zone. It also shields the electrical leads from the magnetic field of the furnace. The cell temperature is controlled to within a variation of 2C° by a Barber-Colman Model 477P proportional controller. The controlling thermocouple (Figure 7A, 17) is positioned just outside the windings, adjacent to the tablets. The cell temperature can be varied automatically between any two selectable temperatures at any rate between 50 to 250 C°/hr. This is accomplished by placing an extra, variable voltage source in the controlling thermocouple circuit which adds to the thermocouple voltage. The set-point of the controller is always kept at 1200° C, a temperature higher than any used. Various constant temperatures are associated with various constant magnitudes of the extra voltage. The controller senses the sum of the extra voltage and the controlling thermocouple voltage which is constant and always equal to the voltage that the controlling thermocouple would produce if it were sensing 1200° C rather than the actual temperature. To effect a temperature change, the extra-voltage source generates a ramp signal starting from its initial value. The magnitude and sign of the ramp slope are chosen to effect the desired rate and direction of temperature change, respectively.

Raw data consist of cell temperature and cell emf. The voltage of the Pt-Pt + 10% Rh thermocouple (Engelhard) used to determine the cell temperature is measured by a Leeds & Northrup 8686 millivolt potentioneter. An ice bath reference is used. The cell emf is measured by a Keithley 660

guarded dc differential voltmeter. A Honeywell Electronik 19 recorder is used when the cell emf requires recording. Cables used between the voltmeter posts and Pt emf leads consist of a twisted pair with a wrap-around shield (leakage resistance $>10^{13}$ ohms). The shield, the voltmeter chassis and low impedance post, the cell cap, the Inconel 601 pipe, and all metal shells in the vicinity are grounded to a common ground according to proper grounding and shielding practice (66).

E. Preparation of Cell Tablets

E.1 Materials Used

Raw materials used to prepare cell tablets are listed in Table 5 with their form, purity, and supplier. Instances in Table 5 involving an unknown producer required procurement of spectrographic analyses or purchasing specifications followed by Lawrence Berkeley Laboratory. A spectrographic analysis was also run on the ZrO_2 because moderate levels of the analyzed contaminants interfere with the functioning of the ZrO_2 •CaO electrolytes made from it. This information is shown in Table 6.

Niobium dioxide powder was made by reducing Nb_2O_5 powder for 2-1/2 hr. at 1120° C in tank hydrogen (1 ppm H_2O, 1 ppm O_2). Weight change indicated stoichiometric conversion. An NbO-NbO_2 mixture was made by reducing Nb_2O_5 under palladium-diffused hydrogen for 6 hr. at 1230° C.

Table 5. Raw materials.

Material	Form	Purity	Supplier
Ir	Powder, -325 mesh	99.7	Lawrence Berkeley Lab stores
Ir	Sheet, .02" thick	99.8	Englehard Indust. Carteret, N.J.
Ta	Powder, -325 mesh	99.9	Orion Chemical Co. Glendale, CA
Ta	Sheet, .01" thick	99.9	Lawrence Berkeley Lab stores
Fe	Powder, -250 mesh	99.95	Materials Research Corp. Orangeburg, N.Y.
Ni	Powder, -325 mesh	99.5	A.D. Mackay, Inc. New York, NY
Mo	Powder, 10μ	99.9	Orion Chemical Co.
Nb	Powder, -270 mesh	99.8	Wah Chang Corp., Albany, Ore.
ZrO_2	Powder, -325 mesh	99.9	Wah Chang
Nb_2O_5	Powder, -325 mesh	99.9+	Alfa Ventron, Beverly, Mass.
Fe_2O_3	Powder, -325 mesh	99.8	Alfa Ventron
Ta_2O_5	Powder, -325 mesh	99.9	Orion Chemical
$CaCO_3$	Powder, -400 mesh	Analytical Reagent	Mallinckrodt Chemical Works St. Louis, Mo.
NiO	Powder, -325 mesh	Reagent	Matheson, Coleman, & Bell Los Angeles, CA
MoO_3	Powder, -325 mesh	Analyzed Reagent	J. T. Baker Chemical Co. Phillipsburg, NJ

Table 6. Impurity content of selected materials.

Laboratory specification MEL-500031B applied to purchase of Ta, maximum level of impurities (ppm/wt):

Nb	W	Mo	Zr	Si	Ca	Fe	Mg	O	N	C	H	Total interstitials
1000	500	200	50	30	25	25	5	60	50	40	10	<100

Spectrographic analyses of Ta and Ta_2O_5 from Orion (ppm/wt):*

	Fe	Cr	Ni	Si	Nb	Ti	Zr	Al	Cu	Mg	Ag	Ca	Mn	C†
Ta	<100	<100	100	100	<100	<50	<100	<100	<100	<50	<50	<100	<100	35
Ta_2O_5	<100	<100	<50	700	<100	<50	<100	<100	<100	<50	<50	<100	<100	

Spectrographic analysis of Ir powder from LBL stores (ppm/wt):*

Pt	Pd	Rh	Ru	Mg	Si	Fe	C†
2000	<100	300	<100	50	50	<100	40

Spectrographic analysus of Wag Chang ZrO_2 powder (ppm/wt):*

Nb	Co	Fe	Mn	Mo	Ni	Si	Ti	V
<50	<20	<50	10	<50	<50	1000	<20	<50

*Spectrographic analyses performed by G. Shalimoff, Lawrence Berkeley Laboratory.

†Carbon analyses performed by D. McCoy, Lawrence Livermore Laboratory.

E.2. Preparation of Electrolytes

Electrolytes of the composition $(ZrO_2)_{.85}$ $(CaO)_{.15}$ were prepared. This is not the composition associated with maximum ionic conductivity (67); however, it is most commonly used, evidently because it is kinetically stable with respect to decomposition. The fluorite eutectoid field of the ZrO_2-CaO system (68), of which $ZrO_2 \cdot CaO$ electrolytes are a part, is thermodynamically unstable at temperatures commonly used in cell work; and smaller CaO contents (which have higher ionic conductivities) tend to destroy the kinetic stability of the fluorite phase (49).

The method of preparing the $ZrO_2 \cdot CaO$ electrolytes is based on that of R. Rapp (69). Appropriate amounts of ZrO_2 and $CaCO_3$ were dry mixed in a polyethylene bottle by adding a few alumina balls to the powder and tumbling for 6 hr. The powder was then isostatically compacted in a single mass at a pressure of 50,000 psi and fired for 48 hr. at 1000° C. The mixture reacted to form ZrO_2 and $CaZrO_3$. The mass was then ground to a powder with an alumina mortar and pestle, placed in a polyethylene bottle with a large number of stabilized zirconia mixing balls (Zircoa) and distilled water, and vibration ball milled for 6 hr. Next the slurry was passed through a 400 mesh screen to remove the plastic, and allowed to settle. The remaining plastic floated to the top and was skimmed off, and the mixture was evaporated to dryness. The average particle size was found to be 0.7μ, as measured by a Fisher apparatus. One w/o naphthalene was then added by stirring it into the powder with ether. When the powder was completely dry, it was uniaxially pressed in a steel die of .52" diameter at a pressure of 40,000 psi. The naphthalene probably helped the powders to compress; but, also, if

it was absent, the die and plunger galled. Resulting tablets were about 3/16" thick. Impurities from the steel die were scraped off. (Somewhat less steel rubbed off on the tablets if the die was lightly lubricated with a solution of 2 gm naphthalene dissolved in 50 ml of benzene.) The tablets were then placed in toy balloons which were completely collapsed and tied off. Isostatic pressing at 100,000 psi followed. The tablets were then heated for 1 day at 100° C to vaporize the naphthalene. Sintering was done in a Bickley gas-fired kiln for 4 hr. at 1750° C. The kiln could be brought down to 1200° C in two hours, shut off, and allowed to cool to room temperature without cracking the electrolyte tablets.

The resulting tablets were 91% of theoretical density. A powder X-ray spectrum taken on a Picker diffractometer, Model No. 3488K, showed only that of the fluorite phase (67). (The Picker diffractometer was used for all the x-ray spectra taken in this work.) Zirconia with a 0.5 w/o Si impurity yielded tablets of 93% theoretical density under identical processing conditions, but the use of these tablets in cells was abandoned. On the other hand, 3 to 4% of theoretical density was lost when sintering ZrO_2+$CaCO_3$ compacts or ZrO_2+CaO compacts in which the CaO was made by $CaCO_3$ decomposition. Prereaction of powders was necessary to achieve sufficient density to isolate the pores from one another. A non-interconnected pore phase was required to prevent gas phase transport of oxygen through the body of the electrolyte. Such a process would have disturbed the equilibria maintained at the electrode-electrolyte interfaces.

The $ThO_2 \cdot Y_2O_3$ electrolytes used in this work were borrowed from W.L. Worrell and were 99% dense.

E.3. Preparation of Various Electrodes Used for Reference and Testing

Electrode preparation followed a general method for each type of electrode prepared. Two powdered materials were dry mixed with a few alumina balls in a small jar on a tumbler for 5 hr. The powders were then uniaxially pressed in a 1/2" or 7/16" diameter steel die at 75,000 psi to form tablets close to 3/16" thickness. The tablets were then placed on an alumina dish and heated at high temperature to equilibrate and sinter them. The heating was done in a tungsten-ribbon resistance furnace which maintained a vacuum of 10^{-6} torr. The heat shields were made of Mo.

To prepare Ta, Ta_2O_5 electrodes, Ta and Ta_2O_5 powders were mixed according to a weight ratio of 3/1 (metal/oxide) which yielded a volume ratio of 1.5/1, and then pressed in the 7/16" die. The tablets were annealed at 1100° C for 24 hr. and then at 1000° C for 24 hr. X-ray spectra showed only Ta and β-Ta_2O_5. (The Powder Diffraction File, published by the Joint Committee on Powder Diffraction Standards, was used throughout this work to identify the spectra obtained.)

To prepare Nb, NbO electrodes, enough Nb powder was mixed with the NbO-NbO_2 mixture to ultimately result in what appeared to be, under microscopic examination, a volume ratio of 1.5/1 (metal/oxide). The powder was pressed in the 7/16" die to form the tablets which were annealed at 1250° C for 48 hr. and 1000° C for 24 hr. The long exposure to high temperature was required to exhaust the NbO_2. No reaction with the alumina dish

occurred. Final x-ray spectra taken showed only Nb and NbO.

To prepare Mo, MoO_2 electrodes, the method of Rapp (69) was adopted. Powders of Mo and MoO_3 were mixed according to a weight ratio of 2/1 (metal/oxide). The electrodes, pressed in the 7/16" die, were slowly heated over a day to 1100° C to allow them to degas. Then the temperature was maintained at 1100° C for 20 hr. X-ray analysis showed only Mo and MoO_2).

To prepare Ni, NiO electrodes, powders were mixed according to a weight ratio of 1.33/1 which afforded a volume ratio of 1/1. After pressing, they were heated in a tube furnace at 1200° for 12 hr. in helium with an oxygen pressure of about 10^{-6} atm. They could probably be heated in vacuum without much vaporization; but, early attempts to prepare them when only a dirty, "inert" atmosphere instead of a good vacuum was available in the annealing furnace resulted in pure Ni. Therefore, a more oxidizing atmosphere was used.

To prepare Fe, FeO electrodes, the best method used was the following: Powdered Fe containing only 18 ppm C was mixed with Fe_2O_3 which had been annealed in oxygen for 6 hr. at 900° C to rid it of a C impurity of 70 ppm. The weight ratio used was 2/1. The powders were pressed in a 1/2" steel die because the tablets shrank upoun annealing to a diameter of 7/16", and this diameter matched that of the electrolyte. The heating scheme consisted of a slow temperature rise to 850° C which was maintained for 24 hr. The temperature was then increased to 1050° C and held for another 24 hr. Room temperature x-ray analysis showed no hemitite (Fe_2O_3), but only bcc Fe and magnitude (Fe_3O_4) because wüstite (FeO) is unstable below 560° C. In order to completely rid the electrode of its capacity to

generate CO by reaction of the C impurity with the oxide phase, re-crushing to powder and reannealing twice was expected to be necessary, after discovering that a single annealing was insufficient. The concern for C is explained in Chapter IV.

Lastly, to prepare NbO_2, $Nb_2O_{4.8}$ electrodes, powders of NbO_2 and Nb_2O_5 were mixed in a weight ratio of 1.9/1 (NbO_2/Nb_2O_5) which, upon some consumption of NbO_2 during equilibration, yielded equal volumes of the oxide phases. The powder mixture was pressed in a 1/2" die (to offset shrinkage) and further compressed isostatically at 100,000 psi because there was no ductile metal phase in this electrode. Higher temperatures were used because achieving equilibrium between niobium oxides is difficult (70). The heating scheme was 16 hr. at 1250° C, 6 hr. at 1385° C, 18 hr. at 1250° C, and 43 hr. at 1100° C. Discoloration of the alumina dish occurred, but the contacting face of the electrode was not visibly altered. This face was ground off anyway. X-ray analysis showed only tetragonal NbO_2 and $Nb_{12}O_{29}$.

E.4. Preparation of Alloy-Oxide Electrodes

Three Ta-Ir alloy compositions were prepared. Referring to the phase diagram in Figure 6, single-phase compositions of 2 a/o and 5 a/o Ta and a two-phase composition of 17.4 a/o Ta were made. The single-phase alloys were made by mixing the proper proportions of Ta and Ir powders. Each mixture was compacted isostatically at 100,000 psi in a small rubber mold. The compacts were sintered at 1820° C for 19 hr. in a tungsten-mesh resistance furnace under a vacuum of 10^{-6} torr. They were supported in a Ta cradle which was only slightly attacked. Proper

weights of pieces of Ta and Ir sheet were cut out for the two-phase composition. Equal volumes of the α-Ir and $TaIr_3$ phases exist at this composition. The sintered compacts and pieces of sheet were arc-melted with a non-consumable tungsten electrode on a water-cooled copper hearth in an argon atmosphere gettered with Zr-Ti alloy. The alloy buttons formed were flipped and remelted 5 times. Weight losses were only 0.3% or less in each case. The buttons were then homogenized at 1750° C for 30 hr. and then at 1500° C for 48 hr. This was the same scheme that Grant used in his phase diagram study. The compositions in the two-phase alloy are uniquely set by nature. The compositions of the single-phase alloys were taken as weighed because virtually no chance for composition change was available. The very small weight loss which occurred during arc-melting was attributed to splattered material of the same composition as the whole button because the powders composing the compacts were well-mixed and substantially homogenized before arc-melting.

Next the alloy buttons were pulverized. The single-phase alloys were somewhat ductile. They were reduced to -115 mesh by arduous pounding in a metallurgical mortar (Rene 41) and pestle (304 stainless steel) immersed in liquid nitrogen. The alloy powder was washed in hydrochloric and nitric acids separately to dissolve the constituents of the mortar and pestle. Neither elemental Ta nor elemental Ir react with these acids, but Ir reacts slightly with aqua regia (71). The powders were then boiled in distilled water and dried. The two-phase alloy was brittle. It was reduced to -400 mesh with a cobalt-bonded titanium carbide (Kennametal K11) mortar and pestle. Resulting powder was magnetic, so it was washed with nitric acid.

The alloys were then mixed with two types of powdered Ta_2O_5. One type was white and oxygen rich. The other had been annealed in palladium-diffused hydrogen for 8 hr. at 1100° C roughly at the oxygen activity of $NbO-NbO_2$ which was lower than that ultimately expected in the alloy-oxide electrodes. It was grey and oxygen poor. A 1.5/1 (metal/oxide) volume ratio was used for the -115 mesh powders and 1.8/1 was used for the -400 mesh powder. Corresponding weight ratios were 4.1/1 and 4.8/1, respectively. The electrodes were pressed in the 7/16" die and then isostatically pressed at 100,000 psi. The electrodes were equilibrated at either 925° C or 1125° C under a vacuum of 10^{-6} torr in the tungsten ribbon furnace. They did not react at all with the alumina dish. Various times up to 300-400 hr. were used to check for attainment of equilibrium. The use of two types of Ta_2O_5 provided another check because equilibrium had to be approached from two compositional extremes. Further discussion of equilibrium of alloy oxide electrodes occurs in Chapter IV. The electrodes were occasionally X-rayed and constantly metallographically examined after annealing to check for the nucleation of new phases or the disappearance of old ones. No tenary oxides were ever seen.

F. Procedures Used to Measure the Cell EMF

The rationale for these procedures will be examined further in Chapter IV.

Before the electrolyte and electrodes were put into the cell apparatus, their contacting faces were polished with specially developed techniques designed to minimize surface porosity and maximize overall

flatness. A detailed description of the procedures, the results of which were highly reproducible, is given in the appendix. Thus, interfacial contact and "tightness" was at a maximum for the geometry used.

The cell was next assembled, placed in the containment tube, and connected to the inert gas line. Leak checking was accomplished via a well-trapped mechanical pump and a thermocouple vacuum gauge. The rate of gas evolution inside the system decreased with time of pumping, indicating vacuum tightness. A gas flow rate of 30 cc/min was then started to quickly sweep out the water desorbing from the alumina while the temperature rose. (All flow rates are reported at 21° C, 1 atm.) The temperature increased at a rate of 200C°/hr if a $ZrO_2 \cdot CaO$ electrolyte was used or 75C°/hr if $ThO_2 \cdot Y_2O_3$ was used as the electrolyte.

The procedure required to take emf measurements is described below. Since none of the cells involving alloy-oxide electrodes operated completely successfully, many parts of the complete procedure could not be carried out. What should be done with and expected from a successful cell is therefore described. Meschter's example (37, 64) which involved similar cells is followed here.

Cells are equilibrated initially at about 1000° C under a gas flow of 15-18 cc/min. One or even two days might be required for the cell emf to stabilize. Meschter considered equilibrium "to have been obtained when the measured emf varied by less than 0.3 mV over a 3-hour period." At this point one should determine whether the emf is the result of solely solid-state processes in the electrodes and electrolyte, or is being influenced by impurities in the flowing inert gas. The suspected gaseous contribution to the emf may be greatly changed by sharply increasing the

flow rate from 15-18 to 150-180 cc/min. If the emf does not ultimately restabilize at fast flow to within 1 mV of its original value, the experiment should be terminated because this implies that the emf does not correspond to the cell reaction of interest. Flow rate test failure signifies bad interfacial contact and/or too dirty an inert atmosphere.

A cell which passes the flow rate test should then be cycled in 25-50C° steps to obtain the emf vs. temperature relationship. Points should be approached from both higher and lower temperatures. Agreement of the two directions of approach to within 1 mV is a necessary but not a sufficient criterion which demonstrates the attainment of equilibrium. Approaching points from extremes also allows one to "bracket" the emf-T relationship, thus making it unnecessary to wait for the emf to utterly completely stabilize after a temperature change. Since some of Meschter's runs lasted 3 weeks, experiments might otherwise last for intolerably long times.

The cell was assembled with electrodes in well-defined thermodynamic states. These states must be maintained throughout the duration of the run to associate the measured emf with the cell reaction. To determine that this is so, provided that the cell has passed the flow rate test, polarization and stability tests are required. Since the emf at a single temperature is unique, and emf recorded over 12-24 hr. should show only random variation, probably only within 1 mV. Note that a 2 mV random variation would be acceptable; such a cell would produce data with somewhat larger uncertainties, but a cell with 0.5 mV change in a single direction for 24 hr. would be no good. A good cell should also be able

to recover its original emf under open-circuit conditions if the leads are shorted for 1-2 min, and the cell reaction is allowed to proceed. This could occur only if it were indeed exactly the cell reaction of interest which in fact proceeded when the external circuit was closed.

From Meschter's experience with the Ti-Pt, Zr-Pt, and Hf-Pt systems, long annealing times were expected for the Ta-Ir alloy-oxide electrodes to reach equilibrium. For this reason, successive runs on the same electrode which has undergone further annealing between runs should be made and the resulting emf's compared. Electrodes made from white and grey Ta_2O_5 should ultimately result in identical emf's with sufficient annealing.

After all runs in this work, the electrode and electrolyte faces were examined microscopically to check for any electrode-electrolyte side reactions or phase changes in the electrodes. X-ray analyses after runs were occasional. Observations will be noted later as various cells are considered.

G. Apparatus Check-Out

The temperature distribution inside the containment tube was determined by moving the thermocouple which was used to measure cell temperature along the length of the tube. The maximum temperature difference between opposite ends of the solid-state cell (3/4") was made to be 0.2C° by adjusting the external resistors. The maximum temperature difference between the middle of the cell and either end was 0.3 C°. This situation did not vary with temperature; checks were made between 850 and 1100° C. Also, the following thermocell was run in this temperature range:

$$Fe,FeO|ZrO_2 \cdot CaO|Fe,FeO. \qquad II$$

Voltages measured throughout the range were from 0.00 to 0.03 mV. Usual uncertainties of emf-T relationships are ± 1 mV. The thermoelectric power of $ZrO_2 \cdot CaO$ and $ThO_2 \cdot CaO$ have been measured (72). The largest component of the thermoelectric voltage in cells employing these electrolytes is due to the temperature variation of the chemical potential of oxygen at the electrolyte faces, and this component is quite negligible to the 1 mV uncertainty when the cell is run under the tiny gradients involved here.

The temperature of the solid-state cell itself was assumed to be that measured by the thermocouple suspended in the inert gas atmosphere 1/4" away. To prove this assumption true, the insulator carrying the emf leads was replaced with one carrying a Chromel-Alumel thermocouple (30 gage, B&S). The ends of the inch of bare wire protruding from the insulator were spot-welded to the top Pt disc, and an alumina mixing ball was used as dummy tablets. The Chromel-Alumel thermocouple read 1 C° hotter under helium and 2 C° hotter under argon at 1000° C than the Pt-Pt+10% Rh thermocouple. Neither one was calibrated; these results were taken to be in sufficient agreement. The cell temperature must not vary during flow rate testing. At 1000° C, not even the slightest change (< 3 μV) in the voltage of either thermocouple could be detected when the helium flow rate was increased from 25 to 280 cc/min. The same held true for argon from 25 to 265 cc/min.

Two cells were run to test electrolytes and atmospheric purity:

$$Fe,FeO|ZrO_2 \cdot CaO|Ni,NiO. \qquad III$$

$$Nb,NbO|ThO_2 \cdot Y_2O_3|Ta,Ta_2O_5. \qquad IV$$

The voltage for Cell III was calculated from Worrell's review (58). The cell produced the proper emf to within 1 mV. When the argon (cyl. #1273507) flow rate was changed from 25 to 255 cc/min, the emf of Cell III changed only 0.1 mV. This cell's emf had a slight tendency to decay (1 mV over 40 hr). The cause will be suggested later; nonetheless, Cell III proved that the $ZrO_2 \cdot CaO$ electrolytes made were ionic conductors and non-porous. The borrowed $ThO_2 \cdot Y_2O_3$ electrolyte was contaminated with some transition metal impurity which produced electronic conductivity. The evidence for this was its grey color after Cell IV was run, and the achievement of only 80% of the thermodynamic emf, taken from Worrell (52), during the run. The emf of Cell IV had an amplitude variation of only 0.13 mV over 26 hr. at a constant temperature of 962° C, however. A change of helium (cyl #51131) flow rate from 25 to 280 cc/min resulted in an emf change of only 0.1 mV or less. Ample evidence therefore existed that the inert gas atmosphere was undergoing acceptable purification.

During these cell runs, the furnace power was switched on and off to see if the furnace magnetic field was inducing any stray emf's in the measurement circuit. Cell emf changes, which could be seen to 0.002 mV, were not observed. The measuring cables were also jiggled with no observed effects. The springs were stretched 1/4" to 1/2". No change in emf could ever be seen with this change in cell compression. The inert gas line and cell apparatus were occasionally helium leak checked.

IV. WHAT REALLY HAPPENS IN SOLID-OXIDE-ELECTROLYTE, ELECTROCHEMICAL CELLS

As was implied in III-F, acceptable emf data on the Ta-Ir system are yet to be produced. This chapter is offered as an appropriate, worthwhile replacement, because there are actually so many results to be discussed concerning the functioning of electrochemical cells themselves. The literature is first examined to gather and analyze results obtained from oxide-electrolyte cells employed by various workers to study identical materials. The chapter then proceeds with the identification of the atomic, physical processes which lead to proper and improper cell functioning.

Sources of error are discussed in the light of these processes, and the methods to reduce or eliminate errors are reviewed. Examples in which a particular source of error is operative are presented, as well as the means to correct the error.

A. Problems with Thermodynamic Data Derived from Cell Work

The objective of this particular section is to illustrate the need to understand, discover, and eliminate the sources of error which occur in oxide-electrolyte cell experiments. This is accomplished by presenting the results of various researchers working on the same metal oxide or alloy. The results are compared with one another and/or accepted thermal data to display their consistency and/or accuracy.

First, consider the use of oxide-electrolyte cells to obtain the Gibbs energies of formation of binary metal oxides. Generally, researchers are able to accurately repeat the work of Kiukkola and Wagner (6), who ran cells which used Fe,FeO; Ni,NiO; Co,CoO; and Cu, Cu_2O as the electrodes and $ZrO_2 \cdot CaO$ as the electrolyte; they thus obtained the Gibbs energies of formation of NiO, CoO, and Cu_2O. On the other hand, great difficulty has been encountered by several cell researchers when they attempted to determine the same quantity for MoO_2 and Cr_2O_3. Their results are displayed in Tables 7 and 8. Each researcher determined a ΔG^o_f and represented it as a linear function of temperature within the temperature range of his experiment. The other quantities displayed facilitate evaluation. To produce these quantities, the following calculations were done: At 100K increments, $\Delta H^o_{f,298}$ of Cr_2O_3 or MoO_2 was calculated throughout the experimental temperature range using the researcher's Gibbs energy data and the Gibbs energy functions for Cr, Mo, O_2 (73), and Cr_2O_3 and MoO_2 (63) (third-law method (61)). The values obtained were then averaged, and the mean was used in the tables. The drift of the calculated values of $\Delta H^o_{f,298}$ between the extremes of the temperature range is also shown. Lastly, the accepted value of $\Delta H^o_{f,298}$ (63) was combined with the third-law method to calculate S^o_{298} of MoO_2 or Cr_2O_3 using a scheme analogous to the enthalpy calculations. The drift of $\Delta H^o_{f,298}$ contains information concerning the temperature coefficient in the experimentally determined linear representation of $\Delta G^o_{f,T}$. The coefficient is a constant which represents ΔS^o_f, a quantity which in fact slowly changes through

the experimental temperature range. If the drift is negative, this implies that the experimentally determined ΔS^o_f is algebraically too large, while a positive drift implies the opposite. Drift magnitude reflects the magnitude of the error. If the temperature coefficient is as good as the linear Gibbs energy representation can permit it to be, i.e., the average of $\Delta S^o_{f,T}$ over the investigated temperature range, the drift between the temperature extremes is essentially zero. All this is independent of the experimental enthalpy term. The mean values of $\Delta H^o_{f,298}$ and S^o_{298} of the oxides indicate the accuracy of the Gibbs energy data in the experimental temperature range. The third-law entropy of the oxide is the more sensitive indicator because it experiences a greater relative change from its accepted value when calculated with poor Gibbs energy data.

The cell results on the Gibbs energy of formation of MoO_2 are listed and analyzed in Table 7. The JANAF values of $\Delta H^o_{f,298}$ and S^o_{298} are provided to allow assessment of the experimental Gibbs energy data in the temperature range investigated. Rapp's work (69) was done first (1962); the other researchers account for 15 more years of work, but his remains as the best. The only gross error in $\Delta G^o_{f,T}$ was made by Barbi (80), although ΔH^o_{298} is outside the uncertainty of ± .5 kcal/mole for most of the investigations. The great problem arises in the determination of the correct temperature coefficient. Most are mediocre to extremely bad, such as Fischer's (81). (He references three of his earlier works on $\Delta G^o_f[Mo\,O_2]$ which are of similar quality.) Except for the first three listings, one would have to conclude that systematic,

Table 7. Evaluation of $\Delta G^{o}_{f,T}[MoO_2]$ as determined by several workers using oxide-electrolyte cells.

Workers	ΔG^{o}_{f} = A+BT(cal) Temperature range	$\Delta H^{o}_{f,298}$ (kcal/mole)	Drift (cal/k)	$S^{o}_{298}[MoO_2]$ (cal/k-mole)
JANAF Tables		-140.5±.5		11.95±2
Rapp (69)	-137500+40.0T 1000-1300K	-140.26	.1	11.74
Katayama & Kozuka (74)	-137560+40.31T 1173-1373K	-139.87	1.0	11.47
Berglund & Kierkegaard (75)	-134990+38.48T 1150-1450K	-139.62	-1.0	11.23
Alcock & Chan (76)	-138600+40.0T 1273-1873K	-140.86	1.9	12.21
Drobyshev & Rezukhina (77)	-137580+40.48T 1260-1360K	-139.62	1.4	11.30
Zabeivorota & Lykasov (78)	-138170+40.64T 1123-1973K	-139.35	2.4	11.32
Iwase & Mori (79)	-128800+31.0T 1723-1923K	-139.86	-6.2	11.58
Barbi (80)	-138350+42.5T 800-1200K	-138.55	1.9	10.00
Janke & Fischer (81)	-117280+28.28T 1733-1933K	-140.23	-8.9	11.78

temperature dependent errors are associated with the MoO_2 cell work. Extrapolations to outside the experimental temperature range would be seriously in error.

Cell determinations of the Gibbs energy of formation of Cr_2O_3 are listed in Table 8. The results are much poorer than those for MoO_2. Scanning the $S^o_{298}[Cr_2O_3]$ column indicates one bad and three (the last three listings) terribly bad errors in ΔG^o_f in the experimental temperature range. Fischer's (81) results have a fair ΔG^o_f in his temperature range, but his temperature coefficient is quite bad. Mazandarany and Pehlke (82) produced very good results. The serious errors in ΔG^o_f are easier to explain than the errors in temperature coefficient. Worrell (45) has pointed out that the poor results of Tretjakow (85) and of Fitterer (86) are due to their use of a $ZrO_2 \cdot CaO$ electrolyte in combination with the Cr, Cr_2O_3 electrode. Schmeltzer's (84) results now join this group for the same reason. The oxygen activity of the Cr, Cr_2O_3 couple is below the lower boundary of the electrolytic domain of $ZrO_2 \cdot CaO$ estimated by Patterson (51), which implies this electrode-electrolyte combination results in too small an emf which does not correspond to the cell reaction. Probably Smeltzer and Fitterer were following the example of Fruehan, Martonik and Turkdogan (87) who successfully employed Cr, Cr_2O_3 as a reference electrode and $ZrO_2 \cdot CaO$ as an electrolyte in an electrochemical sensor to determine the oxygen content of liquid steel at 1600° C. Oxygen contents as small as those corresponding to the oxygen activity of Cr, Cr_2O_3, and even slightly smaller, were successfully measured. On the other hand, Jacob and Alcock (7) clearly

Table 8. Evaluation of $\Delta G^{o}_{f,T}[Cr_2O_3]$ as determined by several workers using oxide electrolyte cells.

Workers	ΔG^{o}_{f} = A+B(cal) Temperature range	$\Delta H^{o}_{f,298}$ (kcal/mole)	Drift (cal/k)	$S^{o}_{298}[Cr_2O_3]$ (cal/k-mole)
JANAF Tables		-271.2±2.0		19.40±.3
Mazandarany & Pehlke *82)	-266600+59.78T 1150-1450K	-270.43	-.6	18.81
Suzuki & Sambongi(83)	-261600+57.06T 973-1823K	-269.27	-3.5	17.85
Janke & Fischer (81)	-257400+55.53T 1823-1998K	-269.77	-5.6	18.64
Smeltzer & Davies (84)	-263350+59.15T 1150-1400K	-267.97	-1.2	16.90
Tretjakow & Schmalzried (85)	-258600+55.2T 1200-1500K	-268.61	-5.2	17.32
Pugliese & Fitterer (86)	-271253+66.20T 1073-1450K	-266.99	5.8	16.12

showed that $ZrO_2 \cdot CaO$ used with an Fe, $FeCr_2O_4$, Cr_2O_3 electrode yielded too small an emf, at least up to 1400° C. An emf of proper magnitude was obtained by using $ThO_2 \cdot Y_2O_3$. At 1400° C, the oxygen activity of Fe, $FeCr_2O_4$, Cr_2O_3 is two orders of magnitude higher than that of Cr, Cr_2O_3. Thus there appears to be a conflict over just how low an oxygen activity $ZrO_2 \cdot CaO$ can withstand and still maintain essentially ionic conductivity. This is too hasty a decision, however; other factors which lead to emf's which are too small must be examined. One purpose of the remaining sections is to identify them. Nonetheless, apparently the Cr, $Cr_2O_3 | ZrO_2 \cdot CaO$ combination is not useful in the cells and temperature ranges employed in Table 8. The first three listings which are better than the last three, in Table 8 are studies which used

Very few measurements on identical, binary alloy systems using oxide-electrolyte cells have been made. Where two different sets of workers have obtained results on the same system, substantial disagreement occurs about half the time. The Fe-Pt system was investigated by Sundaresen (88) and by Alcock and Kubik (89). Alcock showed his results to be in fair agreement with an equilibration study. Both sets of workers ran identical cells, but Sundaresen's emf's are quite different from Alcocks in the Pt-rich half of the phase diagram. Alcock also pointed out that Sundaresen failed to take account of the variation of the thermodynamics of wüstite with its non-stoichiometry and the change of the oxide phase which exists in equilibrium with Fe-Pt alloys from wüstite to magnetite at higher Pt

compositions; his calculated activities are thus also quite different from Alcock's. The Nb-Co system has been investigated by Barbi (90) and Drobyshev and Rezukhina (91). Barbi found by careful equilibration and x-ray experiments that the oxide phase in equilibrium with the two-phase Co-$NbCo_3$ alloy was NbO_2, while Rezukhina found NbO in equilibrium with Co-$NbCo_3$ and $NbCo_3$-$NbCo_2$ two-phase alloys. Comparison of Worrell's results for the oxygen activity of NbO-NbO_2 (52) with Rezukhina's own emf's indicates that NbO_2, not NbO, must be the stable phase. Both Barbi and Rezukhina ran identical cells, but the emf's they obtained differ by 30 mV. Obviously, their calculated activities disagree, but no possibility exists to judge which are better from their work alone. The Cr-Ni system has been investigated by Davies and Smeltzer (84) and Pugliese and Fitterer (86). At 1300K, their determined Cr activities agree at the boundaries of the solid miscibility gap, but Fitterer's Cr activities are about 60% of Smeltzer's in the Ni primary solution. A new pitfall has arisen in the first two examples: Poor understanding of the thermodynamics of phase relationships does not allow one, especially in the case of alloy-oxide systems, to properly interpret one's own data. Rezukhina and Proshina (92) investigated the W-Co system, but their results for $\Delta G_f^o[WCo_3]$ cannot be right because they failed to account for the substantial solubility of W in Co and the change in composition with temperature of this primary solution boundary as discussed in III-C. No indication that these factors were considered is given in the investigation of the Mo-Co system, either (77).

Nearly all the workers considered in this section were not aware that they had experimental problems. Chatterji and Smith (93), who used a ZrO_2·CaO electrolyte to determine the Gibbs energy of formation of Bi_2O_3, Sb_2O_3, and TeO_2, carefully analyzed their data with methods similar to those used in Tables 7 and 8. They knew they had experimental problems because comparison of their extrapolated data to low temperature thermal data showed large differences; but still after noting their existence, they could not understand the source of these differences. The difference between the electrochemical data of Rosenqvist and Haugom (94) on the Gibbs energy of formation of SO_2 and the well-established thermal and spectroscopic data (63) prompted these authors to suggest the replacement of these data with theirs, however.

At this point, the necessity to be able to identify and eliminate errors in cell measurements should be clear; there is plenty of room for improvement in the literature. There is no intent to analyze in detail the papers presented in this section; rather a conceptual framework is to be erected from which the causes for error and the methods for their elimination may be deduced from fundamentals.

B. The Nature of an Oxide-Electrolyte Cell

B.1. Identification of Processes Caused by the Contact of Cell Components with One Another

To build a framework to aid the the correction of errors requires first the formation of a physical picture of an oxide-electrolyte cell. To do so, the cell components are assembled conceptually, one by one. As this is done, the processes occurring and the entities which participate in them are identified.

Consider first the electrolyte, for example, $ZrO_2 \cdot CaO$. How does it respond to the various and changing oxygen activities which arise during actual cell operation? The electrolyte is a three-component oxide; the phase rule requires the setting of two composition variables and the temperature in order to uniquely determine its state. The ratio of Zr^{4+} to Ca^{2+} is fixed by the electrolyte powder mixing process and their diffusion coefficients (44) which are several orders of magnitude smaller than that of O^{2-}; any current is carried by oxide anions when the electrolyte is in the cell. The remaining composition variable is the oxygen to metal ratio which must respond to changing temperature and changing oxygen activity. Therefore, generally, equilibration of an oxide-electrolyte with various oxygen activities is accomplished via a real, physical change of its oxygen content. All oxides have ranges of nonstoichiometry associated with ranges of oxygen activity at given temperatures (95); electrolytes are no exception even though such ranges are necessarily quite small. P. Kofstad (95) has estimated that x in

ZrO_{2-x} is 4×10^{-6} at 1200° C and 10^{-14} atm of O_2. This is at the bottom of the electrolytic domain for $ZrO_2 \cdot CaO$.

How is the required transport of oxygen into or out of the bulk of the oxide-electrolyte brought about? What species participate in the transport process? The defect chemistry and transport properties of $ZrO_2 \cdot CaO$ have been studied extensively (95, and the reviews listed in III-A). The dissolution of CaO into ZrO_2 creates one mole of oxide ion vacancies per mole of CaO added. The lattice gains or loses oxygen according to the equilibrium

$$\frac{1}{2} O_2(g) + 2e^- = O^{2-}(s) \quad \text{or} \quad \frac{1}{2} O_2(g) = O^{2-}(s) + 2h^+ \qquad (8)$$

where e^- is an excess electron and h^+ is an electron hole. Oxide ion vacancies are created or consumed by these reactions. The electronic defects will be identified with chemical species. The possibility of doing so arises from the very small amount of overlap of orbitals on adjacent ions in an ionic solid like $ZrO_2 \cdot CaO$. The resulting "bands" are narrow. The reductive removal of oxygen leaves vacancies on the oxygen lattice and excess electrons. Each electron would be closely associated with a Zr^{4+} and would be the equivalent of a Zr^{3+} cation. The highest level in the valence band would be O^{2-} (96); and, an electron hole would be an O^-. From the chemical viewpoint, then,

$$\frac{1}{2} O_2(g) + 2Zr^{3+}(s) = O^{2-}(s) + 2Zr^{4+}(s) \quad \text{removal of electrons}$$

or (9)

$$\frac{1}{2} O_2(g) + O^{2-}(s) = 2O^-(s). \quad \text{formation of holes}$$

At higher oxygen activities when the Zr^{3+} ions are all used up, oxygen must create holes, O^- ions, to enter the lattice. The emf experiments are carried out at lower oxygen activites, which is the sole concern from now on, so excess electrons are the predominate electronic defect; and Zr^{3+} ions may be oxidized to increase lattice oxygen content. As implied by the species considered in reactions (8) and (9), oxygen atoms or molecules do not diffuse into or out of the oxide lattice. Instead, there is an ambipolar diffusion (43, Chapter 22) of oxide ions and electronic defects. Several studies of the oxygen permeability of $ZrO_2 \cdot CaO$ have demonstrated this mechanism (97, 98). Thus, at lower oxygen activities, oxygen may enter or leave the lattice only by the diffusion of oxide ions and electrons (hopping from Zr^{4+} to Zr^{4+}) in opposite directions. Note that since simultaneous diffusion of both species is required, the $ZrO_2 \cdot CaO$ electrolyte is able to equilibrate with various oxygen activities precisely because it <u>does possess</u> a small but finite electronic conductivity.

Now consider the electrodes which are metal-metal oxide compacts for example, Fe,FeO and Ni,NiO. Upon annealing them, chemical equilibrium is established by transport of metal and oxygen across phase boundaries; but, an electrochemical equilibrium is also set up as soon as the two phases are brought into contact. This latter equilibrium results from contact electrification, a process occurring when two different metals or a metal and a semiconductor are brought into contact at some point on their surfaces. A useful history dealing with the experimental facts which established the existence of contact electrification between

metals has been written by L. Fisher and R. Varney (99). R. Parson's essay on the "Equilibrium Properties of Electrified Interphases" (100) and a book written by E. Spenke (101) discuss related concepts and definitions of terms associated with this phenomenon. For a most thorough understanding of terms used in the following discussion, and of the discussion itself, these three references shouls be consulted. Many other references which dealt with the same topics were of no use in cell analysis.

Contact electrification results from processes which equalize the electrochemical potential of electrons, η_e, (or the Fermi level) in metals and semiconductors when they are brought into thermal equilibrium. In general, the electrochemical potential of any species is defined as

$$\eta_i = \mu_i + z_i FV \tag{10}$$

where μ_i is the chemical potential of species "i" and z_i is its charge, sign included. The electrostatic potential inside the phase (inner potential) is represented by V. Using Fe, FeO as an example, the equilibrium criterion for electrons is

$$\eta_e(Fe) = \eta_e(FeO)$$

or

$$\mu_e(Fe) - FV(Fe) = \mu_e(FeO) - FV(FeO). \tag{11}$$

Spenke remarks, essentially, that μ_e of a solid in a defined thermodynamic state is unique to it and cannot be changed to satisfy the equality in Eq. (11) when contact occurs. He states that what happens

instead is the transfer of a small amount of charge from the surface of one phase to the surface of the other thus changing the inner potential, V, in each phase until equality of η_e exists. Equation (11) may be re-written as

$$\mu_e(Fe) - \mu_e(FeO) = F[V(Fe) - V(FeO)] \qquad (12)$$

which shows that because the difference in μ_e is unique to the two phases, the difference in V must also be unique. The inner potential difference which exists in this equilibrium situation is called the Galvani potential difference. See the schematic representation in Figure 8. Of course, the real situation involves a powder compact, so the inner potential jumps up and down throughout, but η_e is constant as shown. The Volta potential difference, which exists between two points just outside of each phase, also called the contact potential or outer potential difference, is not shown because it is a result of, not a cause of, the equilibration processes just discussed. It is important under conditions of current flow, but that is of no concern here. For the same reasons, the bending of the inner potential at the semiconductor surface is not shown or discussed.

Now contact the Fe, FeO electrode and the $ZrO_2 \cdot CaO$ electrolyte at a temperature sufficiently high to allow the necessary transport, at least 600° C in this case. What happens? The $ZrO_2 \cdot CaO$ oxygen content will change by reducing some FeO or oxidizing some Fe until its own oxygen activity is that set by the Fe, FeO equilibrium. Also, two new, unique Galvani potential differences develop between the electrolyte

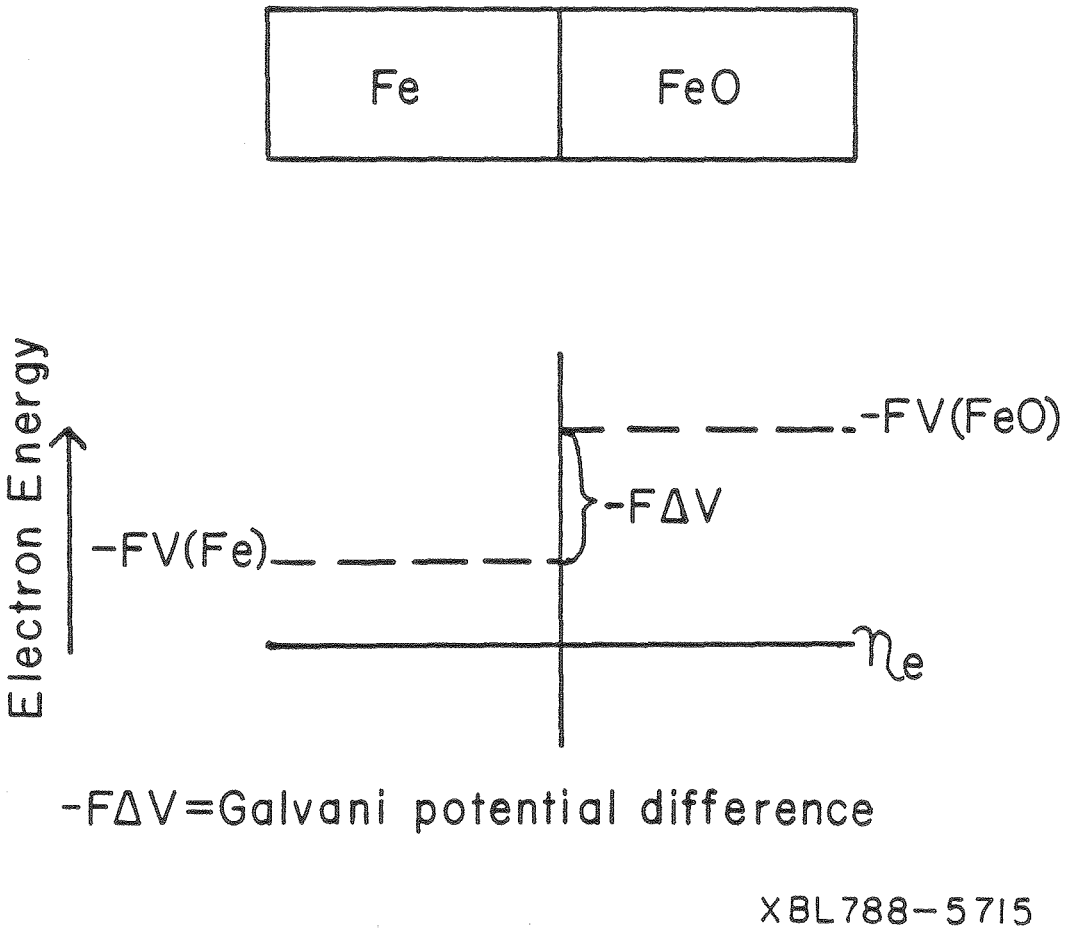

Figure 8. Fe and FeO in contact.

and Fe and between same and FeO because η_e must be constant in all phases.

Now contact the Ni, NiO to the opposite face of the electrolyte. The oxygen activity set by the Ni, NiO electrode is about five orders of magnitude larger than that set by Fe, FeO; therefore, oxygen will transport into the $ZrO_2 \cdot CaO$ from the Ni, NiO. As the oxygen activity at the electrolyte face in contact with Fe, FeO begins to rise, however, this electrode will extract oxygen from the electrolyte. The result is a diffusion of O^{2-} ions from the Ni, NiO electrolyte face to the Fe, FeO electrolyte face where they are consumed and a diffusion of excess electrons in the opposite direction to the Ni, NiO face where they are consumed. The development of this steady-state, ambipolar diffusion creates a physical gradient in oxygen content and, hence, a gradient in the chemical potential of O_2 across the electrolyte. Each differential slice of electrolyte, from one face to the other, can be viewed as being in equilibrium with a particular O_2 activity between the O_2 activities of Fe, FeO and Ni, NiO at the temperature of interest. Choudhury and Patterson (102) have calculated the shape of the μ_{O_2} gradient; it depends on the ionic and electronic conductivities of $ZrO_2 \cdot CaO$. Lastly, Pt discs are contacted to the cell ends, and they adopt the η_e of their electrodes.

The physical picture of an oxide-electrolyte cell is summarized in Figure 9. Studies by Worrell and Iskoe (103) on oxygen exchange between the Cu, $Cu_2O/ZrO_2 \cdot CaO$; Fe,$FeO/ZrO_2 \cdot CaO$; and Ni, $NiO/ZrO_2 \cdot CaO$ electrode-electrolyte interfaces indicate that the major portion of exchange occurs between the metal and the electrolyte as shown. In each electrode,

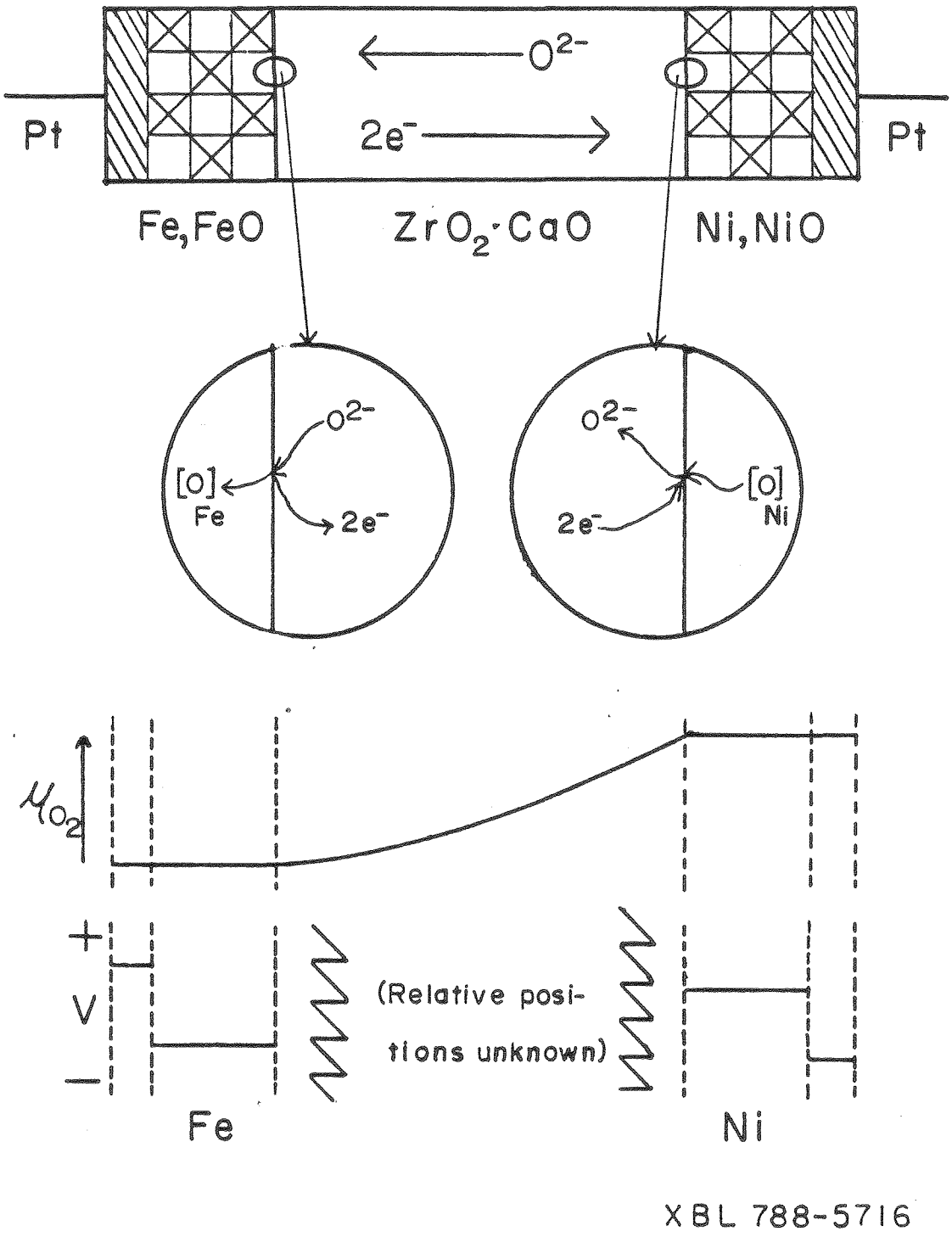

Figure 9. Model for an oxide-electrolyte cell.

μ_{O_2} is constant, but it varies across the electrolyte, the qualitative form of this variation being taken from Patterson. Assuming local equilibrium in the electrolyte, from reaction (8)

$$\mu_{O_2} + 2\,\mu_e = \mu_{O^{2-}} \,. \tag{13}$$

There would be no variation in V in a locality so electrochemical potentials need not be used. In general, as the value of μ_{O_2} changes from values corresponding to superstoichiometric oxygen compositions to those which correspond to substoichiometric ones, the concentration of O^{2-} vacancies in the $ZrO_2 \cdot CaO$ changes from slightly smaller to slightly larger than that established by the CaO. All throughout such changes, μ_e and $\mu_{O^{2-}}$ are not independently variable because electroneutrality is maintained. Oxide ions which have left the lattice in Figure 9 have left behind their electrons; therefore, μ_{O_2} completely determines both μ_e and $\mu_{O^{2-}}$ all the way across the electrolyte. In the electrodes, μ_{O_2} is shown as being constant because it has been assumed that the oxygen transport across the electrolyte is quite small so that only negligible concentration gradients of dissolved oxygen develop in the Fe and Ni particles in contact with the electrolyte. Taking all this into account, the electrodes set μ_{O_2} in the electrolyte at each face which sets μ_e of each electrolyte face which sets the Galvani potential differences between each face and the phases that contact them. The inner potential of selected phases is schematically illustrated in Figure 9, but no statement can be made at present concerning the inner potential of the electrolyte. The relative positions of the left and right half of the

illustration are unknown. From the present level of sophistication of this treatment, neither the value nor even the actual existence of the cell emf may be predicted. The ignorance of the electrolyte inner potential results in the same statement for η_e in the electrolyte; each electrode and Pt contact has a constant η_e though.

B.2. Quantification of the Value and Identification of the Source of the Cell EMF.

The next task is not merely to ascertain the value of the cell emf (it could simply be measured) but rather to identify the processes which create the cell emf and to decide what value it should take in terms of physical parameters which describe such processes. This information will supply the means to judge whether or not the measured emf corresponds to the cell reaction of interest, i.e., whether or not it is the right emf. In this regard, the classical thermodynamic analysis of a cell (61) which results in the statement $\Delta G = -nFE$ does not answer all the required questions. Besides assuming reversible cell operation, this analysis also assumes that the cell reaction is already precisely defined and that it occurs solely by elections flowing in the external circuit. From this point of view then, the ultimate goal is to determine what processes define or change the cell reaction, how the cell reaction might proceed via an inappropriate pathway, and how all this influences the emf.

Great care was taken in the last section to clearly explain that an oxide-electrolyte cell involves a phase of variable composition, the electrolyte itself. Furthermore, mobile species, oxide ions and electrons, transport through the electrolyte continuously. From a chemist's point of view, characterizing the emf of oxide-electrolyte cells requires in principle the same approach that is applied to liquid junction potentials. In fact, there is an apt analogy between an oxide-electrolyte cell and Planck's problem of constrained diffusion through a porous plug (104) which he solved in 1890. An inert porous plug is placed in a tube and two electrolyte solutions, which may contain the same species at different concentrations, bath each side of the plug. A liquid junction potential develops across the plug as a steady-state concentration gradient through the plug is established. The bathing eliminates concentration gradients at the plug faces. This situation may be compared with that in Figure 9. When such a potential develops in solids, it is referred to by the more general term of diffusion potential (43); and it is this phenomenon which must be confronted, explicitly or implicitly, to obtain the emf equation of an oxide-electrolyte cell.

Two approaches are used to obtain the emf equation, one being thermodynamic and the other essentially kinetic, although thermodynamic quantities are used in the transport equations involved. Detailed derivations are unnecessary here; the intent is to briefly state methods and to offer some useful interpretation. First dealing with the thermodynamic approach, Wagner (105) has derived general equations for the emf of cells containing several phases in sequence, any of which may be of

variable composition. Current is passed through the cell, and Gibbs energy changes caused thereby within the phases are tallied from one end of the cell to the other. In the limit of zero current reversibility is approached. Wagner is then able to equate his expression for -dG/dq to E, the emf measured under these conditions. His result for an oxide-electrolyte cell is

$$E = \frac{1}{4F}\int_{\mu_{O_2}^{L}}^{\mu_{O_2}^{R}} t_{ion}\, d\mu_{O_2} \tag{14}$$

where

$$t_{ion} = \frac{\sigma_{ion}}{\sigma_{ion}+\sigma_e}, \tag{15}$$

the fraction of current carried by ionic species as expressed by the ratio of ionic conductivity to ionic plus electronic (total) conductivity. Equation (14) shows that no contribution to the emf arises from cell parts of constant μ_{O_2}, i.e., the electrodes. This is consistent with η_e being constant in each electrode-Pt contact pair because E measured between the Pt contacts is the difference in η_e between electrodes:

$$E = V^{RPt} - V^{LPt} = \eta_e^{LPt} - \eta_e^{RPt} \tag{16}$$

because μ_e^{Pt} cancels out. The only contribution to E under the normal operating conditions assumed in Figure 9 is the change of η_e across the electrolyte. This result may be directly obtained by explicitly considering the diffusion potential in the electrolyte. The general diffusion

potential equation as derived in Mac Innes (104) served as a model for Wagner's treatment and deals with a single junction. Current is passed so slowly through this junction that the steady state concentration gradients are not disturbed, Gibbs energy changes therein are tallied, and the classical thermodynamic formula is used. Application to an oxide-electrolyte cell yields

$$-\frac{dV}{dx} = \frac{1}{F}\left[\frac{t_{O^{2-}}}{-2}\frac{d\mu_{O^{2-}}}{dx} + \frac{t_e}{-1}\frac{d\mu_e}{dx}\right] \tag{17}$$

which is the electric field in the electrolyte. No electronic holes nor other ionic species are considered in Eq. (17) due to the low oxygen activities of interest and the virtual immobility of other ions compared to O^{2-}. Using Eqs. (10) and (13), Eq. (17) may be reduced to

$$\eta_e^{LE} - \eta_e^{RE} = \frac{1}{4}\int_{LE}^{RE} t_{O^{2-}}\, d\mu_{O_2} \tag{18}$$

which is the equivalent of Eq. (14) with $t_{O^{2-}}$ equal to t_{ion}. The integration is taken between the left and right faces (LE and RE) of the electrolyte. Noting that

$$\eta_e^{LPt} = \eta_e^{LE} \quad \text{and} \quad \eta_e^{RPt} = \eta_e^{RE} \tag{19}$$

clearly shows that measurement of the cell emf between two like metal contacts always gives the difference in η_e across the electrolyte.

The kinetic method based on the use of transport equations results in the same equations. Wagner used this method in his classic work on parabolic oxidation of metals (106) which can be applied to oxide-electrolyte cells because they may be viewed as a well-defined case of parabolic oxidation. Heyne (107) and Planck (104) have also used the kinetic method to derive the emf equation and diffusion potential equation, respectively. Heyne and Wagner develop the transport equations used which are based on Ohm's law and Fick's first law of diffusion. All the currents in the electrolyte are summed and set equal to zero which yields Eq. (17). Planck worked directly with Ficks second law and the assumption of local electroneutrality to obtain Eq. (17).

The relationship between t_{ion} and the diffusion potential across the electrolyte may now be uncovered; it bears directly on the capability of an oxide-electrolyte cell to produce thermodynamic data. Combining Eqs. (18) and (16) and using the definition (from calculus) of the average ionic transport number, $\bar{t}_{ion}$,

$$FE = \eta_e^{LE} - \eta_e^{RE} = \frac{1}{4}\,\bar{t}_{ion}\left(\mu_{O_2}^{RE} - \mu_{O_2}^{LE}\right). \tag{20}$$

If $\bar{t}_{ion}$ is essentially 1 (> .99), Eq. (20) simplifies to

$$E = \frac{RT}{4F}\,\ell n\,\frac{p_{O_2}^{RE}}{p_{O_2}^{LE}}, \tag{21}$$

the Nernst equation. (By manipulating electrode equilibria, Eq. (21) may be obtained from Eq. (4). The cell may then be used to produce data as

outlined in III-C. If $\bar{t}_{ion} < 1$, E shrinks; and a so-called "non-thermodynamic" emf is obtained. To obtain data, the integration in Eq. (14) or (16) could be carried out if t_{ion} is known as a function of μ_{O_2}; but this method is not practical because the increased electronic conductivity (σ_e) increases the rate of open-circuit transport of oxygen across the electrolyte (vide infra) and the electrodes become polarized (42).

Equation (20) demands a reduction of E as $\bar{t}_{ion}$ decreases in value. What physical process brings about the reduction of $\Delta\eta_e$ across the electrolyte? Equation (20) may be transformed using Eq. (10) and Eq. (22),

$$\eta_e = \frac{1}{2}\eta_{O^{2-}} - \frac{1}{4}\mu_{O_2}, \tag{22}$$

which is based on the local equilibrium of reaction (8),

$$\frac{1}{2}O_2(g) + 2e^- = O^{2-}(s), \tag{8}$$

to Eq. (23),

$$\mu^{LE}_{O^{2-}} - \mu^{RE}_{O^{2-}} - 2F(V^{LE}-V^{RE}) = \frac{1}{2}\bar{t}_e\left(\mu^{LE}_{O_2} - \mu^{RE}_{O_2}\right). \tag{23}$$

The quantities refer to those in either electrolyte face; and $\bar{t}_e$, the average electronic transport number, is $1 - \bar{t}_{ion}$. Generally, nonstoichiometric oxides show very small changes of composition over several orders of magnitude change in oxygen pressure (95). As already noted, this compositional change for $ZrO_2 \cdot CaO$ is abnormally small; it minimizes the concentration of electronic current carriers. Thus in $ZrO_2 \cdot CaO$, the relative change of O^{2-} concentration over even 10 orders of magnitude of oxygen pressure is exceeding small; therefore, $\Delta\mu_{O^{2-}}$ in Eq. (23) is close to zero.

The inner potential drop across the electrolyte or diffusion potential, $V^{LE} - V^{RE}$, is then given by the rest of Eq. (23). If both oxygen pressures are chosen to be low enough to cause substantial electronic conductivity via reaction (8) and if the one on the right is much greater, $\bar{t}_e$ will be a sizeable fraction and $V^{LE}-V^{RE}$ will be positive and of considerable magnitude. On the other hand, if $\Delta\mu_{O_2}$ is kept constant but each oxygen pressure is raised, then $\bar{t}_e$ approaches near zero (as long as the pressures are low enough to avoid holes) and so does the diffusion potential. It may be shown that the measured emf (assuming no polarization) plus the diffusion potential is the emf calculated from the Nernst equation, if both oxygen pressures are known.

Figure 10 shows the inner potentials of the Pt contacts and wires and the electrolyte. The electrodes are not shown. Since η_e is constant through them, they may be viewed as the means to set the μ_{O_2} in the electrolyte face which then determines the Galvani potential difference between the electrolyte face and the Pt. A useful cell with $\bar{t}_{ion} > .99$ is shown to have no electrostatic potential drop across the electrolyte while a useless cell shows a diffusion potential, $V^{LE} - V^{RE} > 0$. Clearly, the diffusion potential is responsible for the shrinking E, not any change in the Galvani potentials because they do not depend on the relative magnitudes of ionic and electronic conductivity which are represented by $\bar{t}_{ion}$.

Considering the driving forces for open circuit oxygen transport, a cell with $\bar{t}_{ion} > .99$ with virtually no diffusion potential has a $\Delta\eta_e$ which arises from the oxygen composition gradient across the electrolyte. Electrons are driven by a concentration gradient from left to right.

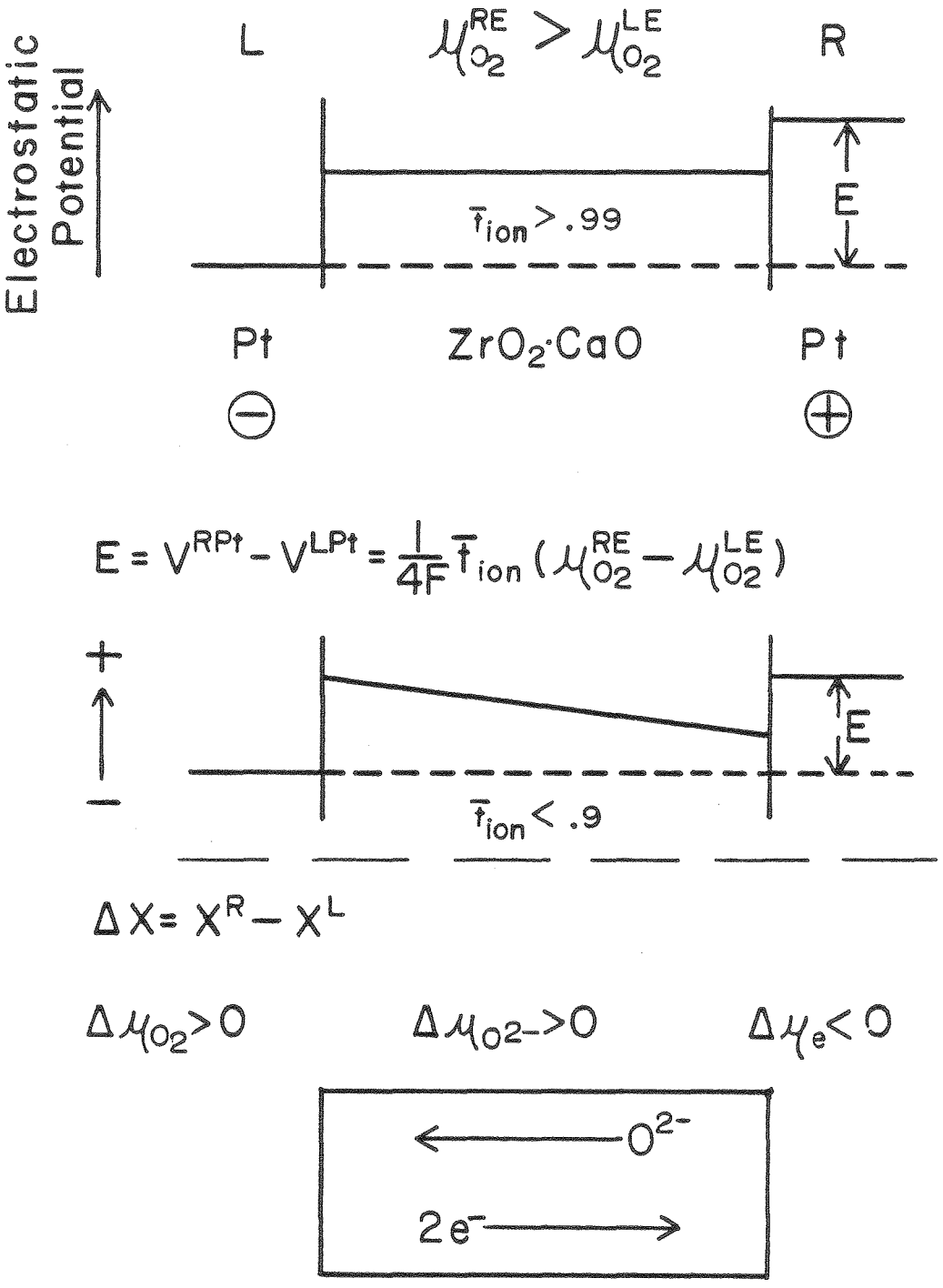

XBL788-5717

Figure 10. Effect of the diffusion potential on the emf and open-circuit transport.

A slight concentration gradient drives O^{2-} ions from right to left. At lower $\bar{t}_{ion}$ when the concentration of electrons increases, the diffusion potential retards the electronic current somewhat and boosts the O^{2-} current. Thus, open-circuit oxygen transport increases with decreasing $\bar{t}_{ion}$.

There are a few important facts to be emphasized in summary. Measurement of the cell emf yields directly the $\Delta\eta_e$ across the electrolyte. If the electrode successfully set the right μ_{O_2} in each electrolyte face, then the emf corresponds to the cell reaction of interest. If some difference could exist between the μ_{O_2} of an electrode and the μ_{O_2} of its electrolyte face, the effect would be a change in cell reaction and a corresponding change in emf. Lastly, it is the open-circuit transport of oxygen through the electrolyte which allows the cell reaction to proceed via a pathway other than the external circuit and makes the classical thermodynamic formula inapplicable unless the transport is small and $\bar{t}_{ion} > .99$.

C. Errors and Problems Associated with the Improper Functioning of the Cell

Worrell (45) has already briefly discussed the topics covered in this section. His points are further explained and illustrated here.

C.1. Effects of Electronic Conductivity in the Electrolyte

The existence of electronic conductivity in the electrolyte can reduce the cell emf to a value which is smaller than the proper one; this reduction can occur through two different aspects of the same process. As discussed in the last section, open-circuit transport of oxygen across the

electrolyte creates a diffusion potential therein which subtracts from the emf predicted by the Nernst equation. If $\bar{t}_{ion} > .99$, this effect will be negligible; at lower oxygen activities, however, σ_e increases while σ_{ion} remains constant. Ultimately, $\bar{t}_{ion}$ drops below .99; emf measurements then yield erroneous thermodynamic data because calculations are made using the Nernst equation. Open-circuit, oxygen transport can also create nonequilibrium, oxygen concentration gradients in the electrodes at each electrode-electrolyte interface. Such gradients may occur with or without the nucleation of a phase at the interface. Deviation of μ_{O_2} from the equilibrium values at the electrode surfaces in contact with the electrolyte requires a corresponding change of oxygen content in each electrolyte surface. An increase occurs on the side of low μ_{O_2}, and a decrease occurs on the side of high μ_{O_2} due to the direction of oxygen transport. Thus, $\Delta\mu_{O_2}$ across the electrolyte itself is decreased relative to equilibrium conditions in the electrodes. Since the measured emf reflects directly the difference in oxygen content of the electrolyte faces (see Eq. (20)), it will be reduced to below its appropriate value according to the magnitude of the concentration gradients caused by open-circuit transport. If the rate of oxygen transport is small relative to the rate of electrode diffusion processes which deliver the oxygen to and disperse it from the electrolyte, then concentration gradients in the electrodes and the accompanying concentration overpotential will be negligible. On the other hand, if electrode diffusion processes are relatively slow, the measured emf will be significantly in error.

Having characterized these problems on an abstract level, consideration will now be given to the specific factors upon which they depend.

The magnitude of the diffusion potential depends solely on $\bar{t}_{ion}$. Once a particular oxide-electrolyte and its dopant concentration have been chosen, the value of the electronic conductivity determines the value of $\bar{t}_{ion}$ at the temperature and electrode oxygen activities of interest. The magnitude of open-circuit, oxygen transport is determined by several factors. It is given by (43,107)

$$J(\text{amp/cm}^2) = \frac{1}{4F} \frac{\sigma_{O^{2-}} \sigma_e}{\sigma_{O^{2-}} + \sigma_e} \frac{d\mu_{O_2}}{dx} \approx \frac{1}{4F} \sigma_e \frac{d\mu_{O_2}}{dx} \qquad (24)$$

where J is the O^{2-} current density. An approximation of $\sigma_{ion} > 10\sigma_e$ has been used in Eq. (24). It shows that the size of J in this case is limited by σ_e for a given μ_{O_2} gradient. Integration of Eq. (24) yields an expression for J which is applicable to cells involving lower oxygen activities with $\bar{t}_{ion} > .9$ and σ_e due to excess electrons,

$$J = \sigma_e \ (x=0) \frac{RT}{FL} [1 - \exp(-F E_{Ner}/RT)] . \qquad (25)$$

The direction of the x axis is taken from the anodic side to the cathodic side of the electrolyte. Application of Eq. (25) requires knowledge of σ_e of the electrolyte at the oxygen activity of the anode and of the emf, E_{Ner}, given by the Nernst equation for the particular $\Delta\mu_{O_2}$ across the electrolyte. The various factors that determine the size of J can now be identified. The open-circuit current is inversely proportional to L, the thickness of the electrolyte. Its magnitude approaches a maximum with increasing E_{Ner} for a given anodic σ_e if $E_{Ner} > 0$. (This is because an increase of E_{Ner} is brought about by increasing the cathodic oxygen activity. The electronic conductivity near the cathode

shrinks due to a loss of carriers, but $\Delta\mu_{O_2}$ increases. These competing effects cause J to approach a maximum as long as E_{Ner} is not increased too much so that hole formation is avoided.)

A significant diffusion potential can be avoided by confining the oxygen activities encountered in a working cell to those within the electrolytic domain of the particular electrolyte in use. Patterson (51) conservatively estimated the breadth of the electrolytic domain for $ZrO_2 \cdot CaO$ and $ThO_2 \cdot Y_2O_3$. He presents them graphically in terms of log P_{O_2} vs. 1/T plots and states that the boundaries of the domains are given by the condition $\sigma_{ion} = 100\ \sigma_e$, or $t_{ion} = .99$. Outside the boundaries, $\sigma_{ion} < 100\ \sigma_e$ due to increased electronic conductivity from holes or excess electrons. There are two reasons, however, why the exact positions of these boundaries are not definable generally. First, Worrell has noted that the impurity content of an electrolyte strongly influences the position of a domain boundary. Variable valence transition metal impurities are especially harmful because they can donate or accept electrons according to the ambient oxygen activity. The effect of Fe could be represented by

$$2\ Fe^{3+} + O^{2-} = \frac{1}{2}\ O_2(g) + 2\ Fe^{2+}. \qquad (26)$$

The Fe^{3+} cation will be reduced more readily than the Zr^{4+} cation, thus creating an abnormally large number of excess electrons. These additional carriers increase the electronic conductivity causing the low oxygen activity domain boundary to shift to higher oxygen activities. The same sort of effect would arise from impurities of Mn, Cr, Ti, etc. The domain boundary rises as the level of contamination increases until, if

there is sufficient contamination, the electrolyte is transformed to a mixed, rather than an ionic, conductor. For ZrO_2•CaO (15 m/o CaO), 1% electronic conductivity would be introduced by 130 mole ppm of an impurity which creates one excess electron per ion, assuming that the mobilities of such electrons are 100 times that of O^{2-} ions. The effect of relatively high Si contamination (.1 - .5 w/o, which often occurs in electrolyte starting materials) on bulk electronic conductivity is difficult to predict, if there is any at all. A study by Beekmans and Heyne (108) indicates that the most important effect of Si contamination is the formation of a second, intergranular phase of low ionic transport number. One of their ZrO_2•CaO samples which contained .2 w/o Si (and comparable levels of other nontransition metal contaminants) showed a considerable amount of a second phase and strong dependence of impedance on frequency. No such phase could be seen in the electrolytes used in this work; they contained .1 w/o Si and performed well in tests mentioned in III-G. The second reason which does not allow exact location of a domain boundary lies in Patterson's use of actual cell measurements to help define it. If successful cell work has been done at a certain p_{O_2} and T, then that point lies within the electrolytic domain of the particular electrolyte used. The work could not have been good if $\bar{t}_{ion} < .99$; if so, the point would have to lie outside the electrolytic domain according to Patterson's definition. If the measured emf is too small, however, and none of the sources of error yet to be covered exist, then the point does not necessarily lie outside the domain. The cell's deviation from its proper emf may be caused by concentration overpotentials due to open-

circuit transport even if $\bar{t}_{ion} \geq .99$. Excepting the electronic conductivity, this criterion does not control the factors involved in open-circuit transport and electrode polarization. In the case of the low oxygen activity boundary for $ZrO_2 \cdot CaO$, for example, points derived from direct measurements of electrolyte conductivity (109) suggest a lower position for the boundary than do those based on actual cell measurements.

The infuence of concentration overpotentials on the cell emf can be used to offer a reasonable interpretation of the seeming disagreement between the work of Turkdogan (87) and Alcock (7) briefly raised in IV-A concerning the "exact location" of the lower domain boundary for $ZrO_2 \cdot CaO$. Worrell's work on oxygen transfer kinetics between a $ZrO_2 \cdot CaO$ electrolyte and various metal-metal oxide electrodes (103) can be used to roughly estimate the magnitude of overpotential present in Alcock's cell,

$$Fe, FeCr_2O_4, \ Cr_2O_3 | ZrO_2 \cdot CaO | Fe, FeO, \qquad V$$

which seems to suggest that $t_{ion} < .99$ for the oxygen activities of the left electrode from 800 to at least 1400° C. Worrell measured the steady-state overpotential in symmetric cells with small currents flowing through them. He was able to show that the overpotential was due to oxygen concentration gradients in the metal particles in contact with the electrolyte and was able to relate the size of the overpotential to the solubility-diffusivity product of oxygen in the metal. The open-circuit current of Cell V at 1000° C was calculated using Eq. (25). The measured emf of Cell V was used in the calculation, which then assumes that $\bar{t}_{ion} \geq .99$. The electronic conductivity information required to perform the calculation was taken from Rapp's dc polarization work (109). The

company literature of Alcock's source of electrolytes in tube form shows that L, the thickness, was only 1/16 inch. The value of J obtained (7.6 $\mu A/cm^2$) was then used in Worrell's treatment, and a value of 4 mV was calculated for the overpotential. Alcock found that Cell V had an emf which was 3 to 5 mV too low; therefore, electrode polarization could quite possibly account for the error Alcock found in Cell V. This result is consistent with the successful performance of Turkdogan's oxygen sensor at oxygen activities which lie even deeper in the electrolytic domain. He proved beyond doubt that errors resulting from a significant diffusion potential in the $ZrO_2 \cdot CaO$ electrolyte were absent. His choice of reference electrode and cell construction minimizes concentration overpotentials: (1) As the oxygen content of the steel decreases, the cell emf decreases and reduces the open-circuit current driving force. (2) An electrolyte 3 to 4 mm thick was used. (3) The solubility-diffusivity product of oxygen in liquid steel is huge and works to minimize concentration gradients from open-circuit transport in the melt.

Turkdogan's success poses a question concerning the failure of the Cr, $Cr_2O_3 | ZrO_2 \cdot CaO$ combination to yield good values of $\Delta G_f^0[Cr_2O_3]$ for the workers in Table 8 who used it: Why did it not work for them? Perhaps the oxygen activity of the Cr, Cr_2O_3 electrode is outside the electrolytic domain of $ZrO_2 \cdot CaO$ at the lower temperatures they used. Rapp's polarization and ac conductivity measurements imply a t_{ion} of .992 at 1000° C and the Cr, Cr_2O_3 oxygen activity, however. This is a borderline case, but it cannot account for the large errors found in Table 8. The problem may then be suggested to have been contamination of the electrolytes by transition metal impurities, thus lowering $\bar{t}_{ion}$.

Instead of resting on that suggestion, however, the question of whether electrode polarization alone can account for the errors will be examined. Consider Smeltzer's cell,

$$Cr, Cr_2O_3 \mid ZrO_2 \cdot CaO \mid Fe, FeO. \qquad VI$$

Assume, according to Rapp's results, that $\bar{t}_{ion} > .99$ for Cell VI. In the same manner as for Cell V, J was calculated to be $55 \mu A/cm^2$ at 1000° C. (Smeltzer also used an electrolyte tube of 1/16" wall thickness.) The nature of Worrell's treatment of overpotentials and the cell set-up itself allows only a very rough estimate of the overpotential expected from this value of J. Near equality of the solubility-diffusivity products of O in Fe and Cr must be assumed because the diffusivity of O in Cr is unknown. Examination of lattice constants, the solubility and diffusivity of O in Cr (111) indicates that this assumption is good to within an order of magnitude. The overpotential is then estimated to be in the range of about 10 to about 30 mV. Cell VI has an emf at 1000°C which is 11 mV too small, so the error has been accounted for without assuming any significant diffusion potential. Fitterer used the same type of electrolyte tube (L = 1/16") as did Smeltzer but replaced the Fe, FeO electrode with air; his results are appropriately worse due to increased electrode polarization. In Fitterer's cell, $\bar{t}_{ion}$ is larger than in Smeltzer's cell. If a diffusion potential were assumed to contribute to their errors, this would necessarily imply even larger overpotentials than those just estimated. There is no reason to disagree with Rapp's finding which places Cr, Cr_2O_3 on the borderline of the electrolytic domain at 1000° C, however, at this point, σ_e has increased enough to make the Cr, Cr_2O_3|

$ZrO_2 \cdot CaO$ combination generally susceptible to polarization except in the most controlled of circumstances. The best course of action is to avoid it. Pehlke's success is due to his use of the $ThO_2 \cdot Y_2O_3$ electrolyte which, Rapp's work shows, has a σ_e at the Cr, Cr_2O_3 oxygen activity of at least 100 times smaller than that of $ZrO_2 \cdot CaO$. Overpotentials are avoided if the other factors are not pushed to extremes.

What can be learned from this long discussion regarding emf work on Lewis-acid-base alloys? Hartung (112) has attempted to measure the solubility-diffusivity product of oxygen in platinium; he has also summarized the attempts of other workers. This quantity measured at an oxygen pressure of .21 atm and 1000° C is no more than one-hundredth that of oxygen saturated Fe at the same temperature. At the low oxygen activities encountered in cell work, it is surely much smaller. In electrodes involving primary solutions of noble metals, the relatively small conductivities of such alloys for oxygen would be expected to make the electrodes susceptible to polarization due to significant oxygen concentration gradients in the alloy particles in contact with the electrolyte. This situation might be avoided if the oxide in the electrode were capable of exchanging oxygen with the electrolyte at least as fast as the metal; to allow this possibility, the oxide must establish good physical contact with the electrolyte which requires the exacting polishing techniques explained in the appendix. Rather than hoping for help from the oxide, a simple test can be performed which will indicate the presence of a concentration overpotential if it exists or prove its absence. The test must be performed on the cell in question only after $\bar{t}_{ion}$ has been proved to be > .99 by perhaps running a commonly successful cell (III or

IV, for example), after the flow rate test has been passed (see III-F) and after any side-reactions have been eliminated. The cell emf may continuously decay, in which case the transport processes causing the overpotential are unable to reach steady-state; and, the problem will be obvious. Much less obvious is the steady-state overpotential, which has been the particular concern here. A cell with such a problem will pass the "polarization test" (steady-state will merely be reestablished after current flows in the external circuit) and also the stability test. If the electrolyte thickness, is varied, however, a steady-state overpotential will manifest itself through a cell emf which decreases as L decreases. If no overpotential exists, one can probably be created if the electrolyte is made thin enough; the approach of the cell emf to a constant value may then be observed when L is increased. The electrolyte thickness can be varied by grinding the tablet down to a wafter. A factor of eight in thickness should be obtainable (1/4 to 1/32 inch) and sufficient to cause an observable effect on the emf unless the size of open-circuit current is quite harmlessly small. If an overpotential of either type is discovered, the factors involved in its creation which have been identified, explained, and illustrated in this discussion must be manipulated to eliminate it.

C.2. Effect of Reactive Impurities in the Flowing Inert Atmosphere

The measured, cell emf directly indicates the difference in oxygen content in the electrolyte faces. If the oxygen content in a face is changed by reaction with gas phase molecules, this deviation from the oxygen content set by the electrode equilibrium will be reflected by the

measured emf. In such a case, the oxygen activity in the affected face no longer corresponds to the cell reaction; it gives rise to what is referred to as a "mixed potential." A plausible mechanism for the creation of a mixed potential can be presented.

Reactive impurities will always be present at some level of concentration in the cell atmosphere. They may arise from poor gettering of the intert gas supply; for example, H_2 and CO are harder for Zr and Ta to getter than H_2O and CO_2. Degassing of H_2O from the alumina containment tube, much of which will be reduced to H_2 by the internal Ta getter, is also a source of impurities. Very small leaks which occur after the gettering furnaces in the gas line contribute oxygen; the Ta getter in the containment tube cannot be expected to be 100% efficient, although its presence is designed to minimize the effects of oxgygen leaks. Significant pressures of gaseous species may be produced by the electrodes themselves, either by equilibrium between electrode phases which result in gaseous products or by reaction of contaminants in the electrode phases with same to yield gaseous products. The latter case produces products which may obviously be regarded as gas phase impurities, but the former does also because the products produced in this case cannot achieve equilibrium pressures or distributions in the experimental configuration; they will be a foreign influence to both electrolyte faces.

Consider the effect of reactive, gaseous impurities in the context of the cell model which has been developed. If H_2 or CO, for example, impinges on an electrolyte face, each is liable to abstract an oxygen atom; the opposite tendency would hold for H_2O or CO_2. Under constant flow rate conditions, a net addition or subtraction of oxygen from

each face might occur save for the influence of the contacting electrode which senses the oncoming deviation of oxygen content away from what it prescribes. The electrode adds oxygen to or substracts it from the electrolyte face to counteract the change effected by the reactive impurities. In a metal-metal oxide electrode, the rate at which oxygen could be transported in the appropriate direction would again be proportional to the metal's oxygen solubility-diffusivity product. The oxygen activity in the electrolyte face is, finally, the result of a competition in reaction rates between the solid state and the gaseous state. Any of three situations can result: (1) Gas phase interference can be so small relative to the rate of solid-state, oxygen transport that the oxygen activity in the electrolyte face does not noticeably deviate from that required by the contacting electrode. (2) Solid-state and gaseous transport processes can have comparable rates that result in an electrolyte-face, oxygen activity which is significantly different from what the electrode requires but is constant due to a steady state. (3) Gas phase processes may overwhelm solid-state ones. The cell may have an emf which changes continuously over several hours, as if the electrode processes can never "catch up." If gas phase processes are large enough, they can swamp out the influence of the electrode; the electrolyte-face oxygen activity would then be nearly completely controlled by the gas phase.

The basis for a flow rate test is now clear. Changing the flow rate changes the rate of gas-electrolyte reactions. If such reactions do not significantly contribute to fixing the electrolyte-face, oxygen activity, then negligible effect (< 1 mV change) on the cell emf will follow a flow rate change.

All these general statements concerning the nature of a mixed potential and hence emf flow rate dependence were drawn from specific experiences in the course of experimental work; they now serve as illustrations. Cell VII,

$$\text{Ir, } TaIr_3, \text{ } Ta_2O_5 \mid ZrO_2 \cdot CaO \mid \text{Fe, FeO,} \qquad \text{VII}$$

was run several times. The emf never stabilized and continuously decayed most of the time. Changing the flow rate from 25 to 125 cc/min produced vast (> 10 mV) decreases in the cell emf. The internal Ta getter was always oxidized near the cell tablets, but no where else. During one run, gas flow was stopped by completely isolating the cell volume; the emf increased linearily with time, seemingly forever (> 8 hr.). After the run, soot was found in the cooler sections of the cell tube and the Ta getter had developed a golden color (TaC) near its top end. The electrodes were analyzed for carbon; the Fe, FeO electrode was found to contain 250 ppm/w C. Analysis of the Fe then being used as starting material for the electrode showed .1 to .2 w/o C. Assuming that all the C in the electrode was dissolved in the Fe, one can use the results of Chipman (113) on the activity of C in Fe to calculate the equilibrium pressures of CO and CO_2. They are .6 and .2 atm, respectively, at 1000° C; thus, the contaminated Fe, FeO electrode would certainly be expected to generate CO as fast as it could. Little CO_2 production would be expected under the nonequilibrium conditions of a flowing atmosphere. Cell VII was, then, its own source of reactive gas phase impurities. Only the electrolyte face in contact with the alloy-oxide electrode was being affected, however. Cell III, the iron-nickel cell, was tested using the C contaminated Fe,FeO electrodes,

and its emf was quite flow rate independent and quite correct. The large solubility-diffusivity products of oxygen in Fe and Ni were able to support sufficiently fast transport of oxygen in the solid state to overcome gas phase interference. This is an example of situation (1), noted above. The noble metal rich alloy in the alloy-oxide electrode of Cell VII would not be expected to support such fast solid-state transport of oxygen; the Fe,FeO side of Cell VII remained unaffected as it was in Cell III, but the opposite side could not compete with the gas phase. In fact, when Cell VII was isolated and the CO pressure was allowed to build up, the alloy-oxide side of the electrolyte was reduced continuously as if its contacting electrode were not even there. Thus, Cell VII illustrates both aspects of situation (3).

The steps taken to obtain a flow rate independent cell containing an alloy-oxide electrode offered further understanding of the response of a cell to gas phase interference. Cell VIII,

$$\text{Ta, } Ta_2O_5 \;|ThO_2{\cdot}Y_2O_3|\; \text{Ir, } TaIr_3, Ta_2O_5, \qquad \text{VIII}$$

was run to make sure a flow rate independent emf was possible for a cell involving a Ta-Ir electrode. When the flow rate was changed from 30 to 180 cc/min, the emf of Cell VIII decayed 2 mV, and then began to increase again. It did not restabilize to within 1 mV of its original value owing to other problems created by the contamination of the $ThO_2{\cdot}Y_2O_3$ electrolyte; but the fact that it was able to reverse the decay of its emf, something which Cell VII was never able to do, was taken as a strong indication that Ta-Ir electrodes could function in a flow rate independent fashion in the cell atmosphere which had been purified by the technique explained in III-D.

Another aspect of the slow oxygen transport kinetics of the alloy-oxide electrode was visible in Cell VIII: Its response to a flow rate change was much more sluggish than that of Cell IV, which involved an Nb,NbO electrode in place of the alloy-oxide electrode. Both Ta and Nb have large oxygen solubility-diffusivity products (each has a larger oxygen solubility than Fe and a bcc lattice); this is consistent with its small deviation (.1 - .2 mV) from its original emf at any time during a flow rate test. Cell VIII and flow rate independent cells run later on which also involved an alloy-oxide electrode always suffered a 2 mV drop in emf when the flow was increased. They only sluggishly reversed the decay and, in the case of flow rate independent cells, finally stabilized to within 1 mV of their original value. (See IV-C-C.3 for an example.)

An attempt was made to "clean up" Cell VIII by using an Fe,FeO electrode which had been made from Fe which contained 170 ppm/w C. Further purification of the electrode was expected through vaporization of CO during annealing. After the cell had been run, examination of the Ta getter showed that CO/CO_2 impurities had indeed been reduced. The oxygen transport from the Fe, FeO to the getter which had been mediated by this couple was substantially attenuated. During the run, this cell produced an emf that was stable to within .7 mV for 48 hr. When the flow rate was changed from 36 to 280 cc/min, the emf dropped 14 mV but restabilized in a day's time. When the flow rate was reduced to 150 cc/min, the emf increased 5 mV over a half day's time and stabilized. The cell then produced an emf which was stable to within 1 mV for a half day. The flow rate was then reduced back to 36 cc/min and the cell had nearly recovered its original emf in a half day when the run was

stopped. Atmospheric contamination had been reduced, but not to the negligible level. This cell is a clear case of situation (2), a cell with a steady-state, mixed potential; it produced a stable potential for each of the three flow rates. Here again is an example of a stable cell which is a bad cell. Only a flow rate test could have demonstrated this for sure. Other tests need not fail; the cell may even have yielded a linear emf vs T relationship.

The slight decay of Cell III with time, noted in III-G, was also due to a mixed potential. The NiO in the Ni, NiO electrode tends to dissociate when this cell is run for 2-3 days at about 925° C. The ring of metal sponge left behind about the outer circumference of the electrode tends to deform and expose part of the electrolyte face, a situation which favors gas phase interference. With the assistance of D. Davis, Cell III was run again using Fe (MRC) which contained only 18 ppm/w C as electrode starting material. Even with marked NiO dissociation, no decay was observed for 4 days at 925° C.

D. Davis also ran two cells which clarified an aspect of the mechanism for gas phase interference suggested at the beginning of this discussion:

$$Nb_2O_{4.8}, NbO_2 \,|ZrO_2 \cdot CaO|\, Fe,FeO \qquad IX$$

$$Nb_2O_{4.8}, NbO_2 \,|ThO_2 \cdot Y_2O_3|\, Fe,FeO. \qquad X$$

The MRC Fe was used in these cells. Cell IX was quite flow rate dependent; it had an emf which decreased more than 10 mV under a flow change of 30 to 230 cc/min. When flow rate tested, Cell X decayed 1.5 mV and then stabilized. The point to be taken lies in the large difference in

flow rate dependence between the two cells. They have identical electrodes but different electrolytes. If the major cause of gas phase interference were gaseous impurities reacting with the electrode particles at the electrode-electrolyte interface, one would expect no difference in flow rate dependence between the two cells because the oxygen activity in the electrolyte face would simply follow that of the affected particles. While it may be argued that the difference could lie in differing rates of oxygen transport across the interface, a simpler and more likely explanation is that the gaseous impurities are reacting directly with the electrolyte face. Thus one can be lead to speculate why one electrolyte could be more reactive to gas phase impurities than the other. Evidently, in Cells IX and X the Fe was still not clean enough. An equilibrium CO pressure of 10^{-2} atm would still exist at 1000°C if the Fe contained 5 ppm/w C. Further purification would result if the Fe,FeO electrode were recrushed and reannealed a couple times. The slow oxygen transport kinetics of the $Nb_2O_{4.8}$, NbO_2 electrode is not surprising.

What general rules can be made to aid the emf worker in avoiding or eliminating gas phase interference? Of course, the quality of the tank inert gas and the purification technique ought to be followed because they were successful. The need for the low temperature, hydrogen gettering furnace is arguable but certainly not the dehydration of the source gas to pick up most of the hydrogen as water. Good polishing techniques should be used to maximize physical contact between electrode and electrolyte and to minimize interfacial porosity. Thus, solid-state transport processes are favored, and gas phase transport is hindered. All this does little good if the electrodes produce significant pressures of gaseous species.

Electrodes with poor oxygen transport capability will be greatly affected. Powdered metals with low levels of nonmetal contaminants should be used for electrode synthesis. If the impurities produced do not bother the electrode that produced them, another solution would be to place the electrodes in separate compartments with different gas flows. An electrolyte pressed against the polished end of an alumina tube with one electrode inside the tube and the other outside should render sufficient separation. Electrolyte tubes generally ought not to be used to achieve separation because their thin walls may cause concentration overpotentials in the electrodes. Tubes of $ThO_2 \cdot Y_2O_3$ would offer less risk in this regard than those of $ZrO_2 \cdot CaO$, but they are very expensive.

The problem of carbon contamination is a general one for a single compartment system. For example, a Mo, MoO_2 electrode, which was substituted for Fe, FeO in Cell VII, was also found to be contaminated with carbon; it caused the same problems as the electrode it replaced. Also Meschter (64) found he could not get the Cr, Cr_2O_3 electrode to work with a $ThO_2 \cdot Y_2O_3$ electrolyte and a Pt rich alloy-oxide electrode. There is no reason to expect the Cr, Cr_2O_3 electrode to experience problems in the solid state in this situation. It worked well for Mazandarany and Pehlke (82), but they separated their electrode compartments. No gas phase species of the Cr-O system occur at significant pressures at 1000° C, so chrome carbon contamination was probably the stumbling block. Although the carbon content of the Ta used to make Ta, Ta_2O_5 electrodes was 35 ppm/w, no problems have been encountered in their use. The carbon would be very tightly bound if it equilibrated with the metal in comparison to the other electrodes, and perhaps this is the reason. Care should be exercised in their use, and in the use of Nb, NbO electrodes. Some of Cell VIII's behavior was puzzling.

C.3. Effect of Side Reactions at the Electrode-Electrolyte Interface

The highest temperature at which a cell can be operated is usually determined by the occurrence of a side reaction. For example, Worrell (52) found that the combination $Fe,FeO|ThO_2 \cdot Y_2O_3$ was unsuitable for emf work even at moderate temperatures (900-1000°C) due to the formation of $YFeO_3$ at the interface. Meschter (64) found no side reaction in the combination NbO_2, $Nb_2O_{4.8}|ThO_2 \cdot Y_2O_3$ at temperatures below 1025°C, but at higher temperatures a dense blue product layer formed on the electrolyte. The layer's X-ray pattern resembled that of $YNbO_4$. Both these situations resulted in cell emfs which were several millivolts too low. The errors grew worse with time at higher temperatures; they were not eliminated when the electrolyte was used again after grinding the product layer away (58). The following discussion tells how such side reaction products lower the emf, and it identifies the parameters which determine the magnitude of the effect. The information gained is used to analyze a side reaction encountered in this work. Results of the analysis assist the suggestion of ways to eliminate the side reaction.

The model for a cell which has formed a product layer through side reaction is illustrated in Figure 11. The layer is represented as a ternary oxide composed of the electrolyte additive and the electrode oxide. The μ_{O_2} of each electrode is constant, but μ_{O_2} changes across the electrolyte and across the ternary oxide. This gradient in oxygen composition is set up by open-circuit transport of oxygen from the right electrode to the left electrode, across both intermediate phases. The interface between these two phases acts as neither source nor sink for ions or electrons;

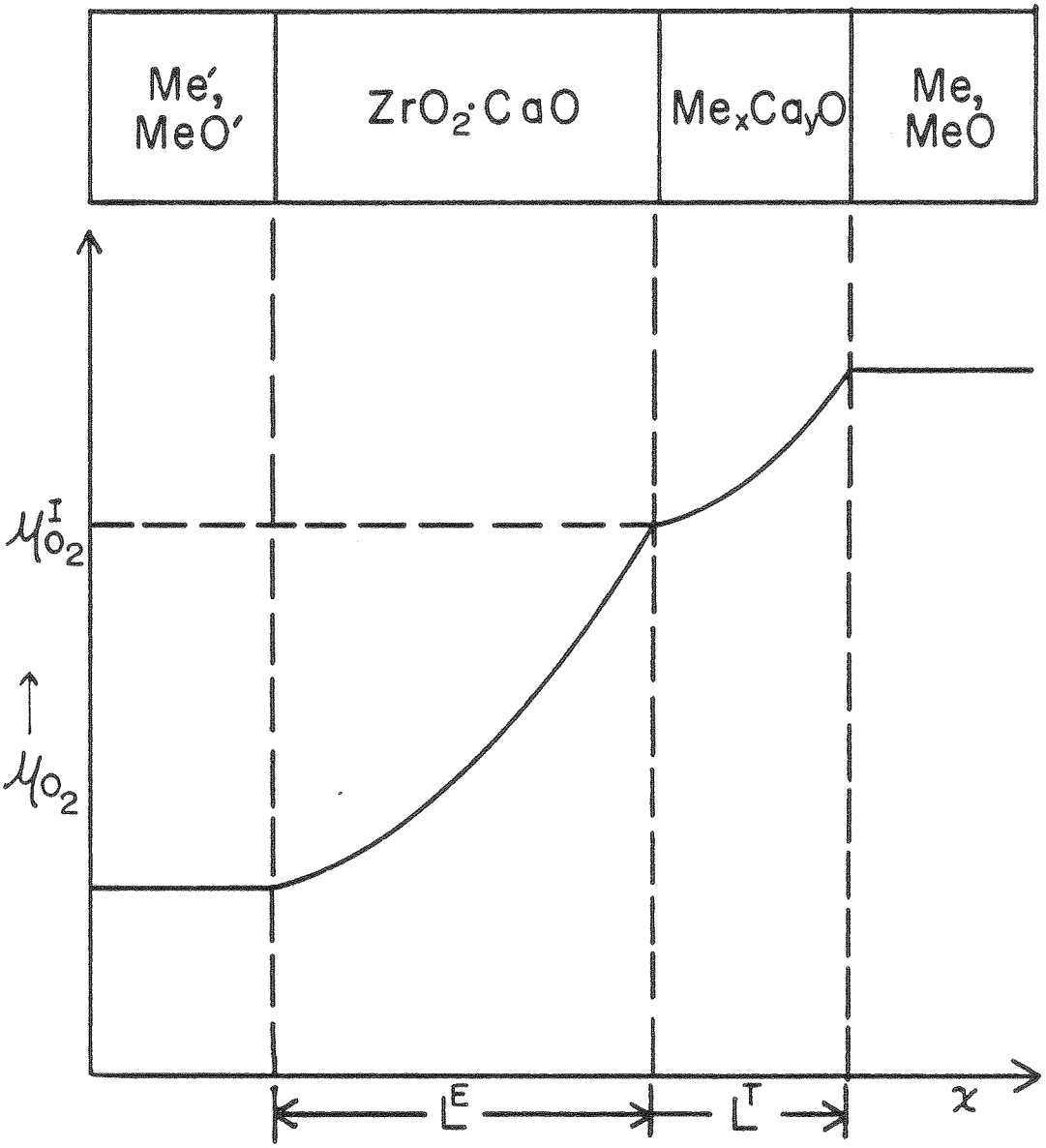

Figure 11. Model for a cell with a product layer from side reaction.

the open-circuit current is then the same in each. The variation of μ_{O_2} across each phase and its value at the interface, $\mu_{O_2}^I$, are both determined by the transport properties of the two phases.

The model is essentially a cell with two solid electrolytes; the steady-state conditions in such a cell and its emf have been interpreted by Wagner (114). His ideas have been applied to a cell with two oxide-electrolytes by Shores and Rapp (115). They also briefly note that their treatment can be applied to the present situation. What will the measured emf be? It is the change of n_e across the electrolyte and the ternary oxide; therefore, Wagner's integral, Eq.(14), must be taken across the cell parts where μ_{O_2} and hence n_e varies:

$$E = \frac{1}{4F}\int_{I}^{RT} t_{ion}^{T}\, d\mu_{O_2} + \frac{1}{4F}\int_{LE}^{I} t_{ion}^{E}\, d\mu_{O_2}, \qquad (27)$$

where T and E refer to the ternary oxide and electrolyte, respectively; and RT refers to the right side of the ternary oxide, etc. If the ternary oxide is an ionic conductor like the electrolyte, the measured emf experiences no decay. If not, the contribution of each integral in Eq.(27) is determined by the change of μ_{O_2} across the ternary oxide, i.e., the value of $\mu_{O_2}^I$. The farther removed $\mu_{O_2}^I$ is from $\mu_{O_2}^{RT}$, the more the emf diminishes. If they are quite close, the effect on the emf is negligible because the first integral is nearly zero. The calculation of $\mu_{O_2}^I$ is done by solving the integral equation,

$$\frac{1}{L^T}\int_{I}^{RT} \sigma_{tot}^{T}\, t_{ion}^{T}\, t_{e}^{T}\, d\mu_{O_2} = \frac{1}{L^E}\int_{LE}^{I} \sigma_{tot}^{E}\, t_{ion}^{E}\, t_{e}^{E}\, d\mu_{O_2}, \qquad (28)$$

which is obtained by equating the expressions for the open-circuit current

of the electrolyte and the ternary oxide. The three factors that determine $\mu_{O_2}^{I}$ are thickness, total conductivity, and the distribution of conductivity between ionic and electronic, $t_{ion}t_e$. If two factors are imagined to be identical in each phase, while the third is varied, a qualitative statement can be made concerning the effect on the value of $\mu_{O_2}^{I}$. The thicker phase experiences the larger change in μ_{O_2}. The phase of larger conductivity experiences the lesser change as does the phase of larger $t_{ion}t_e$. Calculations have been done which illustrate these points (102).

A unique type of side reaction occurred in the last cell run in this work:

$$NbO_2, Nb_2O_{4.8} | ZrO_2 \cdot CaO | Ir, TaIr_3, Ta_2O_5 \qquad \text{XI}$$

Cell XI was first run at 1000°C continuously. After 24 hr. at temperature, it attained an emf which was stable to within .3 mV for 26 hr. (The emf was not found to be reproducible in later runs; its value was about 13 to 16 mV.) A flow rate test was conducted after this period of stability by changing the He flow from 25 to 240 cc/min. After an initial decrease, the emf asymptotically approached a value .6 mV higher than the original emf. Thus, this cell was genuinely flow-rate independent; the test took 12 hr. The cell leads were short-circuited for 30 sec. The 8 mV drop in emf was nearly recovered in 10 min. After 80 hr. at temperature, the emf began to steadily decay. The emf dropped 3 mV in four more days. Another run was set up, and no testing was performed. Data were taken as quickly as possible from 1000° down to 900°C; this required five days. Points from 950 to 1000°C were linear with T, but those from 900° to 950°C were 2 to 5 mV below the line extrapolated from higher temperatures. After the point at 900°C had been taken, the temperature was increased back up

to 980°C; the emf was 2.4 mV lower than its first measurement. Cell XI could not produce data. Why?

Both interfaces of the first run of Cell XI were examined microscopically. Only a very slight, very light roughening was found in one spot on the electrolyte face which had contacted the niobium oxides electrode. The alloy-oxide electrode-electrolyte interface had been disturbed. Most of the polished flats of the metal particles near the center of the electrode were partly or completely covered with a brown granular film on the order of 1μ thick. The Ta_2O_5 in the electrode was not disturbed. The electrolyte had a light orange,mottled appearance closer to its circumference; but near its center, disruptions which were darker, more reddish in color were seen. They appeared to be small sites of growing phases. Similar phenomena, although less pronounced, had been observed in the relatively short runs of Cell VII; an orange color, but no disruptions, had appeared on the electrolyte. Further studies were made with an electron microprobe and a scanning electron microscope. A micrograph of the electrolyte surface appears in Figure 12. The disruptions noted above are seen to be raised islands of a new phase about 2μ thick lying on the electrolyte surface. The porosity of the electrolyte is still visible, especially in the bare areas. The islands were rich in Ta and also contained much more Ca than an unreacted $ZrO_2 \cdot CaO$ standard. The Zr signal from an island and the standard were about the same, so most or all of an island's Zr signal probably came from the electron beam penetrating the electrolyte below it. Some Ir was also found in the islands. Bare

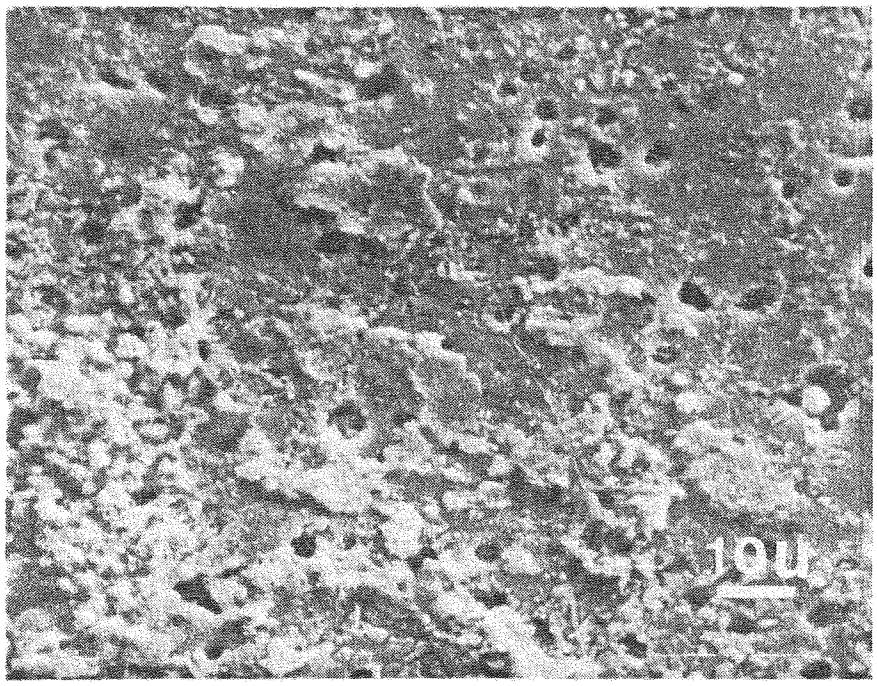

XBB 7711-11492

Figure 12. Product layer islands on the electrolyte surface.

areas near an island had reduced CaO concentrations. Bare areas surrounded by islands had CaO concentrations of 4-5 m/o.

Direct reaction between the Ir,$TaIr_3$ alloy and the ZrO_2·CaO electrolyte had been ruled out earlier. Powders of each had been mixed and heated for 25 hr. at 1410°C and 72 hr. at 1000°C. After each heating, metallographic examination showed no reaction. This implied that oxygen supplied by the electrolyte during cell operation was oxidizing the alloy surface. (In Cell VII runs oxide film occurred on the alloy but no islands formed on the electrolyte; therefore, these islands do not cause the oxide film on the alloy.) Oxygen was being supplied to the alloy faster than it could transport it away. This forced nucleation of Ta_2O_5, or possibly one of the lower metastable oxides which occur during Ta oxidation. To test this conclusion, a ZrO_2·CaO electrolyte was "pumped down" by heating it in contact with a Ta,Ta_2O_5 electrode. This electrolyte was then heated (2 days,1000°C) in contact with an Ir,$TaIr_3$,Ta_2O_5 electrode. No oxide film formed because oxygen had to be transported in the opposite direction compared to that in the cell. Approximate calculations show that sufficient oxygen could be supplied from the pore phase and the nonstoichiometry range of a new, unused electrolyte to produce the amount of oxide film observed. Running Cell XI with a used electrolyte provided no improvement, however, because the cell always experienced a negative emf for 15 hr. during its initial equilibration. During this time when the emf increased from about -90 to 0 mV, the open-circuit transport in Cell XI carried oxygen to the alloy-oxide electrode. Calculations again show that sufficient oxygen was made available to form the film on the alloy.

The source of the calcium tantalate islands is now clear. The oxide film was in intimate contact with the electrolyte. During extended runs it reacted with the CaO therein. Much of the area close to the circumference of the electrolyte face was denied contact with the electrode when the film or islands formed near the center. This is the situation depicted in Figure 11, the separation of the electrode from the electrolyte by a product layer.

The theory presented at the beginning of this discussion can be used to account for the behavior of Cell XI. It demonstrates that a layer which is only about one-thousandth the thickness of the electrolyte can indeed cause a large reduction in the emf. The cell passes through two stages. The product layer is first assumed to be Ta_2O_5, and then a calcium tantalate. Stroud and Tripp (116) have measured σ_{tot} and t_{ion} for Ta_2O_5 as functions of T and oxygen activity. The emf of Cell XI is taken to be 10 mV at 975°C, which appears close to reality. The oxygen activities of each electrode are so close that the quantities inside the integrals in Eq.(28) can be brought outside. The oxygen activity between the electrolyte and product layer is calculated and used to predict the cell emf. The value of σ_{tot} for Ta_2O_5 at this temperature and narrow range of oxygen activity is .047 ohm^{-1}-cm^{-1}, about three times that of $ZrO_2 \cdot CaO$, while $t_{ion} \sim .01$. Data for the electrolyte was taken from Rapp (109), $t_{ion} = .9997$ and $\sigma_{tot} = .016$. No change in oxygen activity occurs across a layer of Ta_2O_5 which is 1μ thick. The same result is obtained for a Ta_2O_5 layer 100 μ thick with a $t_{ion} = .001$. Even in this, the most extreme situation conceivable, a layer of Ta_2O_5 between the electrode and the

electrolyte can not affect the cell emf through Eq.(27). After the Ta_2O_5 had been precipitated on the alloy and before its reaction with CaO, the emf of Cell XI was therefore close to the right emf. A few millivolts change in the cell emf would result from the change in composition of the alloy beneath the precipitated Ta_2O_5.

The 2-3 mV decay of Cell XI which occurred as it aged can be attributed to the formation of the calcium tantalate. No calculations dealing with this phase can be done because the exact composition and transport properties of this substance are unknown, but there is probably another layer besides this one. The CaO concentrations observed in the bare spots in Figure 12 were low enough to destabilize the $ZrO_2 \cdot CaO$ cubic phase. Just behind the calcium tantalate islands, the much larger depletion of CaO would be expected to precipitate a thin layer of monoclinic ZrO_2. Under the conditions of interest its conductivity is $10^{-5.5}$ $ohm^{-1}cm^{-1}$ (95) and $t_{ion} \sim .01$ (117). Assuming no change in oxygen activity across the calcium tantalate layer, a 2-3 μ layer of ZrO_2 will reduce the cell emf by 1-2 mV. These results are sensitive to the value of t_{ion} taken for the electrolyte; for example, if t_{ion} is taken to be somewhat smaller, .995, the predicted emf reductions nearly triple. The calcium tantalate is probably not an ionic conductor; and, if its transport properties are poorer than those of Ta_2O_5, it would also serve to reduce the cell emf. These calculations are approximate, but they show that a thin layer is injurious to the cell emf if its transport properties are poor. A thick layer, such as the one encountered by Meschter, is not necessarily required to ruin a cell. A thick layer does make it impossible to reuse an electrolyte.

So much dopant is drawn out by the product layer that a significant volume of the remaining, unreacted portion of the electrolyte is a mixed conductor.

These steps can be taken to eliminate the peculiar side reaction of Cell XI. A ThO_2-based electrolyte must be substituted for $ZrO_2 \cdot CaO$. The rate of open-circuit, oxygen transport will be reduced. This and the smaller nonstoichiometry range of a ThO_2-based electrolyte will reduce the rate and amount of oxygen transported across the electrode-electrolyte interfaces. Precipitation of Ta_2O_5 on the alloy can thus be stopped. Test cells involving the combination $Ir,TaIr_3,Ta_2O_5|ThO_2 \cdot Y_2O_3$ never showed any disturbance at the interface. The electrolyte dopant and reference electrode to be used must be chosen to minimize the possibility of side reaction. If the niobium oxides electrode is to be used, CaO, which is used at low concentrations, could be the dopant. Worrell substituted CaO for Y_2O_3 and avoided side reaction with the Fe,FeO electrode. The mechanism for the product layer formation appears to involve the diffusion of the dopant out of the electrolyte to meet and react with the electrode oxide. Use of dopants such as BaO and La_2O_3 with large cations would slow this process. If the Cr,Cr_2O_3 electrode could be made to function, it would have less tendency to side react than the niobium oxides electrode.

C.4. One Aspect of the Thermoelectric Effect in an Oxide-Electrolyte Cell

Wagner has discussed (118) the thermoelectric power of cells containing ionic compounds involving mixed conduction. The procedures used to eliminate error due to a thermoelectric voltage are not difficult and

have been discussed in III-G. One additional problem which can lead to a thermoelectric voltage was saved for discussion here.

Consider the effect of interdiffusion between an electrode and its metal disc used to establish electrical contact. The electrode oxide does not usually participate; the reaction takes place between the disc and the metal in the eleectrode. If the electrode is thick, the composition of the metal at the electrode-electrolyte interface is not changed. This means n_e in the electrode and in its contacting disc is also not changed. The compositional gradients that result in the reaction region cannot change n_e. A thermoelectric component in the measured emf may result from this reaction, however. The simple rules used to decide whether a thermoelectric voltage will exist in a specific situation or not have been presented by Moffat (119). The composition of the lead wire spot-welded to the metal disc must be unchanged between the external connections and the constant temperature zone in the furnace. If some of the electrode metal diffuses through the disc and into the lead wire where the temperature begins to fall, a thermoelectric voltage will result. If the reaction stays within the constant temperature zone, the cell emf remains unaffected. If the electrode is to be used several times, its reacted volume which is usually very small can be ground away to prevent the contamination from spreading too far into the electrode. The composition of the contacting metal disc is electrically irrelevant because the disc lies within the constant temperature zone. Contaminated ends of lead wires ought to be cut off.

C.5. On the Equilibration of Alloy-Oxide Electrodes

Brief comments were made at the end of III-F and III-E.4 on the problem of attaining and testing for equilibrium in the alloy-oxide electrodes. Their very slow approach to equilibrium was noted and useful testing procedures were outlined. Further explaination of these procedures and the rationale behind them is presented here. Some added precautions which ought to be taken are also discussed.

The alloys used to make the electrodes must, of course, be at equilibrium before they are crushed and mixed with the oxide. For a single-phase alloy, the equilibrium requirement is simply a homogeneous composition in the whole alloy button. For a two-phase alloy, equilibrium is attained when the proper partitioning of elements between the phases has taken place throughout the button. Equilibration of Lewis-acid-base alloys at high (>1600°C) temperature usually presents no problems. The single-phase alloy may be homogenized at any high temperature in the phase field. The compositions of the phases in the two-phase alloy may have significant dependence on annealing temperature. Therefore after annealing a two-phase alloy button at high temperature, it should be annealed at a lower temperature which will bring the phase compositions closer to those associated with the temperatures of the emf experiment. This should most certainly be done if compositional dependence on temperature is large. The second annealing temperature of 1500°C used in this work was chosen because Grant demonstrated that phase precipitation could occur with 2 days of annealing at this temperature. This indicates that significant

transport occurs at 1500°C in a reasonable amount of time. The composition of the Ir,$TaIr_3$ alloy varies little with temperature, so the necessity of a second annealing is arguable. It will be important for the σ, α_1 alloy to be encountered in future work (see Figure 6). Whether diffusion processes are fast enough for the two-phase alloy to achieve equilibrium compositions at cell temperatures or not is the subject of a test explained below.

Sometimes, when an alloy button is melted on a water-cooled hearth, coring occurs. Small inhomogeneities result from crystallization taking place from the cooled bottom of the button to its top. The shapes of the solidus and liquidus curves control the existence of coring. It is expected in the tantalum-rich part of the Ta-Ir system. During his investigation of the Ta-Rh phase diagram, Grant (120) noted coring in arc-melted buttons which had Ta compositions greater than 75 a/o. He was able to eliminate it with an initial annealing at 1600°C for 72 hr and an additional annealing at 1970°C for 36 hr. If problems with alloy equilibration are suspected, the buttons can be cross-sectioned and electron microprobed.

When the oxide is mixed with the crushed alloy and annealed, the metal/oxygen ratio of the oxide must change in order for equilibration to occur. Ultimately, the chemical potential of the metal in the alloy and in the oxide must be equal. Consider the case of an electrode involving a single alloy phase, for example, Ir,Ta_2O_5. White Ta_2O_5 will have a Ta activity which is too small to be in equilibrium with, for example, a 2 a/o Ta alloy. Transport of Ta from the alloy to the oxide would play the major

role in increasing the oxide's metal/oxygen ratio. Some vaporization of oxygen from the oxide would occur at first; but as the activity of oxygen therein decreased, the vaporization rate would too. Also, only an exceedingly small amount of oxygen would dissolve in the Ir at the equilibrium oxygen activity of the electrode; however, some must. Assuming that equilibration takes place by transport of Ta, would the amount of Ta extracted from the Ir phase significantly change its composition? If so, emf measurements using this electrode would be of very limited use. The metal/oxygen ratio of Ta_2O_5 has been determined as a function of T and oxygen activity (116). Fortunately, it varies only little. If a P_{O_2} of 10^{-16} atm at 1023°C is assumed for the electrode at equilibrium, the resulting composition of the Ir phase may be calculated using this information. The Ta concentration would still be 2.00 a/o, taking into account the relative proportions of phases given in III-E.4. No significant change in alloy composition results from equibration with white Ta_2O_5 for the electrode which would be most susceptible to such a change.

An unaltered alloy composition at equilibrium means little if this state is not attained or if one has no proof that it has been attained. The Ir phase particles are quite large, about 100 μ in diameter. A particle surface suffers depletion of Ta as the oxide extracts it. The oxygen activity of an Ir phase particle would follow that of the oxide as the oxide's metal/oxygen ratio changed. A concentration gradient of Ta is set up which drives Ta on a long trip toward the surface. While all this happens, the electrode oxygen activity is effectively controlled by

the surface Ta concentration of the Ir phase particles. The Ta gradient in the particle decreases as the metal/oxygen ratio in the oxide increases. If such equibration processes are at work, the electrode oxygen activity will decrease with annealing time. If this is observed when the electrodes are alternately annealed and then used in a cell, transport processes are fast enough at the annealing temperature to ultimately bring the system to equilibrium. If a stable electrode oxygen activity is observed from the start, then either equilibrium was attained in the first anneal or it can never be attained. A completely "frozen" electrode is unlikely, but one that approached equilibrium very slowly may require on the order of 600 hr. of annealing time. In such a case, limits to the oxygen activity could be obtained by using an additional electrode of the same alloy, but made with grey (reduced) Ta_2O_5. This oxide has a metal/oxygen ratio that is initially too large to be in equilibrium with the iridium-rich alloys used so far. The physical situation is the reverse of that described above. Tantalum would transport in the opposite direction and the approach to equilibrium would be manifested by an oxygen activity that slowly increased with annealing time. Limits to the oxygen activity could thus be established. Use of grey Ta_2O_5 in electrodes that reach equilibrium somewhat faster would supply an additional proof of equilibrium, besides the one obtained by alternate annealing and cell running, if they are used in conjunction with those made from white Ta_2O_5. A "white" electrode and "grey" electrode would approach and attain the same oxygen activity from opposite extremes. If identical oxygen activities were found for two such electrodes annealed together just once, this would be proof of equilibrium. Again using the

example of the 2 a/o Ta electrode, the Ir phase composition in a "grey" electrode is estimated to be 2.01 a/o Ta at equilibrium. This change, calculated with the same assumptions made above for a "white" electrode, is not significant.

The arguments made above with regard to equibration between oxide and alloy also apply to a two-phase alloy electrode except that in this case the alloy phase composition is uniquely fixed at a given temperature. The required redistribution of components in the alloy phases due to equilibration with the oxide is quite minute, however. If successful equilibration with the oxide occurred with Ir,Ta_2O_5 electrodes, no problem would be expected with any alloys with richer Ta compositions. Whether the compositions in a two-phase alloy can follow the cell temperature, at least well enough to produce insignificant error in the emf, is another question. The test for equilibrium with respect to this process requires the use of a high (1125°C) and a low (925°C) annealing temperature for electrodes containing two alloy phases. If initial cell equilibration is carried out at 1025°C, the emfs obtained for electrodes of different annealing temperatures should approach one another with annealing time.

Finally, electrode annealing should be done in a good vacuum. The compositions in single-phase alloy electrodes are not unique. Enrichment of the alloy can occur by the reaction

$$Ta_2O_5 = 2Ta(Ir) + \tfrac{5}{2}O_2(g), \qquad (23)$$

if the O_2 is chemically transported away. In vacuum, the reaction proceeds by the electrode dissociation pressure only which results in a negligible

rate. Powdered Ir and Ta_2O_5 did not react when heated in vacuum at 1330°C for 18 hr. The precipitation of $TaIr_3$ in the single-phase alloy electrodes was observed early in this work when electrodes were being annealed in a poorly purified inert atmosphere.

APPENDIX

Electrolyte and Electrode Polishing Techniques

The procedures used to polish the electrolytes were designed to produce the smoothest possible surface on a small scale and to produce the flattest possible surface on a large scale which covered the entire electrolyte face.

The first part of the procedure involved the use of eight-inch-diameter, resinbonded, diamond wheels (3M Diamond Discs) at 170 RPM. Then diamond paste (Buehler Metadi) smeared on scored plexiglass (a technique used by P. Meschter) was used for the final polishing stage. The steps and the lubricant employed in each are listed:

(1) 15 μ diamond wheel, water

(2) 9 μ diamond wheel, water

(3) 6 μ diamond wheel, kerosene

(4) 6 μ diamond paste, ethanol

(5) 1 μ diamond plaste, ethanol

No metallurgical mounts were used, and the polishing in steps (4) and (5) was done by hand. In step (1), a special device was used to mechanically hold the electrolyte tablet so that one face could be ground completely parallel to the other. Kerosene was required in step (3) to prevent hydroplaning. The tablets were finally cleaned ultrasonically in methyl ethyl ketone and then in pharmaceutical ethanol.

The flatness and smoothness of the polished electrolyte surface was examined with a Clevite Surfanalyzer 150. The surface profile was quite smooth and had less than 0.1 μ amplitude variation between pores. The surface profile, taken as a whole, appeared as an arc due to the edge-rounding which is generally associated with polishing procedures based on lapping. Electrolyte surfaces were said to be "1.5 μ out-of-flat," which meant that if a subtending chord was drawn from one extreme end of the surface arc to the other, the maximum distance between the chord and the arc occurred at the tablet center and was 1.5 μ. Electrolyte faces of this smoothness and flatness were consistently produced by the described methods.

Attempts to increase the flatness, such as mounting the tablets in expoxy resin impregnated with alumina and vibration polishing, yielded comparable or often poorer results than those quoted above. Vibration polishing with 0.3 μ alumina dust could not produce as smooth a surface as the above methods, either.

Figure A-1 shows a $ZrO_2 \cdot CaO$ electrolyte surface as used in cell runs. The pores do not appear to be interconnected.

Smoothness and overall flatness were also desired for electrode faces which were to be pressed against the electrolyte. Smoothness was attained by polishing methods which did not rip away the oxide phase from the areas among the metal particles but instead polished both so that their surfaces were even. To attain maximum flatness, the severe edge-rounding encountered when first developing the techniques to attain smoothness had to be avoided. In general, edge-rounding may be substantially reduced by surrounding the specimen to be polished with a material

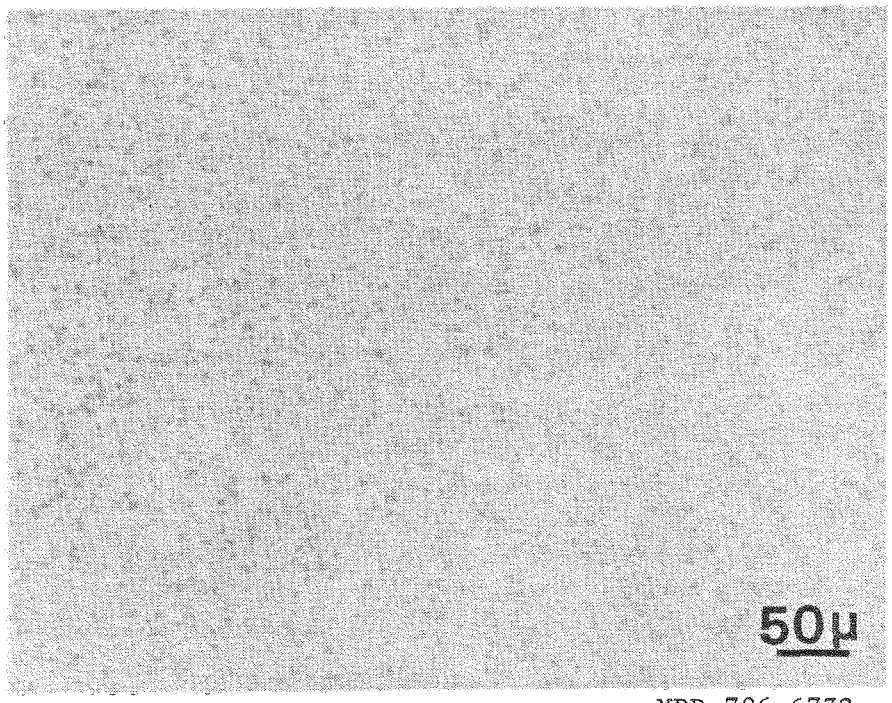

XBB 786-6732

Figure A-1. Polished surface of ZrO_2·GaO electrolyte.

having a hardness similar to the specimen itself. Most of the electrodes polished were therefore placed snugly inside the drilled-out hole of a 1" diameter stainless steel or brass washer, and then both electrode and washer were mounted in epoxy resin (Koldmount, Vernon-Benshoff Co.).

Besides obtaining a tight electrode-electrolyte interface, there is another reason why good polishing techniques were developed for the electrodes: The face of an electrode which has been polished to maximum smoothness also reveals the electrode microstructure at maximum clarity under microscopic examination. Since frequent checking of the electrodes was necessary to look for side-reactions, nucleation or disappearance of phases, or any other sort of physical alteration, metallographic examination proved to be a valuable technique. In fact, X-ray analysis is actually inferior to it for discovering physical changes because such changes must occupy at least a few volume percent of the sample to be exhibited in an X-ray spectrum. Metallographic analysis therefore had the final word for deciding whether new phases had nucleated or not. In order for this technique to be useful in this capacity, polishing had to proceed to the maximum smoothness. Experience showed that a poorly or partially polished surface did not reveal all of its microstructural detail.

The first part of the polishing included abrasive grinding by hand on silicon carbide papers (Buehler Carbimet). Then followed grinding on a 3 μ alumina-impregnated, plastic lap (Pfizer Ultralap). This was done on a wheel at 170 RPM. The final polishing stage involved the use of a powered alumina (Buehler Micropolish), aqueous slurry on felt (Buehler Microcloth) and was also done on a wheel at the same speed. Automatic polishers were unsuitable; the specimens were held by hand. Because some

of the electrodes were porous which made them difficult to dry and because many of the materials of which the electrodes were composed are known to adsorb hydrocarbons, all electrode grinding, polishing, and washing was done under completely aqueous conditions. No hydrocarbon was allowed to contact any of the electrodes. The steps are listed:

(1) wrap electrode in aluminum foil

(2) place inside brass or stainless steel washer and mount in epoxy resin

(3) 240, 320, 400, and 600 grit silicon carbide papers, water

(4) 3 μ alumina lap, water

(5) 1 μ alumina aqueous slurry

(6) 0.3 μ alumina aqueous slurry

In step (1), the foil prevented contact with the mounting material. The hardness of the alloy-oxide electrodes required that they be mounted inside stainless steel washers. The Fe, FeO; Ni, NiO; and Mo, MoO_2 electrodes required no mounting and were polished only on silicon carbide papers, except that the 3 μ alumina lap was used in Mo, MoO_2. These electrodes were ductile and a fairly even surface could be put onto the electrode face with this shortened method, thus allowing the establishment of a good electrode-electrolyte interface. All other electrodes were mounted inside brass washers and were taken through the entire polishing scheme, along with the alloy-oxide electrodes. The 240 grit silicon carbide paper was used to even the surfaces of the washer and the electrode. Care was taken to mount the two surfaces as evenly as possible in the first place to minimize the amount of electrode which had

to be ground away. This was especially important for alloy-oxide electrodes because they had to be used several times. If too much of a stainless steel washer had to be ground away, excessively long (ca. 3 hr.) grinding times resulted. Time could be saved by remounting the electrode correctly. At no time should a motor-driven, abrasive belt be used to even the electrode and washer surfaces. This tore out metal particles from the electrode surface so deeply that holes were still left in it after the polishing scheme was completed. The flushness of the electrode and washer surfaces was checked by touch and a straight edge. Polishing could not proceed until these surfaces were flush. Then 400 passes were made over the length of the 320 grit paper, 600 over the 400 grit, and 800 over the 600 grit. After polishing in the slurries, the washer was prized from the mount; and, the electrode was pushed from a hole in the opposite side. If the electrode became stuck in the mount, heating at 100°C sufficiently softened the epoxy resin to get the electrode out of its mount. Higher temperatures were not used to avoid fumes. The electrode was then placed in the holding device mentioned before, and the unpolished face was ground using 240 grit paper until it was parallel to the polished one. The electrode was cleaned ultrasonically in distilled water with gentle intensity. Strong intensity jarred the oxide phase out of the surface. Drying was done in an oven at 100°C for 6-8 hr.

Peculiar, troublesome polishing properties were encountered except in the case of the three electrodes which were not mounted. All other electrodes had jagged, uneven surfaces through step (4) in the polishing scheme. The oxide was being ripped out and the metal particles themselves were not undergoing polishing. Resinbonded diamond wheels,

diamond paste on canvas, alumina powder slurries on glass, and various other techniques failed to avoid ripping away oxide although some progress was made on polishing the metal. Fortunately, solid success evolved from working with alumina slurries on felt. With the 1 μ slurry, a coherent surface began to develop and oxide appeared. The 0.3 μ slurry fully developed smoothness and surface porosity was nearly eliminated. During all the polishing steps, the surface was microscopically examined. The next step was commenced when no further improvement could be observed.

Surface profiles of the alloy-oxide electrodes were taken. Their surfaces were found to be 1.5 μ out-of-flat. Their smoothness was the same as the electrolyte surfaces, but the pores were deeper. The surface profile of another type of electrode, viz., Ta,Ta_2O_5, indicated that it was 1 μ out-of-flat. Surface profiles also indicated that vibration polishing was detrimental to surface smoothness. Metallographic examination revealed that some of the oxide had been shaken out of the electrode surface. After cells were run, examination of the electrode-electrolyte interface showed that contact had occurred over its whole area, unless a new phase had nucleated at the interface.

Figure A-2 displays a polished NbO_2, $Nb_2O_{4.8}$ electrode surface. The black spots are pores. The dark grey is $Nb_2O_{4.8}$ and the light grey is NbO_2. Figure A-3 displays the polished surface of an α-Ir, $TaIr_3$, Ta_2O_5 electrode. The black spots are pores and the grey is Ta_2O_5. This particular electrode had a weight ratio (metal/oxide) of 2/1. Since it appeared that several of the white metal particles were grouped or were contacting one another, a slightly lower ratio of 1.8/1 was later used.

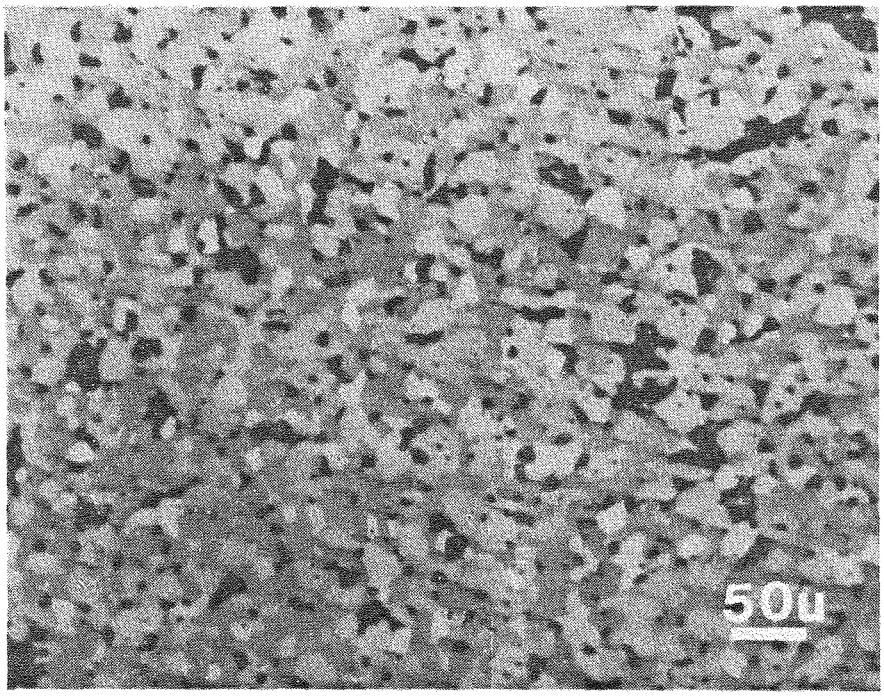

XBB 770-11455

Figure A-2. Polished surface of NbO_2, $Nb_2O_{4.8}$ electrode.

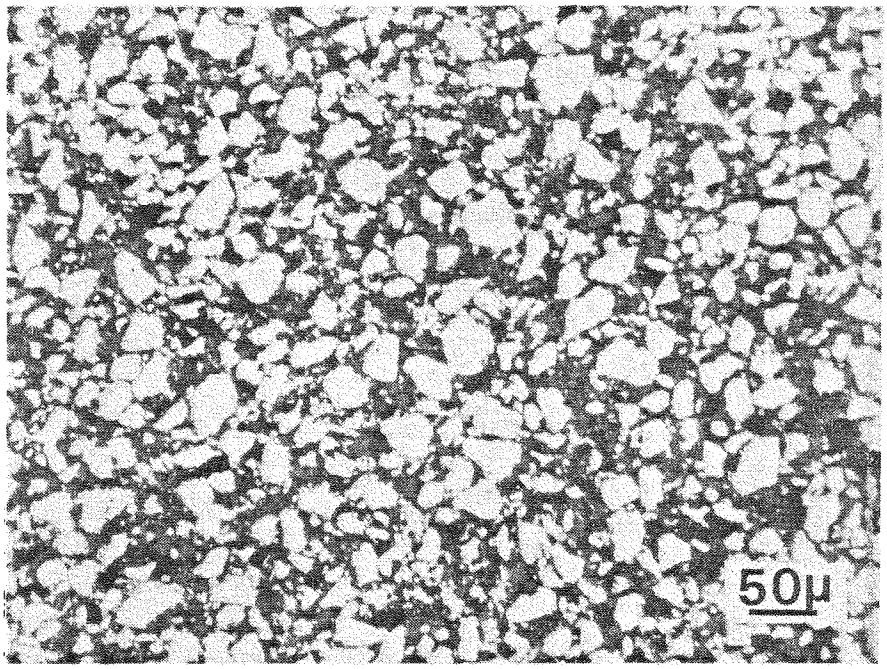

XBB 786-6733

Figure A-3. Polished surface of α-Ir, $TaIr_3$, Ta_2O_5 electrode.

REFERENCES

1. L. Brewer, Science 161, 115 (1968).

2. A. S. Darling, G. L. Selman, and R. Rushforth, Platinum Metals Rev. 14, 54 and 95 (1970).

3. S. J. Tauster, S. C. Fung, and R. L. Garten, J. Am. Chem. Soc. 100, 170 (1978).

4. Donald R. Olander, Fundamental Aspects of Nuclear Fuel Elements, Technical Information Center, Office of Public Affairs, Energy Research and Development Administration, 1976.

5. L. Brewers, Acta. Met. 15, 553 (1967).

6. K. Kiukkola and C. Wagner, J. Electrochem. Soc. 104, 379 (1957).

7. K. T. Jacob and C. B. Alcock, Met. Trans. 6B, 215 (1975).

8. L. Pauling, Phys. Rev. 54, 899 (1938); J. Am. Chem. Soc. 69, 542 (1947); Proc. Roy. Soc. (London) 196A, 343 (1949); Proc. Natl. Acad. Sci. 39, 551 (1953).

9. N. Engel, Some New Viewpoints on the Metallic Bond, 1945, issued as a Lawrence Radiation Laboratory report, Misc-1963-380.

10. L. Brewer, High Strength Materials, V. F. Zackay, Ed., Wiley, New York, 1965, pp. 12-103.

11. W. Hume-Rothery, J. Inst. Metals 35, 307 (1926); W. Hume-Rothery, R. E. Smallman, C. W. Haworth, The Structure of Metals and Alloys, 5th Ed., Institute of Metals, London, 1969, pp. 227-239.

12. N. Engel, Ingeniören, M101 (1939), M1 (1940); Haandbogi Metallăre: Selskabet for Metalforskning, Copenhagen, 1945; Kemisk Maandesblad 30, No. 5, 6, 8, 9, 10 (1949).

13. N. Engel, Powder Metallurgy Bulletin 7, 8 (1954).

14. N. Engel, Trans. Am. Soc. Metals 57, 610 (1964).

15. N. Engel, Acta. Met. 15, 557 and 565 (1967).

16. L. Brewer, Electronic Structure and Alloy Chemistry of the Transition Elements, Paul A. Beck, Ed., Interscience, New York, 1963, pp. 221-235.

17. L. Brewer, Phase Stability in Metals and Alloys, P. Rudman, J. Stringer, R. I. Jaffee, Eds., McGraw-Hill, New York, 1967, pp. 39-61, 241-9, 344-6, and 560-8.

18. L. Brewer, Amer. Institute of Physics Conference Proceedings, Magnetism and Magnetic Materials-1972, H. C. Wolf, Ed., No. 10, Part 1, 1973, pp. 1-16.

19. L. Brewer, Plutonium 1970 and Other Actinides, W. N. Miner, Ed., TMS Nuc. Met. Ser. Met. Soc. AIME, New York, Vol. 17, 1970, pp. 650-8.

20. L. Brewer, J. Opt. Soc. Am. 61, 1101 and 1666 (1971).

21. L. Brewer, J. Nuc. Mater. 51, 2 (1974).

22. L. Brewer, Rev. de Chim. Minefale 11, 616 (1974).

23. W. A. Balfour and A. E. Douglass, Can. J. Phys. 48, 901 (1970); L. Brewer and J. L.-F. Wang, J. Mol. Spectros. 40, 901 (1971).

24. L. B. Knight, Jr., R. D. Brittain, M. Duncan, C. H. Joyner, J. Phys. Chem. 79, 1183 (1975).

25. D. T. Peterson and R. P. Colburn, J. Phys. Chem. 70, 468 (1966).

26. W. H. Zachariasen, The Metal Plutonium, A. S. Cobbenberry and W. N. Miner, Eds., University of Chicago Press, Chicago, 1961, pp. 99-107.

27. W. Klement, Jr. and A. Jayaraman, Progress in Solid State Chemistry, H. Reiss, Ed., Vol. 3, Pergamon Press, New York, 1967, pp. 289-376.

28. C. W. F. T. Pistorius, Progress in Solid State Chemistry, J. McCaldin and G. Somorjai, Eds., Vol. 11, Pt. 1, Pergamon Press, New York, 1976, pp. 1-151.

29. W. Hume-Rothery, Electrons, Atoms, Metals, and Alloys, Dover Publications Inc., 1962, pp. 273-283.

30. J. T. Waber, K. Gschneidner, A. C. Larson, and M. Y. Prince, Trans. Met. Soc. AIME 227, 717 (1963).

31. W. Hume-Rothery, R. E. Smallman, C. W. Haworth, The Structure of Metals and Alloys, 5th Ed., Institute of Metals, London, 1969, pp. 277-286.

32. M. V. Nevitt, Electronic Structure and Alloy Chemistry of the Transition Elements, Paul A. Beck, Ed., Interscience, New York, 1963, pp. 101-178.

33. J. H. Hildebrand and R. L. Scott, Solubility of Non-Electrolytes, 3rd Ed., Dover Publications Inc., New York, 1964 (reprint of Reinhold, New York, 1950.)

34. J. H. Hildebrand and R. L. Scott, Regular Solutions, Prentice-Hall, Englewood Cliffs, N. J., 1962.

35. L. Brewer, Atomic Energy Review, Special Issue on Physical Chemical Properties of Molybdenum, Its Compounds and Alloys, Parts I and II, International Atomic Energy, Vienna, to be published 1978.

36. L. Brewer and P. R. Wengert, Met. Trans. 4, 83 (1973).

37. P. J. Meschter and W. L. Worrell, Met. Trans. 7A, 299 (1976).

38. P. J. Meschter and W. L. Worrell, Met. Trans. 8A, 503 (1977).

39. H. Rickert, Treatise on Solid State Chemistry, N. B. Hannay, Ed., Plenum Press, New York-London, 1976, Vol. 4, pp. 281-331.

40. H. Schmalzried, Metallurgical Chemistry, Proceedings of a Symposium Held at Brunel University and the National Physical Laboratory, July 14-16, 1971, London, HMSO, 1972, pp. 39-64.

41. R. A. Rapp and D. A. Shores, Physicochemical Measurements in Metals Research, R. A. Rapp, Ed., Wiley Interscience, New York 1970, Vol. 4, Part 2, pp. 123-192.

42. W. L. Worrell, Am. Cer. Soc. 53, 425 (1974).

43. F. A. Kroger, The Chemistry of Imperfect Crystals, 2nd Revised Ed., North-Holland, Amsterdam, 1974, Vol. 3, pp. 67-214.

44. T. H. Estell and S. N. Flengas, Chem. Rev. 70, 339 (1970).

45. T. A. Ramanarayanan and W. L. Worrell, Can. Met. Quart. 13, 325 (1974).

46. W. L. Worrell, International Symposium on Metal-Slag-Gas Reactions and Processes, Toronto, 1975, Z. A. Foroulis and W. W. Smeltzer, Ed., Electrochemical Soc., Princeton, N.J., 1975, pp. 822-833.

47. G. R. Fitterer, Metallurgical Chemistry, Proceedings of a Symposium Held at Brunel University and the National Physical Laboratory, July 14-16, 1971, London, HMSO, 1972, pp. 589-604.

48. E. T. Turkdogan and R. J. Fruehan, Can. Met. Quart. 11, 371 (1972).

49. R. C. Garvie, High Temperature Oxides, A. M. Alper, Ed., Academic Press Inc., New York, 1970, Vol. 5, Part 2, pp. 117-166.

50. R. C. Anderson, High Temperature Oxides, A. M. Alper, Ed., Academic Press Inc., New York, 1970, Vol. 5, Part 2, pp. 1-40.

51. J. W. Patterson, J. Electrochem. Soc. 118, 1033 (1971).

52. W. L. Worrell, Thermodynamics, International Atomic Energy Agency, Vienna, 1966, p. 131.

53. W. H. Ferguson, Jr., B. C. Giessen, N. J. Grant, Trans. Met. Soc. AIME 227, 1401 (1963).

54. W. B. Pearson, A. Handbook of Lattice Spacings and Structures of Metals and Alloys, Vol. 2, Pergamon Press, Oxford, 1967.

55. B. C. Giessen and N. J. Grant, Acta Cryst. 17, 615 (1964).

56. A. E. Dwight and P. A. Beck, Trans. Met. Soc. AIME 215, 976 (1959).

57. W. D. Kingery, J. Pappis, M. E. Doty, and D. C. Hill, J. Am. Cer. Soc. 42, 393 (1959).

58. P. J. Meschter and W. L. Worrell, Met. Trans. 6B, 345 (1975).

59. P. Gordon, Principles of Phase Diagrams in Materials Systems, McGraw-Hill, New York, 1968.

60. R. E. Barieau and W. F. Giauque, J. Am. Chem. Soc. 72, 5676 (1950); W. F. Giauque, R. E. Barieau, and J. E. Kunzler, J. Am. Chem. Soc. 72, 5685 (1950).

61. G. N. Lewis and M. Randall, Thermodynamics, 2nd Ed., rev. by K. S. Pitzer and L. Brewer, McGraw-Hill, New York, 1961.

62. L. S. Darken and R. W. Gurry, Physical Chemistry of Metals, McGraw-Hill, New York, 1953.

63. JANAF Thermochemical Tables, Joint Army-Navy-Air Force Thermochemical Panel, Thermal Laboratory, Dow Chemical, Midland, MI; Ta_2O_5, 1973; MoO_2, 1967; Cr_2O_3, 1974.

64. P. J. Meschter, Ph.D. Thesis, University of Pennsylvania, 1974.

65. M. Nagasaka and T. Yamashina, J. Less-Common Metals 45, 53 (1976).

66. R. Morrison, Grounding and Shielding Techniques in Instrumentation, John Wiley & Sons, Inc., New York, 1967.

67. T. Y. Tien and E. C. Subbaro, J. Chem. Phys. 39, 1041 (1963).

68. R. C. Garvie, J. Am. Cer. Soc. 51, 553 (1968).

69. R. A. Rapp, Trans. Met. Soc. AIME 227, 371 (1963).

70. S. Kimura, J. Solid State Chem. 6, 438 (1973); T. Kikuchi and M. Goto, J. Solid State Chem. 16, 363 (1976).

71. Treatise on Analytical Chemistry, I. M. Kolthoff, Ed., Part II: The Analytical Chemistry of the Elements, Vol. 6 and 8, Wiley Interscience, New York, 1963.

72. K. Goto, T. Ito, and M. Someno, Trans. Met. Soc. AIME 245, 1662 (1969).

73. R. Hultgren, P. D. Desai, D. T. Hawkins, M. Gleiser, K. K. Kelly, D. D. Wagman, Selected Values of the Thermodynamic Properties of the Elements, American Society for Metals, Metals Park, Ohio, 1973.

74. I. Katayama and Z. Kozuka, Technol. Rep. Osaka University 23, 411 (1973).

75. S. Berglund and P. Kierkegaard, Acta. Chem. Scand. 23, 329 (1969).

76. C. B. Alcock and J. C. Chan, Can. Met. Quart. 11, 559 (1972).

77. V. N. Drobyshev, T. N. Rezukhina, and L. A. Tarasova, Rus. J. Phy. Chem. 39(1), 70 (1965).

78. N. S. Zabeivorota, A. A. Lykasov, G. G. Mikhailov, E. L. Shakhin, Izvest. Akad. Nauk. SSSR, Neorg. Mater. 13(2), 388 (1977).

79. M. Iwase and T. Mori, Metal-Slag-Gas Reactions and Processes, Z. A. Foroulis and W. W. Smeltzer, Eds., Electrochem. Soc., Princeton, NJ, 1975, pp. 885-902.

80. G. B. Barbi, J. Phy. Chem. 68, 1025 (1964).

81. D. Janke and W. A. Fischer, Arch. Eisenhüttenwes. 46, 755 (1975).

82. F. N. Mazandarany and R. D. Pehlke, J. Electrochem. Soc. 121, 711 (1974).

83. K. Suzuki and K. Sambongi, Tetsu To Hagane 58, 1579 (1972).

84. H. Davies and W. W. Smeltzer, J. Electrochem. Soc. 121, 543 (1974).

85. J. D. Tretjakow and H. Schmalzried, Ber. Bunsenges. 69, 396 (1965).

86. L. A. Pugliese and G. R. Fitterer, Met. Trans. 1, 1997 (1970).

87. R. J. Fruehan, L. J. Martonik, and E. T. Turkdogan, Trans. Met. Soc. AIME 245, 1501 (1969).

88. M. Sundaresen, Y. I. Gerasimov, V. A. Geiderikh, and I. A. Vasil'eva, Rus. J. of Phy. Chem. 37(11), 1330 (1963).

89. C. B. Alcock and A. Kubik, Acta. Met. 17, 437 (1969).

90. G. B. Barbi, J. Less-Com. Met. 29, 397 (1972).

91. V. N. Drobyshev and T. N. Resukhina, Rus. J. Phy. Chem. 39(1), 75 (1965).

92. T. N. Resukhina and Z. V. Proshina, Rus. J. Phy. Chem. 36(3), 333 (1962).

93. D. Chatterji and J. V. Smith, J. Electrochem. Soc. 120, 889 (1973).

94. T. Rosenqvist and J. Haugom, J. Chem. Soc. Faraday Trans. I, 73, 913 (1977).

95. P. Kofstad, Nonstoichiometry, Diffusion, and Electrical Conductivity in Binary Metal Oxides, Wiley Interscience, New York, 1972; ZrO_2, Chapter 8.

96. N. F. Mott and R. W. Gurry, Electronic Processes in Ionic Crystals, Dover Pub., Inc., New York, 1964; reprint of 2nd ed., Oxford, 1948; Chapter 3.

97. A. W. Smith, F. W. Meszaros, and C. D. Amata, J. Am. Ceram. Soc. 49, 240 (1966).

98. J. Fouletier, P. Fabry, and M. Kleitz, J. Electrochem. Soc. 123, 204 (1976).

99. L. H. Fisher and R. N. Varney, Amer. J. Phys. 44, 464 (1976).

100. R. Parsons, Modern Aspects of Electrochemistry, J. O'M. Bockris, Ed., Academic Press Inc., New York, 1954, Vol. 1, pp. 103-179.

101. E. Spenke, Electronic Semiconductors, McGraw-Hill Book Co., New York, 1958; a translation of Elektronishe Halbleiter, 2nd ed., Springer-Verlag; especially Chapter 10.

102. N. S. choudhury and J. W. Patterson, J. Electrochem. Soc. 117, 1384 (1970).

103. W. L. Worrell and J. L. Iskoe, Fast Ion Transport in Solids, W. vanGool, Ed., North-Holland Publishing Co., 1973, pp. 513-521.

104. D. A. MacInnes, The Principles of Electrochemistry, Dover Pub., Inc., New York, 1961; reprint of 2nd ed., Reinhold Pub. Corp., Chapter 13 and Appendix.

105. C. Wagner, Adv. in Electrochem. and Electrochemical Eng., P. Delahay, Ed., Wiley Interscience, 1966, Vol. 4, pp. 1-46.

106. C. Wagner, Z. Phy. Chem. B21, 25 (1933).

107. L. Heyne, Mass Transport in Oxides, J. B. Wachtman Jr. and A. D. Franklin, Eds., NBS Special Pub. 296, U.S. Gov't. Printing Office, Washington, D.C., 1968, pp. 149-164.

108. N. M. Beekmans and L. Heyne, Electrochim. Acta 21, 303 (1976).

109. J. W. Patterson, E. C. Bogren, and R. A. Rapp, J. Electrochem. Soc. 114, 752 (1967).

110. J. H. Swisher and E. T. Turkdogan, Trans. Met. Soc. AIME 239, 426 (1967).

111. D. Caplan, M. J. Frazer, and A. A. Burr, Ductile Chromium, American Society for Metals, Metals Park, Ohio, 1957, pp. 196-215.

112. R. Hartung, Z. Phy. Chem., Leipzig 256, 997 (1975).

113. S. Ban-ya, J. F. Elliot, and J. Chipman, Met. Trans. 1, 1313 (1970).

114. C. Wagner, Z. Electrochem. 40, 365 (1934).

115. D. A. Shores and R. A. Rapp, J. Electrochem. Soc. 118, 1107 (1971).

116. J. E. Stroud and W. C. Tripp, J. Am. Cer. Soc. 57, 172 (1974).

117. M. M. Nasrallah and D. L. Douglass, J. Electrochem. Soc. 121, 255 (1974).

118. C. Wagner, Progress in Solid State Chemistry, H. Reiss and J. O. McCaldin, Eds., Vol. 7, Pergamon Press, New York, 1972, pp. 1-37.

119. R. J. Moffat, Temperature, Its Measurement and Control in Science and Industry, Part 2, Applied Methods and Instruments, A. I. Dahl, Ed., Reinhold Pub. Corp., New York, 1962, pp. 33-38.

120. B. C. Giessen, H. Ibach, and N. J. Grant, Trans. Met. Soc. AIME 230, 113 (1964).

TECHNICAL INFORMATION DEPARTMENT
LAWRENCE BERKELEY LABORATORY
UNIVERSITY OF CALIFORNIA
BERKELEY, CALIFORNIA 94720